This MS has been accepted for publication on Chem: doi:10.1016/j.chempr.2018.05.016

URL: https://www.cell.com/action/showMethods?pii=S2451-9294%2818%2930225-0

Chirality effects on peptide self-assembly unravelled from molecules to materials

Ana M. Garcia[1], Daniel Iglesias[1], Evelina Parisi[1], Katie E. Styan[2], Lynne J. Waddington[2], Caterina Deganutti[1], Rita De Zorzi[1], Mario Grassi[3], Michele Melchionna[1], Attilio V. Vargiu[4]*, and Silvia Marchesan[1]*

Affiliations

1. Department of Chemical & Pharmaceutical Sciences, University of Trieste, Trieste, Italy.
2. CSIRO Manufacturing, Clayton, Victoria, Australia.
3. Department of Industrial Chemistry, University of Trieste, Trieste, Italy.
4. Department of Physics, University of Cagliari, Monserrato, Italy.

*Correspondence: vargiu@dsf.unica.it, smarchesan@units.it

Summary

Self-assembling short peptides are attractive minimal systems to mimic the constituents of living systems and to build (bio)materials. The combination of both D- and L-amino acids into heterochiral sequences is a versatile strategy to build durable supramolecular architectures, especially when their homochiral analogues do not self-assemble. The reasons for this divergent behaviour have remained obscure until now. Here we elucidate how and why homochiral and heterochiral peptides behave differently. We identify a key spectroscopy signature and its corresponding molecular conformation, whereby an amphiphilic structure is

uniquely enabled by the peptide stereochemistry. Importantly, we unravel the self-assembly process as a *continuum* from the conformation of single molecules, to their organisation into nano- and micro-structures, and through to macroscopic hydrogels, which are probed for cytotoxicity in fibroblast cell culture. In this way, (bio)material properties at the macroscale can be linked to the chemical structure of their building blocks at the Ångstrom scale.

Keywords: peptide, self-assembly, chirality, hydrogels, D-amino acids, water channels, nanostructures.

Introduction

Peptides self-assemble to make up the materials of life. The fine-grained details of their organisation give rise to useful properties, from the toughness of spider silk to the delicate dynamism of the structures of the cytoskeleton. New knowledge of how peptide self-assembly works in minimal systems – those comprising only a few amino acid residues – could provide a basis for understanding how more complex protein assemblies form, and it is expected also to allow useful materials to be generated. The functional materials formed by self-organising minimalist peptides have high value.[1] Their applications include drug delivery,[2] tissue engineering,[3] biomimicry,[4] cancer cell detection,[5] and even vaccine-adjuvants to stimulate the immune response,[6] through to uses as emulsifiers,[7] pigments,[8] catalysts,[9] and semiconductors.[10] Peptides stand out for their chemical diversity, low impact on the environment, and ability to convey biological messages in sequences as short as three amino acids.[11] However, it is less well-understood that non-proteogenic D-amino acids play crucial roles in short bioactive motifs, such as D-Phe in fibronectin-mimics for integrin engagement,[12] and D-Ala in demorphin for opioid receptor binding.[13] D-amino acids are also attracting attention for their emerging role in brain neurotransmission.[14, 15] In addition, they are known to bestow resistance against enzymatic hydrolysis and stability upon specific peptide conformations, such as β-turns.[16] Such findings generate new motivation for employing D-amino acids in simple building blocks for supramolecular biomaterials, where structure and function are entwined.

In light of the cost of large-scale peptide production, the search is very active for the smallest motifs capable of achieving a chosen function. Hydrogel formation is a useful feature that is, unfortunately, difficult to predict. Computational approaches are proving useful in the search for gel-forming peptides, especially for derivatives bearing rigid aromatic groups that dominate self-assembly behaviour, such as fluorenyl (in Fmoc), or naphthalene.[17] However, concerns exist over the fate of these modified peptides *in vivo*, and thus over their biological application.[18, 19] Successful prediction of gel formation is most difficult for the shortest unprotected peptides. For example, only four new gelators were experimentally identified guided by an *in silico* analysis of all 8,000 combinations of L-amino acids in trimers.[20] There is thus large scope for new approaches to the discovery[21] or the rational design of short peptides able to gel, especially under physiological conditions. Advances in this area could provide new means of therapy, by eliciting a biological response through assembly *in vivo*.[22] In addition, the combination of both L- and D- amino acids in short peptides could provide a unique approach to fine-tune their lifetime in biological settings and to shed new light on Nature's pervasive choice for homochirality. Ultimately, understanding the effects of D-amino acids in short peptide self-organisation could advance therapeutic solutions for amyloidoses,[23] implicated from neurodegeneration[24] to diabetes,[25] as well as for infections linked to biofilm formation.[26]

The design of peptides that self-assemble to form hydrogels requires a fine balance between hydrophobic and hydrophilic content, so as to achieve aggregation whilst allowing favourable interactions with water to avoid precipitation. Such amphiphilic structures are typically obtained by intra-peptide segregation of hydrophilic and hydrophobic amino acids, for instance in α-helices, which require longer peptides composed of heptad repeats.[27] Alternatively, amphiphilic β-sheets are formed by the alternation of ionic and hydrophobic amino acids (Fig. 1A).[28] The inclusion of hydrophilic amino acids in unprotected L-tripeptides has been an essential feature to obtain amphiphilic assemblies that gel.[20, 29]

Here we detail a new concept of hydrogel formation using the peptide backbone as the only hydrophilic component. We infer the alternation of D- and L-amino acids to favour an *amphiphilic β-conformation* that is effective for self-assembly and gelation in a peptide of only three residues. Our approach leads hydrophobic side chains and hydrophilic backbone groups to be displayed on opposite sides of the peptide

(Fig. 1B). The effects of heterochirality upon unprotected (tri)peptide gelation have been observed in isolated examples,[30-33] but a conceptual framework for understanding these effects has been lacking until now. This study aims to provide such a framework by unveiling the effects of fine structural changes on peptide conformation and consequent packing into soft materials, and thus on their macroscopic properties. The rational design of a series of hydrogelators (Fig. 1C and Table 1) was accompanied by both *in silico* and experimental investigations of self-assembly from the initial monomer state, through each stage and length scale up to the macroscopic material, which was then probed for cytotoxicity *via* cell culture. Importantly, for the first time we have identified a key circular dichroism (CD) signature and its correspondence with peptide conformation, revealing how homochiral and heterochiral analogues are similar, and how they differ, in the domino process leading to macroscopic gelation.

Results and Discussion

Rational design of self-assembling tripeptides. A series of hydrophobic ^{L}Phe-^{D}Xaa-^{L}Phe tripeptides, where ^{D}Xaa is an aliphatic D-amino acid (Fig. 1C and Table 1), was prepared by solid-phase peptide synthesis (SPPS) and purified by high-performance liquid chromatography (HPLC). This series included all naturally-occurring side chain lengths (*i.e.*, methyl, propyl, and butyl groups) and all possible branching options (*i.e.*, β-, γ-branched or linear side chain) for common building blocks to allow a thorough correlation between chemical structure and assembly. The alternation of D and L handedness was designed to yield two-faced amphiphilic supramolecular β-sheets, as predicted by molecular dynamics (MD) simulations in explicit water.[34] Superstructures were designed to be held together by an ordered pattern of hydrogen bonding between amides, and salt bridges between the charged ammonium and carboxylate termini, which together provide the hydrophilic content (see Supplementary Fig. S41). The presence of Phe at both termini allowed interdigitation between stacks into supramolecular zippers that exclude water.[32] Indeed, MD showed that within

nanoseconds Phe-^{D}Ile-Phe formed stacks that converged into elongated fibres of approximately 5 nm in diameter (Fig. 1D-F and Supplementary Video SV1).

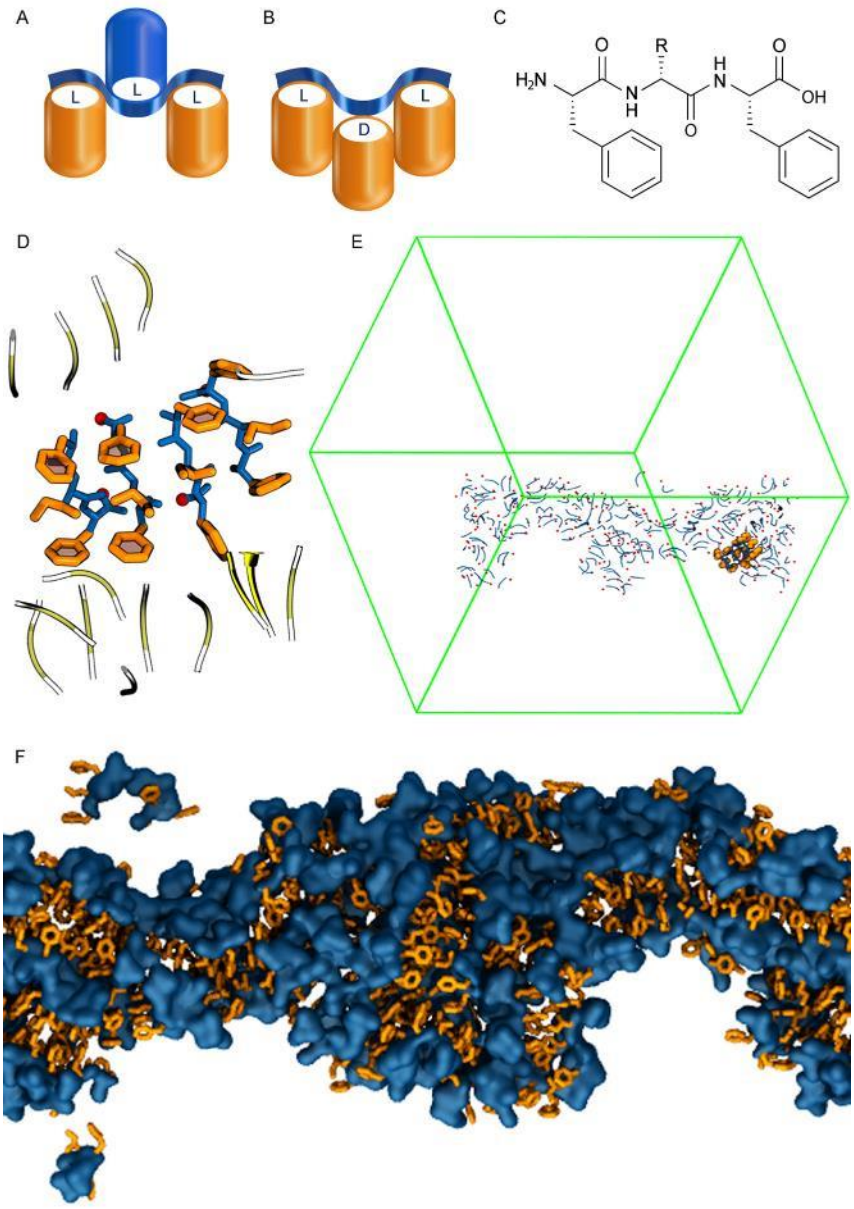

Fig. 1. Tripeptides that contain alternating L- and D-amino acid residues generate amphipathic fibres.

A, Traditional design alternates hydrophilic (blue) and hydrophobic (orange) L-amino acids to create amphipathic structures, whereas in this study **B**, the alternation of L- and D- hydrophobic amino acids generates amphiphiles where the hydrophilic component is the peptide backbone (blue string). **C**, a generic tripeptide sequence structure (see Table 1 for a list of R side chains). **D-F**, MD

simulations of Phe-^{D}Ile-Phe in explicit water show amphiphilic β-sheets interdigitating into fibres within nanoseconds, wherein peptide stacks (**D**) display hydrophobic side chains on the same side of the peptide backbone; these side chains are highlighted in orange in the MD box (**E**) containing 216 peptides that self-organise into amphipathic nanofibres (**F**, peptide oxygen and nitrogen atoms, and water oxygen atoms within 2 Å from peptides are shown as a blue surface).

Table 1. Phe-^{D}Xaa-Phe peptides of this study. The series includes different central amino acids (^{D}Xaa) with aliphatic side chains (R); hydrophobicity (based on logP[35] and experimental HPLC retention time) correlates with minimum gelling concentration (MGC).

^{D}Xaa	R	logP	HPLC Retention time (min.)	MGC (mM)
Alanine (Ala)	$-CH_3$	1.50 ± 0.20	7.3	n.a.
Valine (Val)	$-CH(CH_3)_2$	2.39 ± 0.21	8.0	9.5
Norvaline (Nva)	$-CH_2CH_2CH_3$	2.47 ± 0.32	8.0	9.5
Isoleucine (Ile)	$-CH(CH_3)CH_2CH_3$	2.83 ± 0.27	8.3	8.0
Leucine (Leu)	$-CH_2CH(CH_3)_2$	2.76 ± 0.32	8.4	5.0
Norleucine (Nle)	$-CH_2CH_2CH_2CH_3$	2.91 ± 0.38	8.4	5.0

Circular dichroism (CD) signature and peptide conformation in solution. This series of heterochiral tripeptides displayed a characteristic CD signature in the monomer state (Fig. 2A and Supplementary Fig. S42) that was very different from that of more commonly observed conformations (*e.g.*, α-helix, β-sheets, random coils). The molar ellipticity did not change following sample dilution at different concentrations that were well below the minimum gelation concentration (MGC), confirming a monomeric state.

The naturally occurring L-tripeptides Phe-Xaa-Phe (with Xaa = Ala, Val, Nva, Leu, Ile, or Nle) served as controls, leading us to infer this CD signature to be a result of predominant L-configuration (Fig. 2A and Supporting Fig. S42), as reported for self-assembling Phe-Glu-Phe in solution[36] as well as for non-assembling

L-peptides containing Phe.[37] However, the physical origin of this CD signature in terms of peptide conformation(s) remains obscure. We hypothesise that it is due to a statistical coil, whereby unfolded peptides sample specific conformational states that co-exist in equilibrium. The two positive maxima observed at 199 and 219 nm are assigned to $\pi \rightarrow \pi^*$ and $n \rightarrow \pi^*$ transitions of the peptide bonds, respectively, and their CD signatures are thus affected by the relative orientations of the corresponding dipoles of the two amides, as well as interactions with their environment.

Comparison of the conformations of self-assembling Phe-^{D}Ile-Phe and Phe-^{D}Leu-Phe, and the non-gelling L-peptide Phe-Ala-Phe, helps to elucidate how self-assembly works in heterochiral tripeptides (Fig. 2B-E). The former two are the most sterically hindered amino acids that are branched at the γ- and β-positions, respectively. The latter is homochiral and displays the least steric hindrance. In the monomeric state, the self-assembling tripeptides sample three principal conformations (accounting for ca. 90% of the population, see Supplementary Fig. S43), of which the most representative is displayed in Fig. 2B. Although the side-chain branching differences between Ile and Leu are known to favour different conformations,[38, 39] here there is a striking similarity between the two, with both adopting an amphiphilic conformation. Their aliphatic side chains are sandwiched between the two Phe aromatic rings, creating a hydrophobic region that effectively excludes water and leads the backbone to turn, while the charged termini are displayed on the opposite side of the peptide backbone, as design dictates.

Phe-Ala-Phe, being the least sterically hindered tripeptide, displayed more freedom and sampled two dominant conformations nearly equally (Fig. 2B). Also in this case, the Phe side chains were on the opposite side of the peptide backbone from the charged termini, but the L-Ala hydrophobic methyl side chain was projected into the otherwise hydrophilic region, leaving a void between the aromatic rings. As a result, Phe-Ala-Phe did not display an overall amphiphilic conformation with net segregation of aliphatic side chains and hydrophilic components.

Peptide and protein structures are described by using Ramachandran plots, whereby specific combinations of backbone dihedral angles Φ and Ψ correspond to defined conformations (e.g., β-sheets, α-helices,

etc.).[40] Ramachandran plots of the three model peptides (Figure 2C) showed a common trend, considering that D-peptide regions are analogous to L-peptides when inverted through the centre of the plot. The dihedral angles for the predominant conformations are overlaid in the Ramachandran plot. All are located in a β-strand area, having Φ and Ψ angles combinations for the second residue that are found in type II β-turns (*i.e.*, [-60, + 120] ±30°).[41] Although these unprotected tripeptides are too short to fulfil all of the requirements for the canonical definition of a turn,[42] these conformations can be considered turns based on the overall change of direction of the peptide backbone, and by the $C_{\alpha 1}$-$C_{\alpha 3}$ distance being less than 7 Ångstroms (see Supplementary Table S3).[41] Importantly, the peptide backbones of the three most frequently observed conformations for each tripeptide are nearly superimposable (inset in Fig. 2D). Indeed, the relative dipole orientations of the peptide bonds reveal analogous distributions (Fig. 2D), in agreement with their similar CD signatures. Correspondence between CD spectra and conformations is supported by theoretical CD spectra calculated for the MD conformations (dashed traces in Fig. 2A), which show the same trends observed in the experimental data (continuous lines in Fig. 2A and Supplementary Fig. S42).

However, only heterochiral L-D-L tripeptides display the three hydrophobic side chains on the same side of the peptide backbone, where their mutual interactions favour a turn overall by excluding water molecules (Fig. 2B). In contrast, L-tripeptides do not experience such an effect, and their backbones stay more extended, as supported by MD-calculated N-to-C distances, which are shorter for self-assembling tripeptides (Fig. 2E).

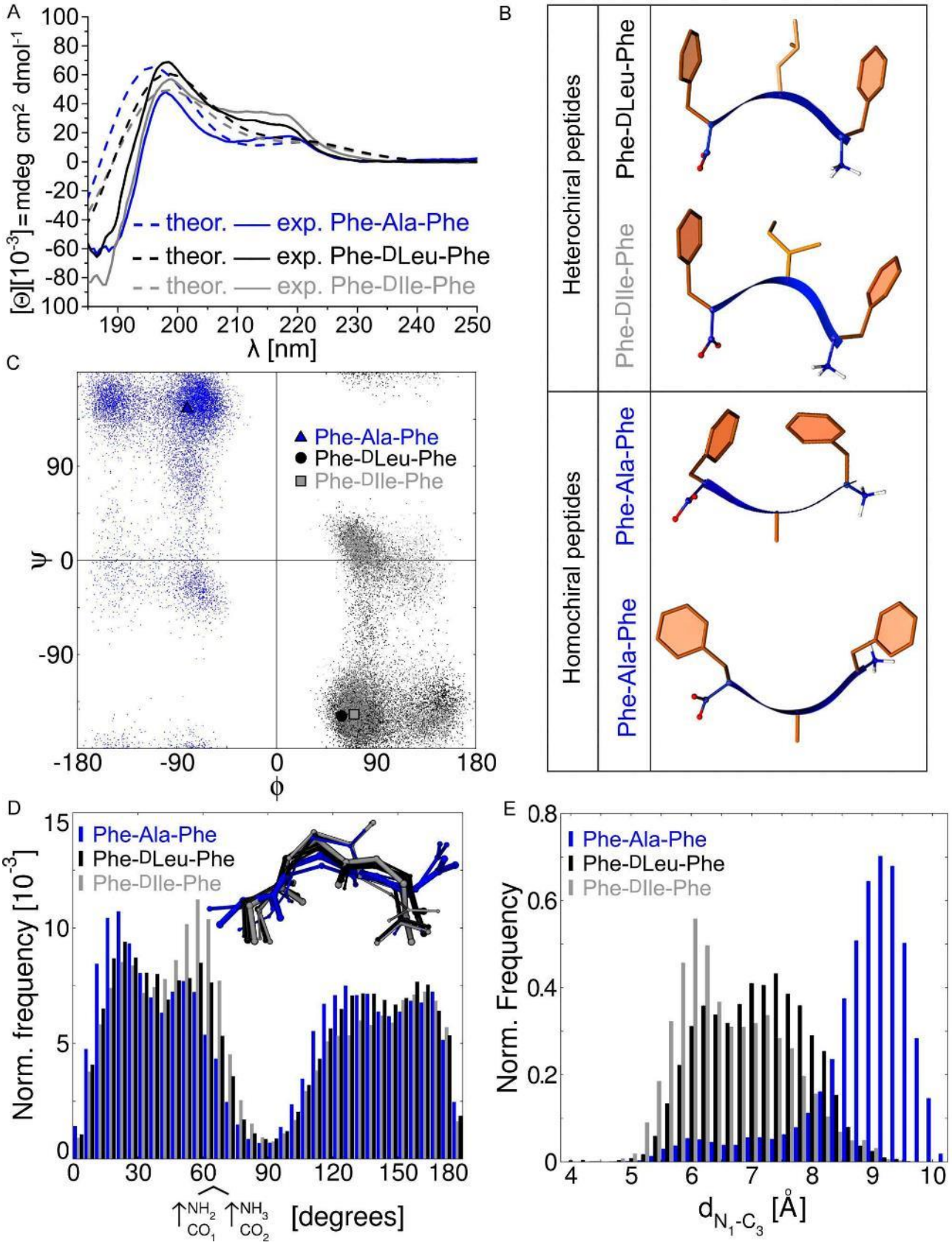

Fig. 2. Why heterochiral peptides self-assemble, and their homochiral analogues do not.

A, Calculated and experimental circular dichroism (CD) spectra for three representative tripeptides. **B**, Favoured amphiphilic conformation (hydrophobic side chain in orange and hydrophilic backbone in blue) for self-assembling tripeptides and the two equally most stable conformations for Phe-Ala-Phe. **C**, Ramachandran plot highlighting the most frequent conformations for the three tripeptides studied. **D**, The relative dipole orientation distributions are analogous for the three tripeptides studied, as confirmed by the superimposable peptide backbones of the three most stable conformations of the three peptides. **E**, N-to-C distances confirm the L-tripeptides to have more extended structures than the heterochiral tripeptides.

Single-crystal XRD structures. Single-crystal XRD data revealed a dramatic difference between the packing of heterochiral and homochiral tripeptides (Fig. 3). Phe-^{D}Nva-Phe displayed an amphipathic conformation with net segregation of hydrophobic and hydrophilic components on opposite sides of the backbone, as predicted by MD studies. The latter face the interior of 2.0-nm wide water channels, while the former create hydrophobic regions whereby amino acid side chains from different channels interdigitate and hold the structure together (Fig. 3A). By contrast, single-crystal XRD data for Phe-Ala-Phe revealed an extended conformation incapable of fully separating hydrophilic (blue) and hydrophobic (orange) components, since the hydrophobic Ala side chain impinges upon the hydrophilic region containing water molecules. As a net result, water channels are not formed by the homochiral tripeptide (Fig. 3B).

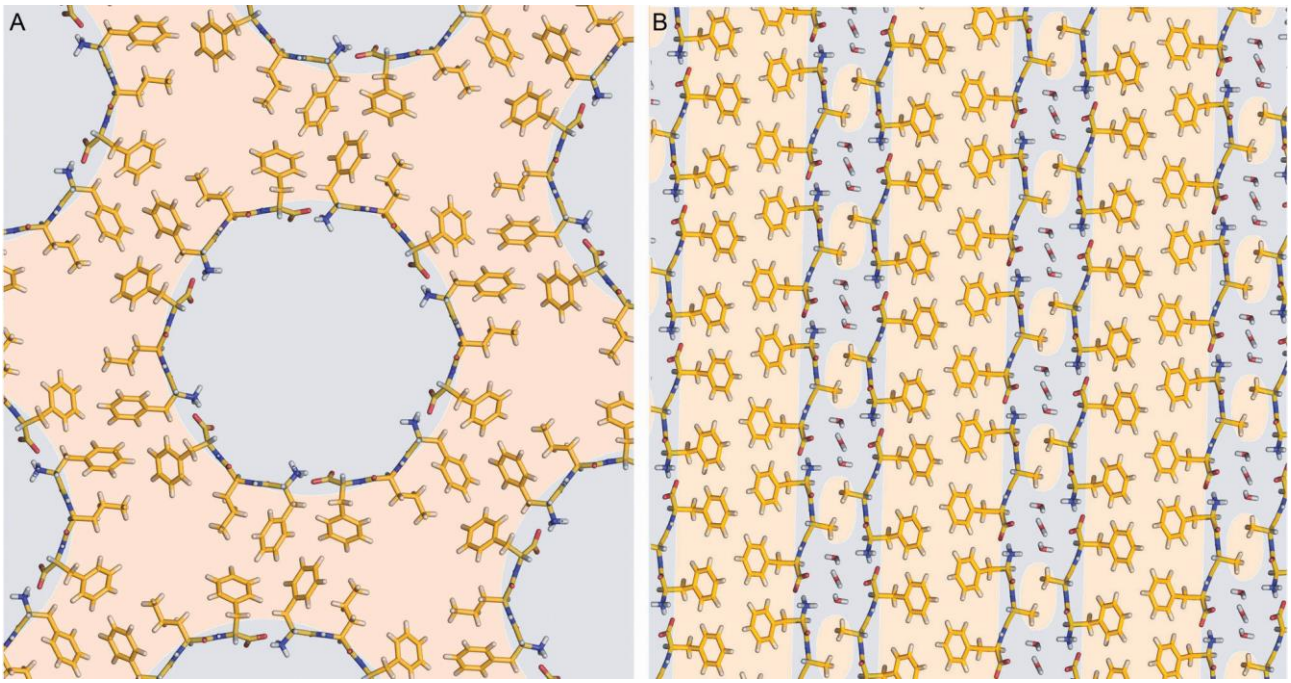

Fig. 3. Single-crystal XRD data reveal very different packing for heterochiral and homochiral peptides.

A, Phe-^{D}Nva-Phe packing shows net segregation of hydrophobic (orange) and hydrophilic (blue) components, allowing the formation of 2.0 nm-wide water channels. **B**, Homochiral Phe-Ala-Phe packs into layers, whereby Ala methyl side chain impinges in an otherwise hydrophilic region.

This combination of crystallographic, MD and spectroscopic evidence thus provides the first clear picture of why heterochiral peptides self-assemble to form hydrogels, whereas their homochiral analogues do not. In light of these new findings, we infer that a similar mechanism could drive the formation of nanostructured hydrogels by other tripeptides featuring scrambled sequences of D- and L-hydrophobic residues with only one Phe at the termini (*e.g.*, Val-^{D}Phe-Phe,[30] ^{D}Val-Phe-Phe,[30] ^{D}Phe-Phe-Val,[31] ^{D}Leu-Phe-Phe,[32] ^{D}Phe-Phe-Ile,[33] His-^{D}Phe-^{D}Phe,[43] etc.). Similarly, amphipathic conformations are expected, as well as formation of dry steric zippers that exclude water and hold the superstructures together. However, differences between building blocks are likely to result in packing variations, whereby water channels, when formed, may vary in diameter and overall topology. Expansion of design rules to a more diverse toolbox of heterochiral peptides opens thus the way to exciting possibilities for the design of supramolecular channels and functional architectures.

Monitoring peptide conformation during assembly and disassembly. Tripeptides were first added to alkaline phosphate buffer, where they dissolved due to electrostatic repulsion between their negative charges. Neutralisation of the pH was then used to probe self-assembly and hydrogelation of the resulting zwitterions, which are capable of engaging in salt bridges given a favourable peptide conformation. Molar ellipticity of CD spectra did not change significantly for non-gelling Phe-Xaa-Phe (Xaa = Ala, Val, Nva, Leu, Ile or Nle) L- analogues and Phe-^{D}Ala-Phe, relative to their monomeric state in dilute samples (see Supplementary Figs. S44). For all of the other, self-assembling, D,L-tripeptides, assembly over time and disassembly upon heating were monitored by CD (see Fig. 4 and Supplementary Fig. S46), confirming visual observations (see Supplementary Table S4). All peptide hydrogels showed thermoreversibility, albeit with

gel-to-sol transitions occurring at different temperatures, reflecting the increasing stability of their supramolecular structures as hydrophobicity increased.

CD signature was qualitatively preserved across most gel-forming peptides, suggesting that peptide conformation did not change significantly from the monomeric state, in agreement with MD data (compare Fig. 1D with Fig. 2B). By contrast, quantitative differences were ascribed to variations in peptide spatial arrangement upon stacking into supramolecular structures, which ultimately led to hypochromic and hyperchromic shifts. The majority of peptides displayed a broad, positive CD signal in the region 200-220 nm, which is compatible with β-structures of D-chirality, as previously observed for other L-D-L self-assembling tripeptides.[30, 31] Phe-^{D}Leu-Phe was the only peptide exhibiting a negative CD signal in the assembled state, yet MD analysis did not reveal significant differences relative to Phe-^{D}Ile-Phe other than an increased twist in the pleated β-sheets, which were significantly more planar in the latter case (see Supplementary Fig. S47). These data suggest that differences in CD spectra may be ascribed mainly to higher order organisation of the fibrils, rather than different peptide conformations. Attenuated total reflectance infrared spectroscopy (ATR-IR) data supported this hypothesis, with one predominant amide I signal centred at 1645-1651 cm^{-1} for all peptides (see Supplementary Fig. S48). This signal is close to the expected β-sheet signal, as was observed for other self-assembling L-tripeptides.[20] The narrowest amide I signal was displayed by Phe-^{D}Leu-Phe, followed by the other gelators. It provides an indication of homogenous conformation and high degree of supramolecular order. By contrast, the broadest amide I signal with multiple maxima was displayed by non-assembling peptide Phe-^{D}Ala-Phe, indicating sample heterogeneity and the presence of different conformations.

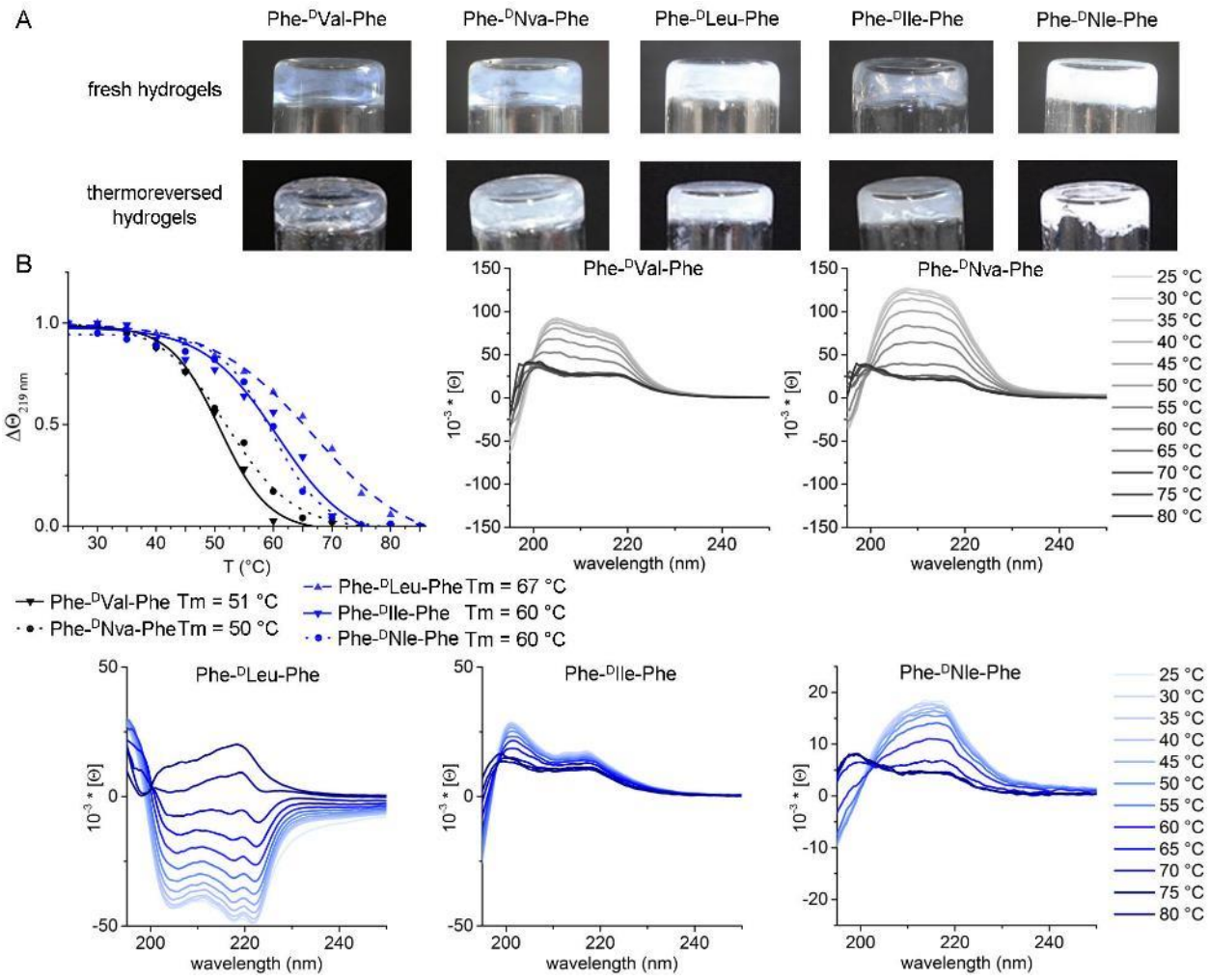

Fig. 4. Peptides form thermoreversible hydrogels.

A, Photographs of fresh (top) and thermoreversed (heated then cooled, bottom) tripeptide hydrogels. **B**, Monitoring of supramolecular structure by CD over a temperature ramp up to 80°C. Melting temperature (Tm) can be determined by plotting molar ellipticity [Θ] at 219 nm as the temperature is increased. Data for peptides bearing valine isomers are depicted in grey, those for leucine isomers are presented in blue.

Self-assembled nanostructure morphology and rheological properties. Peptide Phe-^{D}Ala-Phe is the least hydrophobic and sterically hindered of the series, and no hydrogel or ordered nanostructure was observed to form as expected (see Supplementary Figs. S45, S56, and S57). By contrast, all other heterochiral samples formed nanostructured hydrogels, as revealed by atomic force microscopy (AFM), transmission electron microscopy (TEM), cryogenic TEM (cryo-TEM) imaging, and rheometric analyses (Fig. 5 and Supplementary Figs. S58-S68). Samples composed of thinner fibrils were more transparent, while those

containing thicker bundles appeared opaque white. No hydrogel was obtained from homochiral analogues, even when their concentration exceeded their solubility limit (Supplementary Fig. S45).

With regards to nanomorphology, the majority of homochiral controls formed amorphous aggregates as revealed by TEM and AFM (Supplementary Fig. S49-S55), with the exception of Phe-Ala-Phe, which showed tendency towards formation of microcrystals, thus allowing us to investigate its structure by single-crystal XRD (*vide infra*). By contrast, heterochiral peptides, both displaying Val or Leu isomers, all assembled into fibrils, although diverse in terms of rigidity, and tendency towards branching or bundling (Fig. 5A). In particular, presence of amino acids with side-chain branching closer to the peptide backbone (*i.e.*, at the β-position for ^{D}Val and ^{D}Ile) promoted branching as opposed to bundling. The net result was that peptides bearing ^{D}Val and ^{D}Ile formed thinner fibrils of narrower diameter distribution that were better interconnected in hydrogel networks. Phe-^{D}Val-Phe and Phe-^{D}Ile-Phe formed flexible fibrils as thin as 7 ± 2 nm and 8 ± 2 nm (*n*=100), respectively, that occasionally wound up in numbers of two-to-three (average diameter 15 ± 4 nm and 15 ± 5 nm, *n* = 25, respectively). Instead, Phe-^{D}Leu-Phe assembled into 11 ± 2 nm-wide (*n*=100) fibrils, which for the majority ran parallel to each other or bundled in stiffer fibres very diverse in thickness, *i.e.* 47 ± 37 nm (*n*=100). Phe-^{D}Nva-Phe assembled into 16 ± 3 nm-wide fibrils, which for the majority entangled into bundles of heterogeneous dimensions (average diameter of 76 ± 27 nm, *n*=50). The presence of amino acids with linear side-chains (i.e., ^{D}Nva or ^{D}Nle) allowed peptides to pack efficiently into hierarchical structures, resulting in stiffer and thicker fibres, with the extreme case of ^{D}Nle leading to straight, nearly micron-thick, bundles.

In terms of rheological properties (Fig. 5B), the stability of heterochiral peptide supramolecular structures appeared to increase with steric hindrance, with peptides containing four methylene units (*i.e.*, ^{D}Ile, ^{D}Leu, or ^{D}Nle) surpassing in stability those containing only three (*i.e.*, ^{D}Val or ^{D}Nva). The former had faster gelation kinetics and higher elastic moduli G'. Interestingly, the presence of amino acids with linear side chains (*i.e.*, ^{D}Nva or ^{D}Nle), which promoted hierarchical assembly and bundling into thick and rigid fibres as discussed above, negatively affected hydrogel resistance against applied stress, as exemplified by ^{D}Nle-peptide that was observed to segregate from the aqueous phase. On the contrary, presence of amino acids

with β-branching (*i.e.*, ^{D}Val or ^{D}Ile), which promoted formation of a dense network with a higher level of interconnectivity between flexible and thin fibrils, led to hydrogels that exhibited increased resistance against applied stress, relative to their structural isomers.

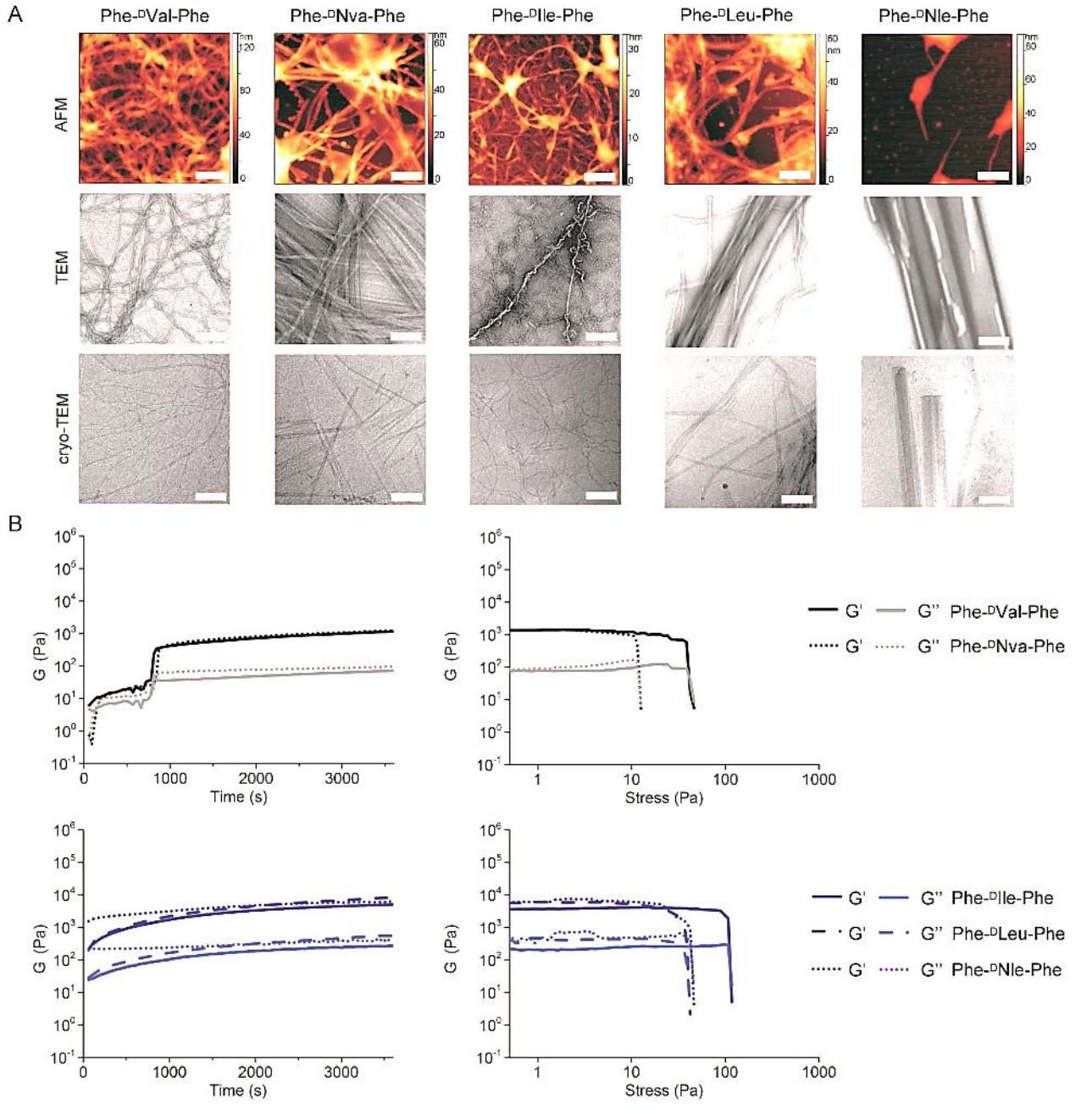

Fig. 5. Nanostructured hydrogels morphology and viscoelastic properties.

A, AFM, TEM, and cryo-TEM images of the peptide hydrogels. Scale bar = 500 nm for AFM images (top row), and 200 nm for TEM and cryo-TEM images (central and bottom row, respectively). **B**, Time sweeps (left) and stress sweeps (right) oscillatory rheometry measurements assessed the gel nature and the viscoelastic

properties of peptide hydrogels containing a central amino acid with three (top) or four (bottom) methylene units in the aliphatic side chain.

Hydrogel biomaterial performance. All heterochiral peptides were tested for their cytotoxicity in fibroblast cell culture *in vitro*, in solution or in the hydrogel state. Cell viability in solution was assessed with increasing concentrations up to the peptide solubility limit (2 mg ml^{-1} in 1% DMSO). Cell viability was greater than 90% relative to the control, with the exceptions of the two peptides bearing both a non-natural stereoconfiguration and a non-natural, linear side chain (*i.e.,* ^{D}Nva and ^{D}Nle) leading to cell viability in the range of 80-90%, significantly lower than the control (see Supplementary Fig. S70). Cell morphology did not appear altered by the presence of peptides (Fig. 6A and Supplementary Fig. S71), except for the case of ^{D}Nle, whereby the number of round cells was significantly higher than the control, with visible peptide fibrillisation occuring over 24 hours at the highest concentration tested (Fig. S71). Rare instances of rigid fibrils were noted also for the sample bearing ^{D}Nva, suggesting once again that the linear side chain favours peptide packing and fibrillisation.

Peptide hydrogel stability against protease degradation was assayed *in vitro*. All heterochiral peptides resisted hydrolysis (<20% over five days), while non-assembling ^{L}-peptide analogs were completely digested within the first 24 hr (Fig. S72). In addition, higher peptide hydrophobicity corresponded to slower gel dissolution, with peptides bearing leucine isomers outperforming the others (Table S5), and being the only ones to persist after 72 hr in cell culture (Fig. 6B-C). The Phe-^{D}Nle-Phe samples were not homogeneous, with microscopic fibre bundles eventually segregating from the aqueous phase, in agreement with the observations discussed above. Nevertheless, the majority of cells were viable in all samples, with greatest survival in the Phe-^{D}Leu-Phe hydrogel. Overall, these results indicate that, amongst peptides tested, Phe-^{D}Leu-Phe outperformed the others as a hydrogel biomaterial, while Phe-^{D}Nle-Phe consistently led to reduced cell spreading and viability in both solution and gel forms, and was the peptide with the highest hydrophobicity and tendency towards fibrillisation. We hypothesise that the combination of these factors with the presence of both a non-natural stereoconfiguration and a non-natural side-chain resulted in

significant, although limited, detrimental effects in terms of biocompatibility, and could be ascribed to cell limited ability to process this compound and its fibrils.

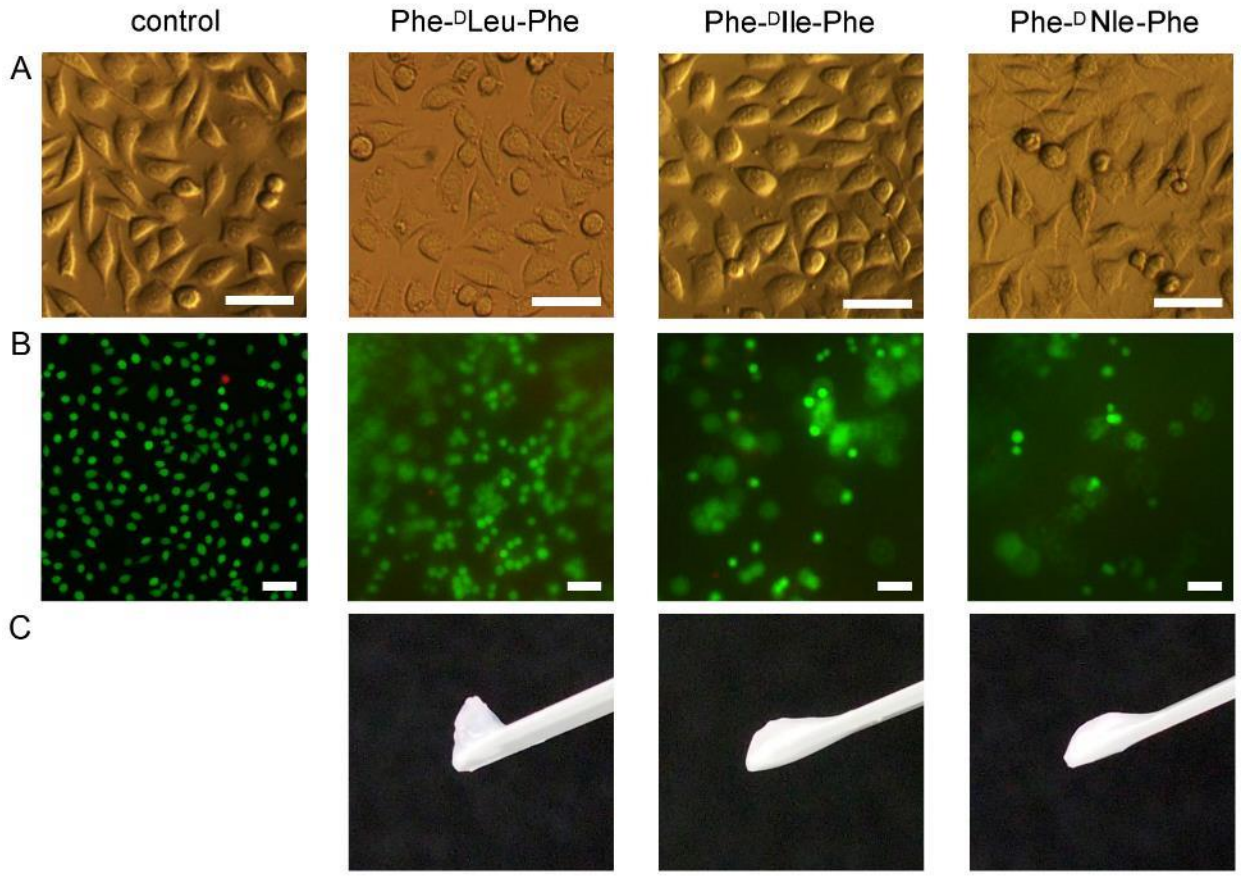

Fig. 6. Peptide performance under fibroblast cell culture conditions.

A, bright-field microscopy images of a cytotoxicity assay for peptides in solution at 2 mg ml^{-1} reveal spindle-morphology for spreading cells across all samples. **B**, live (green)/dead (red) cell staining after 72 hr culture on peptide hydrogels revealed high cell viability, and high cell numbers especially in the case of the Phe-^{D}Leu-Phe hydrogel. **C**, Photographs of peptide hydrogel samples after 72 hr under cell culture conditions. Scale bars = 50 microns.

In conclusion, we present here a general design for hydrogel biomaterials from simple D- and L-amino acids in sets of three. Although the tripeptides are composed exclusively of hydrophobic amino acids, an amphiphilic conformation emerges in the monomeric state that is crucial to self-assembly. The characteristic monomer CD signature is correlated to kinked β-strands according to Ramachandran plots,

whereby only heterochiral – not homochiral – peptides succeed in segregating hydrophobic and hydrophilic zones to enable subsequent self-assembly in water. As a result, heterochiral tripeptide backbones bend in a turn to maximise non-covalent interactions and exclude water from specific regions, resulting in the superstructures zipping together. Tripeptide assembly is elucidated at each step by *in silico* and experimental data from the monomeric state, growing to fibrils, fibres, and macroscopic materials, spanning from the Ångstrom-, to nano-, micro- and macro-scale. The viscoelastic properties of the hydrogels are thus elucidated in terms of fibre diameter and inter-connectivity, allowing correlation with amino acid side chain length and branching. Finally, fibroblast cell viability data revealed no major toxicity and highlighted the potential use of Phe-^{D}Leu-Phe hydrogel as a biomaterial. This investigation thus expands our understanding of how to use amino acid chirality in short peptides as a simple tool to design and master complex supramolecular materials. Future work will extend this approach to other sequences featuring further functional groups and chirality combinations to provide a broader set of building blocks for functional supramolecular systems.

Experimental Procedures

Peptide preparation. Tripeptides were prepared according to standard Fmoc-based solid-phase peptide synthesis and purified on reverse-phase HPLC as previously described.[43] Spectroscopic data can be found in the Supplementary Information.

Hydrogel formation. Hydrogels were prepared by dissolving each peptide in 0.1 M sodium phosphate at pH 11.8, then an equal volume of sodium phosphate 0.1 M at pH 5.8 led to hydrogel formation at a final pH 7.3 $\pm$ 0.1 within a few minutes. Peptide final concentrations used were 10 mM, unless stated otherwise.

Molecular modelling. Model structures of zwitterionic tripeptides Phe-Ala-Phe, Phe-^{D}Leu-Phe, and Phe-^{D}Ile-Phe were generated using MarvinSketch[35]. Structural analyses were performed using the AmberTools17 package[44] and the VMD1.9.3 software[45] through in-house *tcl* scripts.

All-atom MD simulations. Single peptides. Each tripeptide was centered in a cubic box so that its distance from each face was > 16 Å, and solvated with ~2,500 water molecules. The parm14SB[46] and TIP3P[47] force

fields were used to model peptides and water molecules. Structural relaxation was achieved in multi-step fashion: first, a set of restrained optimisation was performed up to 25,000 steps while applying restraints (k = 1 kcal mol^{-1} $Å^{-1}$) to: a) all non-hydrogenous atoms of the system; b) backbone atoms; c) C_α atoms. The reference structures used for steps b) and c) were the final ones from the previous step. As last step prior MD, up to 50,000 cycles of unrestrained optimisation were performed. Each system was then heated to 300 K in 1 ns via constant-pressure-temperature (NTP) MD simulations, followed by an equilibration phase of 10 ns. Starting from the equilibrated structure, an NTP MD simulation of 500 ns was performed for each system. Pressure and temperature were set to 1 atm and 300 K (after the equilibration phase) using the isotropic Berendsen barostat[48] and the Langevin thermostat [49], respectively. A time step of 2 fs was used, and periodic boundary conditions were employed. Electrostatic interactions were evaluated using the Particle Mesh Ewald scheme with a cutoff of 9.0 Å for the short-range evaluation in direct space and for Lennard-Jones interactions (with a continuum model correction for energy and pressure). **Self-assembly.** MD simulations[34] were run for 216 tripeptides whose centers of mass were placed on a cubic 6x6x6 grid of 15 Å-spaced points. Initial orientations of peptides were randomised, and the system was solvated with ~40,000 water molecules. The initial volume of the box was ~1,203 $Å^3$, leading to a peptide concentration of ~0.2 M. Systems were equilibrated as described in the previous paragraph. Starting from the equilibrated structure, three independent NTP MD simulations were performed, each of 300 ns in length.

Theoretical CD analysis. Theoretical CD spectra were calculated using the program DICHROCALC.[50] For each system, spectra were obtained as averages over 1,000 different conformations.

Microscopy. AFM[43], cryo-TEM[34] and TEM[34] images were acquired as previously described.

Cell culture assays. Cytotoxicity in solution was assessed in accordance with ISO 10993; L929 mouse fibroblast cells were seeded at 10,000 cells per well of a 96-well tissue culture plate in 100 μl of media (MEM + GlutaMAX (GIBCO)), supplemented with 1 v% NEAA (non-essential amino acids, GIBCO), 2 v% anti–anti (antimycotic– antibiotic, GIBCO), and 10 v% FBS (fetal bovine serum, SAFC Biosciences) and cultured overnight at 37 °C, 5% CO_2. Peptides were dissolved in the media with 1% DMSO at the highest

concentration possible without occurrence of precipitation or gelation and 1:1 serial dilutions were prepared; peptide solutions were sterile-filtered and 100 µl were applied to monolayers that were then cultured further for 24 h. Cells were imaged using an inverted microscope (Olympus IX71) before quantitation by reduction of resazurin (120 µl of a 1:9 solution of PrestoBlues in media for 1.5 h) and 100 µl assayed for fluorescence on a Pherastar fluorometer (ex. 540–20 nm, em. 590–20 nm). Monolayers remained subconfluent throughout. For gel studies, gel precursor solutions were prepared as indicated previously and 15 µl of each were mixed directly in triplicate wells of a ''µ-Slide angiogenesis'' uncoated (Ibidi, Germany, through DKSH Australia). Gels with lower peptide concentration were not tested to avoid premature gel dissolution during the assay. After 24 h, gels were pre-treated with 30 µl of media for 1 h. L929 cells were added to the gels (10000 cells per cm^2 in 30 µl media), and cultured at 37 °C, 5% CO_2 for up to 72 h, by handling the slides according to the manufacturers's instructions. Every 24 h, cells had 30 µl of media exchanged for fresh media. Cell viability was investigated using the LIVE/DEAD assay (Invitrogen), according to the manufacturers's instructions. Cells were imaged using an inverted microscope (Nikon Eclipse TE2000-U) for calcein (ex. 465–495 nm, em. 515–555 nm) and ethidium (ex. 510–560 nm, em. 4590 nm).

Other experimental techniques are described in the Supplementary Information. Crystallographic data of L-Phe-Ala-Phe and Phe-^{D}Nva-Phe have been deposited with the Cambridge Crystallographic Data Centre (CCDC), accession codes 1588564 and 1836198, respectively.

Author Contributions

Investigation, A.M.G., D.I., E.P., K.E.S., L.J.W., C.D., M.M., A.V.V.; Conceptualization, A.V.V. and S.M.; Writing, S.M. with contribution from all authors; Methodology, A.V.V., M.M., R.D.Z., S.M.; Supervision, R.D.Z., S.M.; Resources, M.G. and S.M.

Acknowledgements

The authors gratefully acknowledge funding from the Italian Ministry of University and Research (MIUR) through the Scientific Independence of young Researchers (SIR) program ("HOT-SPOT" project, personal research starting grant n. RBSI14A7PL for S.M.), and from Ramón Areces Foundation (A.M.G.'s fellowship). Single-crystal XRD data were acquired at the XRD1 line at Elettra Synchrothron in Trieste (Italy).

Declaration of Interests

The authors declare no competing interests.

References

1. Draper, E.R. and Adams, D.J., Low-molecular-weight gels: The state of the art, Chem, *3*, 390-410.
2. Cai, Y., Shen, H., Zhan, J., Lin, M., Dai, L., Ren, C., Shi, Y., Liu, J., Gao, J. and Yang, Z., (2017). Supramolecular "trojan horse" for nuclear delivery of dual anticancer drugs, J. Am. Chem. Soc., *139*, 2876-2879.
3. Alakpa, E.V., Jayawarna, V., Lampel, A., Burgess, K.V., West, C.C., Bakker, S.C.J., Roy, S., Javid, N., Fleming, S., Lamprou, D.A.*, et al.*, Tunable supramolecular hydrogels for selection of lineage-guiding metabolites in stem cell cultures, Chem, *1*, 298-319.
4. Wang, H., Feng, Z. and Xu, B., (2017). Bioinspired assembly of small molecules in cell milieu, Chem. Soc. Rev., *46*, 2421-2436.
5. Zhou, J., Du, X., Berciu, C., He, H., Shi, J., Nicastro, D. and Xu, B., Enzyme-instructed self-assembly for spatiotemporal profiling of the activities of alkaline phosphatases on live cells, Chem, *1*, 246-263.
6. Luo, Z., Wu, Q., Yang, C., Wang, H., He, T., Wang, Y., Wang, Z., Chen, H., Li, X., Gong, C.*, et al.*, (2017). A powerful $CD8^+$ T-cell stimulating D-tetra-peptide hydrogel as a very promising vaccine adjuvant, Adv. Mater., *29*, 1601776.
7. Scott, G.G., Mcknight, P.J., Tuttle, T. and Ulijn, R.V., (2016). Tripeptide emulsifiers, Adv. Mater., *28*, 1381-1386.
8. Lampel, A., Mcphee, S.A., Park, H.A., Scott, G.G., Humagain, S., Hekstra, D.R., Yoo, B., Frederix, P., Li, T.D., Abzalimov, R.R.*, et al.*, (2017). Polymeric peptide pigments with sequence-encoded properties, Science, *356*, 1064-1068.
9. Zaramella, D., Scrimin, P. and Prins, L.J., (2012). Self-assembly of a catalytic multivalent peptide–nanoparticle complex, J. Am. Chem. Soc., *134*, 8396-8399.
10. Tao, K., Makam, P., Aizen, R. and Gazit, E., (2017). Self-assembling peptide semiconductors, Science, *358*, doi: 10.1126/science.aam9756.
11. Ung, P. and Winkler, D.A., (2011). Tripeptide motifs in biology: Targets for peptidomimetic design, J. Med. Chem., *54*, 1111-1125.
12. Haubner, R., Gratias, R., Diefenbach, B., Goodman, S.L., Jonczyk, A. and Kessler, H., (1996). Structural and functional aspects of rgd-containing cyclic pentapeptides as highly potent and selective integrin $\alpha_v\beta_3$ antagonists, J. Am. Chem. Soc., *118*, 7461-7472.
13. Amiche, M., Delfour, A. and Nicolas, P., (1988). Structural requirements for dermorphin opioid receptor binding, Int. J. Pept. Protein Res., *32*, 28-34.
14. Henneberger, C., Papouin, T., Oliet, S.H.R. and Rusakov, D.A., (2010). Long-term potentiation depends on release of D-serine from astrocytes, Nature, *463*, 232-236.

15. Kim, P.M., Duan, X., Huang, A.S., Liu, C.Y., Ming, G.L., Song, H. and Snyder, S.H., (2010). Aspartate racemase, generating neuronal d-aspartate, regulates adult neurogenesis, Proc. Natl. Acad. Sci. U. S. A., *107*, 3175-3179.
16. Mahalakshmi, R., Balaram, P. (2006), The Use of D-Amino Acids in Peptide Design. In *D-Amino Acids*; Konno, R., Bruckner, H., D'Aniello, A., Fisher, G.H., Eds.; Nova Science Publishers, Inc. (New York); pp 415-428.
17. Gupta, J.K., Adams, D.J. and Berry, N.G., (2016). Will it gel? Successful computational prediction of peptide gelators using physicochemical properties and molecular fingerprints, Chem. Sci., *7*, 4713-4719.
18. Truong, W.T., Su, Y., Gloria, D., Braet, F. and Thordarson, P., (2015). Dissolution and degradation of fmoc-diphenylalanine self-assembled gels results in necrosis at high concentrations in vitro, Biomater. Sci., *3*, 298-307.
19. Wojciechowski, J.P., Martin, A.D., Mason, A.F., Fife, C.M., Sagnella, S.M., Kavallaris, M. and Thordarson, P., (2017). Choice of capping group in tripeptide hydrogels influences viability in the three - dimensional cell culture of tumor spheroids, ChemPlusChem, *82*, 383-389.
20. Frederix, P.W., Scott, G.G., Abul-Haija, Y.M., Kalafatovic, D., Pappas, C.G., Javid, N., Hunt, N.T., Ulijn, R.V. and Tuttle, T., (2015). Exploring the sequence space for (tri-)peptide self-assembly to design and discover new hydrogels, Nat. Chem., *7*, 30-37.
21. Pappas, C.G., Shafi, R., Sasselli, I.R., Siccardi, H., Wang, T., Narang, V., Abzalimov, R., Wijerathne, N. and Ulijn, R.V., (2016). Dynamic peptide libraries for the discovery of supramolecular nanomaterials, Nat. Nanotechnol., *11*, 960-967.
22. Zhou, J., Li, J., Du, X. and Xu, B., (2017). Supramolecular biofunctional materials, Biomaterials, *129*, 1-27.
23. Singh, V., Rai, R.K., Arora, A., Sinha, N. and Thakur, A.K., (2014). Therapeutic implication of L-phenylalanine aggregation mechanism and its modulation by d-phenylalanine in phenylketonuria, Sci. Rep., *4*, 3875.
24. Sievers, S.A., Karanicolas, J., Chang, H.W., Zhao, A., Jiang, L., Zirafi, O., Stevens, J.T., Münch, J., Baker, D. and Eisenberg, D., (2011). Structure-based design of non-natural amino-acid inhibitors of amyloid fibril formation, Nature, *475*, 96.
25. Ridler, C., (2017). Alzheimer disease: Misfolded diabetes-mellitus peptide seeds amyloid-beta aggregation, Nat. Rev. Neurol., *13*, doi:10.1038/nrneurol.2017.5.
26. Flemming, H.-C., Wingender, J., Szewzyk, U., Steinberg, P., Rice, S.A. and Kjelleberg, S., (2016). Biofilms: An emergent form of bacterial life, Nat. Rev. Micro., *14*, 563-575.
27. Banwell, E.F., Abelardo, E.S., Adams, D.J., Birchall, M.A., Corrigan, A., Donald, A.M., Kirkland, M., Serpell, L.C., Butler, M.F. and Woolfson, D.N., (2009). Rational design and application of responsive alpha-helical peptide hydrogels, Nat. Mater., *8*, 596-600.
28. Zhang, S., (2003). Fabrication of novel biomaterials through molecular self-assembly, Nat. Biotechnol., *21*, 1171-1178.
29. Zarzhitsky, S., Vinod, T.P., Jelinek, R. and Rapaport, H., (2015). Stacking interactions by two phe side chains stabilize and orient assemblies of even the minimal amphiphilic beta-sheet motif, Chem. Commun., *51*, 3154-3157.
30. Marchesan, S., Styan, K.E., Easton, C.D., Waddington, L. and Vargiu, A.V., (2015). Higher and lower supramolecular orders for the design of self-assembled heterochiral tripeptide hydrogel biomaterials, J. Mater. Chem. B, *3*, 8123-8132.
31. Marchesan, S., Easton, C.D., Styan, K., Waddington, L., Kushkaki, K., Goodall, L., Mclean, K., Forsythe, J.S. and Hartley, P.G., (2014). Chirality effects at each amino acid position on tripeptide self-assembly into hydrogel biomaterials, Nanoscale, *6*, 5172-5180.
32. Marchesan, S., Waddington, L., Easton, C.D., Winkler, D.A., Goodall, L., Forsythe, J. and Hartley, P.G., (2012). Unzipping the role of chirality in nanoscale self-assembly of tripeptide hydrogels, Nanoscale, *4*, 6752-6760.
33. Pappas, C.G., Frederix, P.W.J.M., Mutasa, T., Fleming, S., Abul-Haija, Y.M., Kelly, S.M., Gachagan, A., Kalafatovic, D., Trevino, J., Ulijn, R.V.*, et al.*, (2015). Alignment of nanostructured tripeptide gels by directional ultrasonication, Chem. Commun., *51*, 8465-8468.

34. Vargiu, A.V., Iglesias, D., Styan, K.E., Waddington, L.J., Easton, C.D. and Marchesan, S., (2016). Design of a hydrophobic tripeptide that self-assembles into amphiphilic superstructures forming a hydrogel biomaterial, Chem. Commun., *52*, 5912-5915.
35. Marvin 14.1.9 (2014). ChemAxon (http://www.chemaxon.com).
36. Amdursky, N. and Stevens, M.M., (2015). Circular dichroism of amino acids: Following the structural formation of phenylalanine, ChemPhysChem, *16*, 2768-2774.
37. He, L., Navarro, A.E., Shi, Z. and Kallenbach, N.R., (2012). End effects influence short model peptide conformation, J. Am. Chem. Soc., *134*, 1571-1576.
38. Swindells, M.B., Macarthur, M.W. and Thornton, J.M., (1995). Intrinsic [ϕ],[ψ] propensities of amino acids, derived from the coil regions of known structures, Nat. Struct. Mol. Biol., *2*, 596-603.
39. Maynard, S.J., Almeida, A.M., Yoshimi, Y. and Gellman, S.H., (2014). New charge-bearing amino acid residues that promote beta-sheet secondary structure, J. Am. Chem. Soc., *136*, 16683-16688.
40. Ramachandran, G.N., Ramakrishnan, C. and Sasisekharan, V., (1963). Stereochemistry of polypeptide chain configurations, J. Mol. Biol., *7*, 95-99.
41. De Brevern, A.G., (2016). Extension of the classical classification of beta-turns, Sci. Rep., *6*, 33191.
42. Richardson, J.S., (1981). The anatomy and taxonomy of protein structure, Adv. Protein Chem., *34*, 167-339.
43. Garcia, A.M., Kurbasic, M., Kralj, S., Melchionna, M. and Marchesan, S., (2017). A biocatalytic and thermoreversible hydrogel from a histidine-containing tripeptide, Chem. Commun., *53*, 8110-8113.
44. Case, D.A., Cerutti, D.S., Cheatham, T.E.III, Darden, T.A., Duke, R.E., Giese, T.J., Gohlke, H., Goetz, A.W., Greene, D., Homeyer, N., *et al.* (2017). AMBER 2017. University of California: San Francisco.
45. Humphrey, W., Dalke, A. and Schulten, K., (1996). Vmd - visual molecular dynamics, J. Molec. Graphics, *14*, 33-38.
46. Maier, J.A., Martinez, C., Kasavajhala, K., Wickstrom, L., Hauser, K.E. and Simmerling, C., (2015). Ff14sb: Improving the accuracy of protein side chain and backbone parameters from ff99sb, J. Chem. Theory Comput., *11*, 3696-3713.
47. Jorgensen, W.L., Chandrasekhar, J., Madura, J.D., Impey, R.W. and Klein, M.L., (1983). Comparison of simple potential functions for simulating liquid water, J. Chem. Phys., *79*, 926-935.
48. Berendsen, H.J.C., Postma, J.P.M., Van Gunsteren, W.F., Dinola, A. and Haak, J.R., (1984). Molecular-dynamics with coupling to an external bath, J. Chem. Phys., *81*, 3684-3690.
49. Feller, S.E., Zhang, Y., Pastor, R.W. and Brooks, B.R., (1995). Constant pressure molecular dynamics simulation : The langevin piston method, Time, *103*, 4613-4621.
50. Bulheller, B.M., Rodger, A. and Hirst, J.D., (2007). Circular and linear dichroism of proteins, Phys. Chem. Chem. Phys., *9*, 2020-2035.

Supporting Information for:

Chirality effects on peptide self-assembly unravelled from molecules to materials

Ana M. Garcia[1], Daniel Iglesias[1], Evelina Parisi[1], Katie E. Styan[2], Lynne J. Waddington[2], Caterina Deganutti[1], Rita De Zorzi[1], Mario Grassi[3], Michele Melchionna[1], Attilio V. Vargiu[4]*, and Silvia Marchesan[1]*

Affiliations

1. Department of Chemical & Pharmaceutical Sciences, University of Trieste, Via L. Giorgieri 1, 34127 Trieste, Italy.
2. CSIRO Manufacturing, Clayton, VIC 3168, Australia.
3. Department of Industrial Chemistry, University of Trieste, Piazzale Europa 1, 34127 Trieste, Italy.
4. Department of Physics, University of Cagliari, S.P. Monserrato-Sestu Km. 0.700, 09042 Monserrato (CA), Italy.

* Corresponding authors. Email: vargiu@dsf.unica.it, smarchesan@units.it

Table of Contents

1. Materials and Methods.

Circular Dichroism. A 0.1 mm quartz cell was used on a Jasco J815 Spectropolarimeter, with 1s integrations, 1 accumulation and a step size of 1 nm with a bandwidth of 1 nm. To follow the self-assembly kinetics, the CD signal was monitored over a range of wavelengths from 185 to 280 nm at 25°C (Peltier) every 2.5 minutes for one hour. Samples were freshly prepared directly in the CD cell and the spectra immediately recorded. After one hour of kinetics, a heating ramp of 5 ºC/min from 25ºC to 85ºC was applied to the self-assembled samples. To monitor the CD signal of the samples in solution (below the self-assembly concentration), each peptide was dissolved at a concentration of 2.5 mM in phosphate buffer pH 11.80. The spectra were recorded using the same parameters as for the hydrogels.

LC-MS analysis. LC-MS data was acquired on a Agilent 6120 LC-MS system with a C-18 analytical column (Zorbax SB-C18 Rapid Resolution HT 2.1x50 mm, particle size: 1.8 microns). Flow 0.5 ml/min. The gradient used consisted of acetonitrile (MeCN) / water with 0.1% TFA with the following program: t = 0-2 min. 25% MeCN; t = 12 min. 75% MeCN; t = 14-16 min. 95% MeCN (t_R= 7-8 min).

Peptide crystallisation. Crystals of the peptide Phe-^{D}Nva-Phe and of the peptide Phe-Ala-Phe were grown using the vapour diffusion method: the peptide solutions were dispensed in a small vial connected to a larger vial containing the reservoir solution. The peptide Phe-^{D}Nva-Phe was dissolved in methanol at 2.5 mM concentration. 800 µL were deposited in a small vial and sealed with a reservoir containing 3 mL of methanol 40%(v/v) in water, to allow vapour diffusion until equilibration. Single crystals were grown in a month. The peptide Phe-Ala-Phe was dissolved in phosphate buffer pH 11.80 at 5 mM concentration. 800µL were deposited in a small vial and put sealed in vapour diffusion with a reservoir containing 3 mL of phosphate buffer pH 7.4, to allow vapour diffusion until equilibration. Single crystals were grown upon a three-month period.

Single-crystal X-ray diffraction. Single crystals of (a) Phe-^{D}Nva-Phe and (b) ^{L}-peptide Phe-Ala-Phe were collected with loops, cryoprotected by dipping the crystal in glycerol and stored frozen in liquid nitrogen. The crystals were mounted on the diffractometer at the synchrotron Elettra, Trieste (Italy), beamline XRD1, using the robot present at the facility. Temperature was kept at 100 K by a stream of nitrogen on the crystal. Diffraction data were collected by the rotating crystal method using synchrotron radiation, wavelength 0.70 Å, rotation interval 1°/image, crystal-to-detector distance of 85 mm. A total of 180 and 270 images were collected for crystals (a) and (b), respectively. Reflections were indexed and integrated using the XDS package [1], space groups *$P6_3$* and *C2* were determined using POINTLESS [2] for crystals (a) and (b), respectively, and the resulting data sets were scaled using AIMLESS [3]. Phase information were obtained by direct methods using the software SHELXT [4]. Refinements cycles were conducted with SHELXL-14 [5], operating through the WinGX GUI [6], by full-matrix least-squares methods on F^2. Unit cell parameters and scaling statistics are reported in Table S1.

(a) Phe-^{D}Nva-Phe. The asymmetric unit contains a single molecule of the tripeptide in a general position. All the atoms within the asymmetric unit, except the hydrogen atoms, have been refined with anisotropic thermal parameters. Hydrogen atoms of the tripeptide molecule have been added at geometrically calculated positions and refined isotropically. Disordered solvent molecules present in the large cavities of the structure were too difficult to be modelled, but their contribution was taken into account using the SQUEEZE/PLATON procedure [7]. Residual electron densities corresponding to 302 electrons/cell were found in the voids of Phe-^{D}Nva-Phe crystals, corresponding to 39% of the cell volume. Refinements using reflections modified by the SQUEEZE procedure behaved well and R-factors were reduced from 15% to 7%. Refinement statistics are reported in Table S1. Crystallographic data have been deposited with the Cambridge Crystallographic Data Centre (CCDC), accession code 1836198. See Fig. S1.

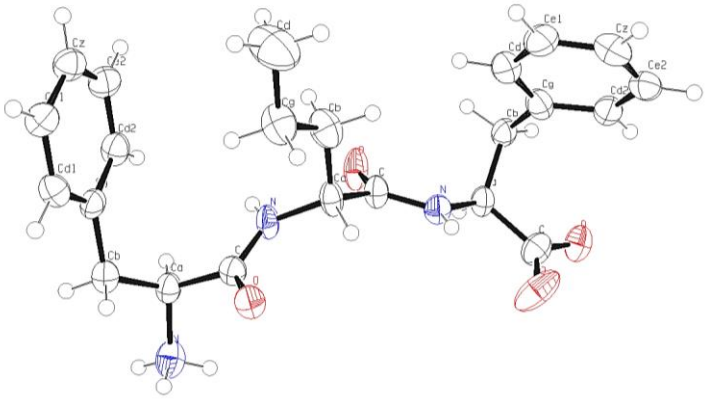

Fig. S1. Crystallographic structure of Phe-^{D}Nva-Phe with probability ellipsoids (50%). Carbon atoms are colored in gray, oxygen atoms in red, nitrogen atoms in blue and hydrogen atoms in light-gray.

(b) Phe-Ala-Phe. The asymmetric unit contains a single molecule of the tripeptide, a water molecule in a general position and a water molecule in a symmetrical position, at 50% occupancy. All the atoms within the asymmetric unit, except the hydrogen atoms, have been refined with anisotropic thermal parameters. Hydrogen atoms of the tripeptide molecule have been added at geometrically calculated positions and refined isotropically. Hydrogen atoms of water molecules were added with restrains on bond lengths and bond angle, using the DFIX and DANG cards of SHELXL-14 [5], respectively. Refinement statistics are reported in Table S1. Crystallographic data have been deposited with the Cambridge Crystallographic Data Centre (CCDC), accession code 1588564. See Fig. S2.

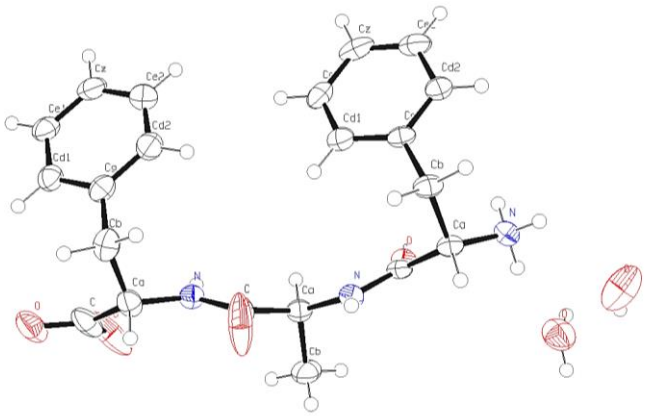

Fig. S2. Crystallographic structure of Phe-Ala-Phe with probability ellipsoids (50%). Carbon atoms are colored in gray, oxygen atoms in red, nitrogen atoms in blue and hydrogen atoms in light-gray.

Table S1: Crystallographic data.

	Phe-^{D}Nva-Phe	Phe-Ala-Phe
Formula	$C_{23}H_{29}O_4N_3$	$C_{21}H_{25}O_4N_3 \cdot 1.5H_2O$
Temperature (K)	100	100
Wavelength (Å)	0.7	0.7
Crystal system	Hexagonal	Monoclinic
Space group	*P 6$_3$*	*C 2*
a (Å)	33.377(5)	23.887(5)
b (Å)	33.377(5)	4.923(1)
c (Å)	4.975(1)	18.348(4)
⟨ (°)	90	90
® (°)	90	105.80(3)
© (°)	120	90
V (Å^3)	4800(2)	2076.1(8)
Z, ⟩calc (g/mm^3)	6, 0.892	4, 1.313
⌠ (mm^{-1})	0.078	0.00
F (000)	1320	876
Data collection ⌡ range	1.202 – 23.192	1.136 - 28.241
Refl. Collected / unique	24136 / 4642	8529 / 4869
Rint	0.1562	0.087
Completeness (%)	99.5	91.1
Data/Restraints/Parameters	4642 / 1 / 273	4869 / 6 / 282
GooF	0.938	1.092
R1, wR2 [I>2 ⌠(I)]	0.0509 / 0.1085	0.0751 / 0.1908
R1, wR2 all data	0.0831 / 0.1216	0.1043 / 0.2114
CCDC code	1836198	1588564

References:

[1] Kabsch, W. Acta Crystallogr., Sect. D. 2010, 66, 125−132.

[2] Evans, P. R. Acta Crystallogr., Sect. D. 2006, 62, 72−82.

[3] Evans, P. R., Murshudov, G. N. Acta Crystallogr., Sect. D. 2013, 69, 1204−14.

[4] Sheldrick, G. M. Acta Crystallogr., Sect. A. 2015, 71, 3–8.

[5] Sheldrick, G. M. Acta Crystallogr., Sect. C. 2015, 71, 3–8.

[6] Farrugia, L.J. J. Appl. Cryst. 2012, 45, 849−854.

[7] Spek, A.L. Acta Crystallogr., Sect. C. 2015, 71, 9-18.

ATR-IR Spectroscopy. Spectra were collected on a Varian Cary 660 spectrometer. Gel samples were spread on a 1cm^2 Silicon wafer by gently pressing a glass coverslip on top. Samples were dried for 24 hours and placed directly on the ATR Germanium crystal. Scans were performed with 128 accumulations and a resolution of 4 cm^{-1}.

Oscillatory rheometry. Rheological analyses were performed on a Haake Mars III stress-controlled rotational rheometer. The system was kept at 25°C (Peltier). Each hydrogel was prepared *in situ* on 20 mm titanium flat plates and applying a gap of 1 mm. Time sweeps were recorded for 1 hour at 1 Pa and 1 Hz, frequency sweeps were recorded at 1 Pa from 0.01 to 100 Hz and stress sweeps were recorded at 1 Hz from 1 Pa until the breaking point typical for every hydrogel, recognisable by the inversion of G' and G'' values. Each analysis was repeated at least 3 times.

Protease assay. 0.25 ml of hydrogel was prepared from each peptide as described in the main MS in 15 ml-Falcon tubes and left to self-assemble overnight. The following morning, 4.75 ml of 50 mM sodium phosphate buffer (pH 7.5) containing a large excess (5 mg) of recombinant proteinase K from Pichia pastoris (Roche – 03115879001 – 2 U/mg) were gently added on top. The tubes were incubated at 37°C, 60 rpm, and at the selected timepoints, 2 ml of NaOH 1M were added to completely disassemble the gel and inhibit further protease activity prior to HPLC analysis. Average and standard deviation values (n=3) were calculated and plotted with Excel.

2. Tripeptides spectroscopic data (NMR and MS)

a. Phe-Ala-Phe

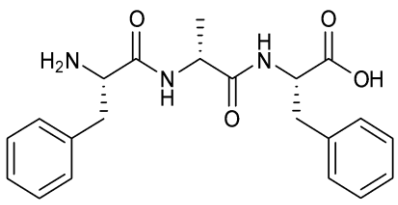

Chemical Formula: $C_{21}H_{25}N_3O_4$
Exact Mass: 383.18
Molecular Weight: 383.45

Fig. S3. Chemical structure of Phe-Ala-Phe.

^{1}H NMR (400 MHz, DMSO-d_6) δ (ppm) 12.79 (s, 1H, COOH), 8.62 (d, *J* = 7.7 Hz, 1H, NH, H-4), 8.29 (d, *J* = 7.9 Hz, 1H, NH, H-7), 8.07 (s, 3H, NH_3^+, H-1), 7.32 – 7.08 (m, 10H, Ar, H-12 – H-17; H-20 – H-25), 4.47 – 4.28 (m, 2H, 2 x αCH, H-8, H-5), 4.02 (sa, 1H, αCH, H-2), 3.06 (dd, *J* = 4.9 Hz, *Jgem* = 13.9 Hz, 1H, βCH_2, H-19a), 3.02 (d, *J* = 5.0 Hz, *Jgem* = 14.0 Hz, 1H, βCH_2, H-19b), 2.89 (dd, *J* = 8.4 Hz, *Jgem* = 13.3 Hz, 1H, βCH_2, H-11a), 2.84 (d, *J* = 7.6 Hz, *Jgem* = 13.5 Hz, 1H, βCH_2, H-11b), 1.20 (d, *J* = 7.0 Hz, 1H, 3 x βCH_3, H-18).

^{13}C NMR (100 MHz, DMSO-d_6) δ (ppm) 173.1, 172.0, 167.9 (3 x CO); 137.9, 135.3, 129.9, 129.6, 128.9, 128.6, 127.5, 126.9 (Ar); 53.9, 53.7, 48.5 (3 x αC); 37.4, 37.0 (2 x βC); 19.0 (γC).

MS (ESI) m/z 384.1 $(M+H)^+$ 406.1 $(M+Na)^+$ $C_{21}H_{25}N_3O_4$ requires 383.2.

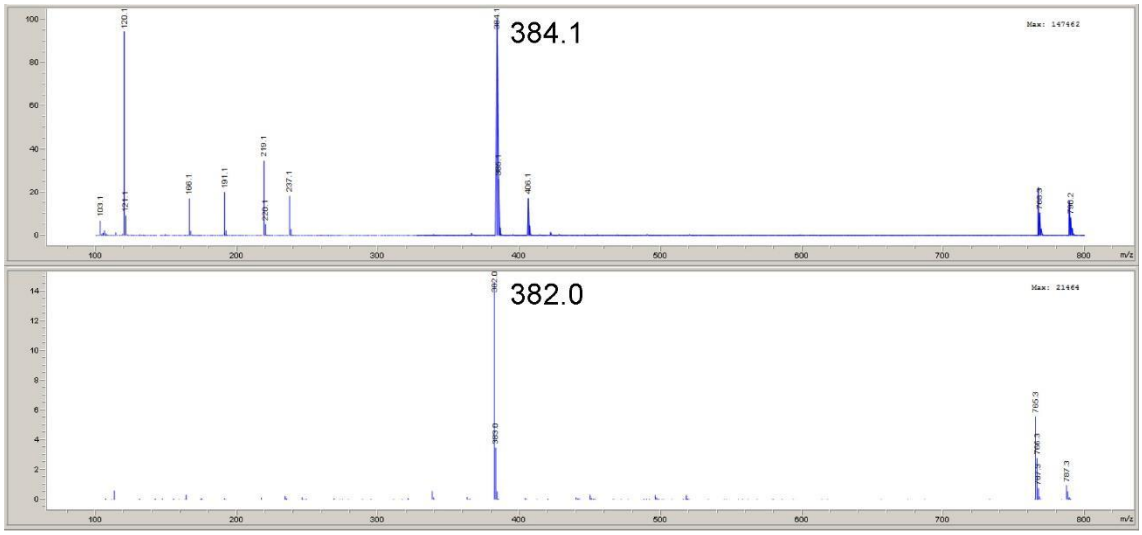

Fig. S4. ESI-MS spectra of Phe-Ala-Phe in positive (top) and negative (bottom) ion mode.

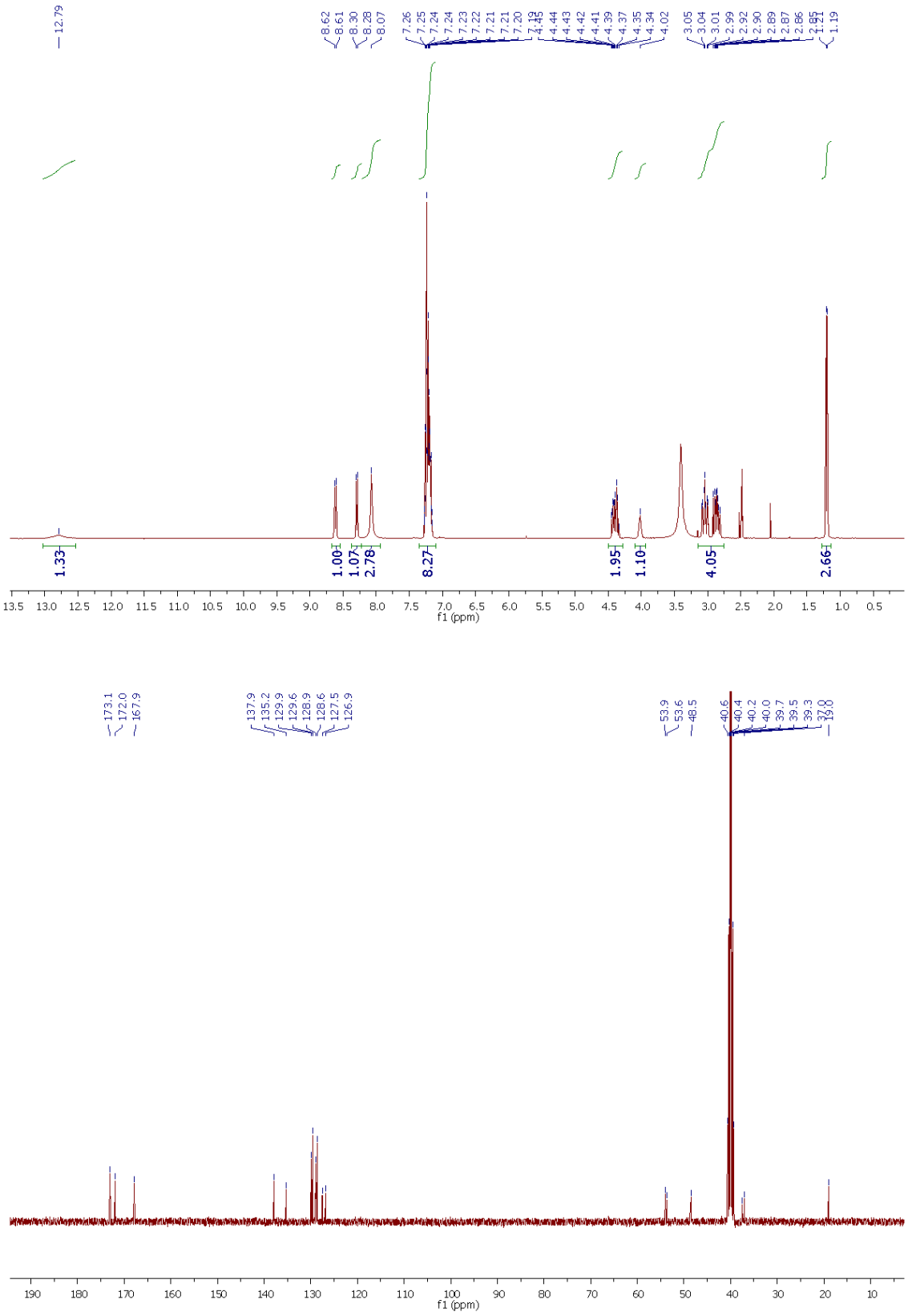

Fig. S5. ^{1}H-NMR (top) and ^{13}C-NMR (bottom) of Phe-Ala-Phe.

b. Phe-Val-Phe

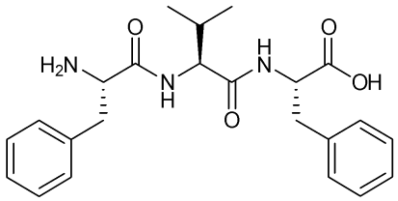

Fig. S6. Chemical structure of Phe-Val-Phe.

^{1}H NMR (400 MHz, DMSO-d_6) δ (ppm) 12.69 (s, 1H, COOH), 8.43 (d, *J* = 9.0 Hz, 1H, NH), 8.39 (d, *J* = 7.7 Hz, 1H, NH), 8.04 (s, 1H, NH_3^+), 7.39 – 6.81 (m, 10H, Ar), 4.50 (ddd, *J* = 9.3, 7.8, 5.1 Hz, 1H, αCH), 4.24 (dd, *J* = 8.9, 6.7 Hz, 1H, αCH), 4.09 (dd, *J* = 7.6, 5.2 Hz, 1H, αCH), 3.06 (dd, *J* = 5.1 Hz, *Jgem* = 14.0 Hz, 1H, βCH_2), 2.99 – 2.77 (m, *3*H, 3 x βCH_2), 1.98 – 1.88 (m, 1H, βCH_2), 0.86 (d, *J* = 6.8 Hz, 3H, 3 x γCH_3), 0.84 (d, *J* = 6.8 Hz, 3H, 3 x γCH_3).

^{13}C NMR (100 MHz, DMSO-d_6) δ (ppm) 173.2, 170.8, 168.2 (3 x CO); 138.0, 135.2, 129.9, 129.5, 128.9, 128.6, 127.5, 126.8 (Ar); 57.9, 53.9, 53.5 (3 x αC), 37.6, 37.0, 31.5 (3 x βC); 19.5, 18.6 (2 x γC).

MS (ESI) m/z 412.2 $(M+H)^+$ $C_{23}H_{29}N_3O_4$ requires 411.2

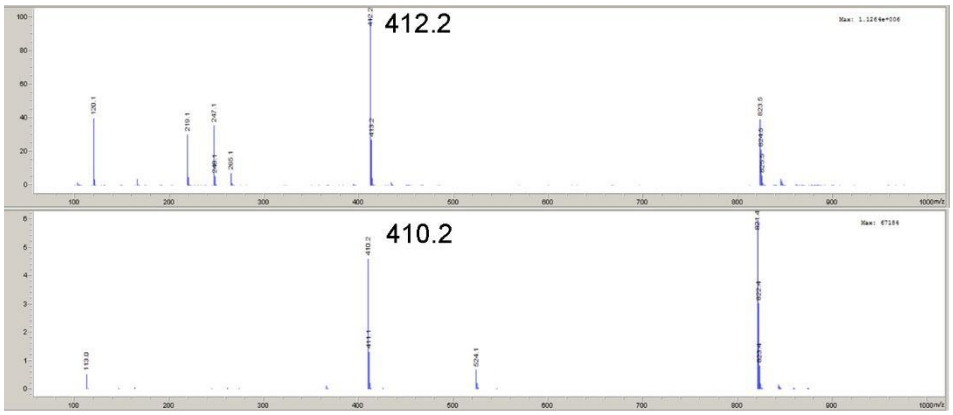

Fig. S7. ESI-MS spectra of Phe-Val-Phe in positive (top) and negative (bottom) ion mode.

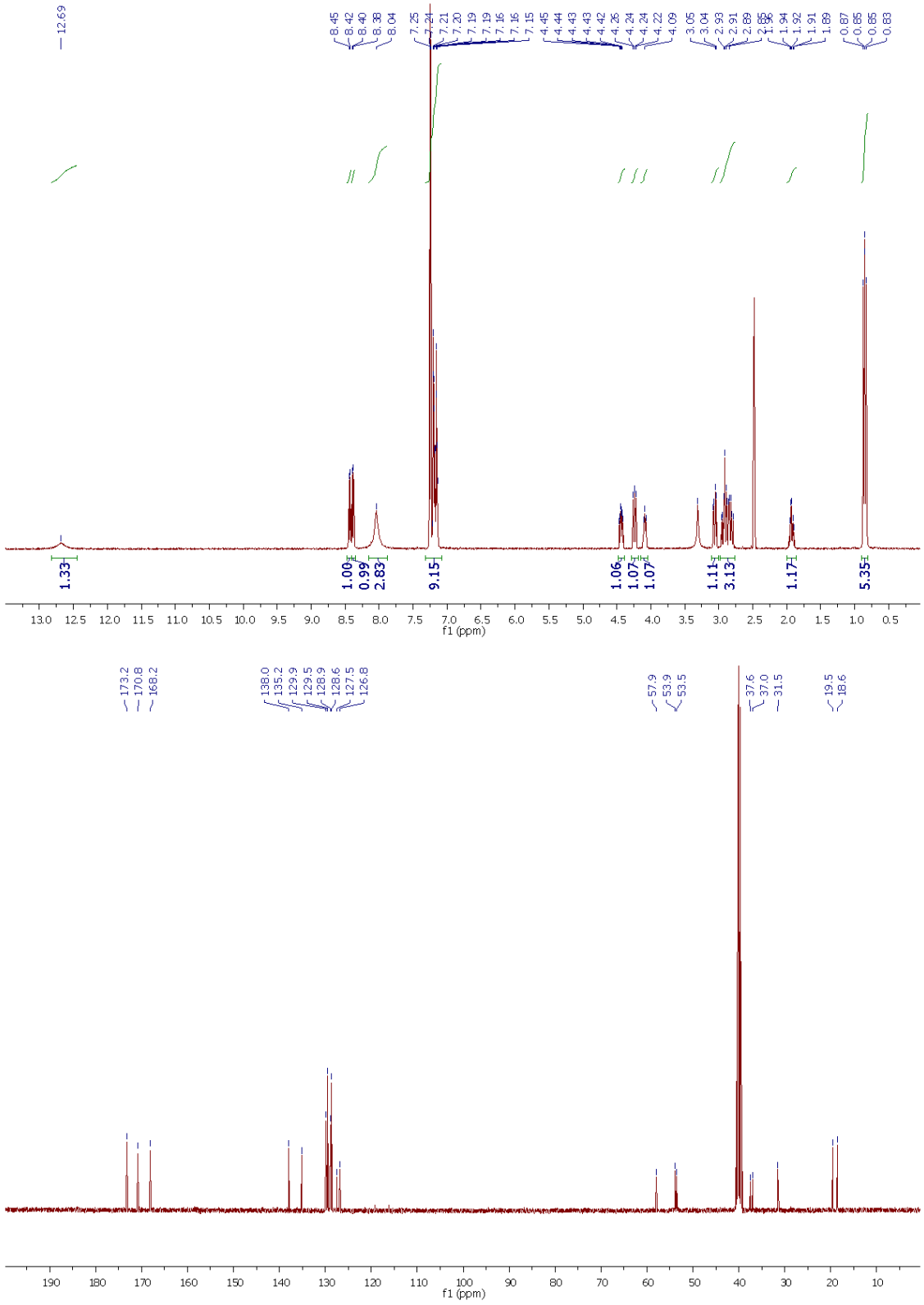

Fig. S8. ^{1}H-NMR (top) and ^{13}C-NMR (bottom) of Phe-Val-Phe.

c. Phe-Nva-Phe

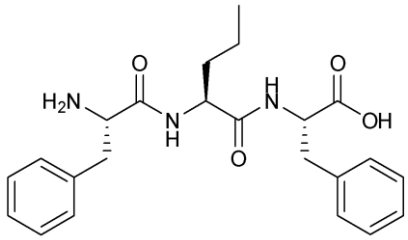

Fig. S9. Chemical structure of Phe-Nva-Phe.

^{1}H NMR (400 MHz, DMSO-d_6) δ (ppm) 8.56 (d, *J* = 8.3 Hz, 1H, NH), 8.33 (d, *J* = 7.8 Hz, 1H, NH), 7.30 – 7.09 (m, 10H, Ar), 4.49 – 4.39 (m, 1H, αCH), 4.34 (td, *J* = 8.2, 5.6 Hz, 1H, αCH), 4.03 (dd, *J* = 8.0, 5.1 Hz, 1H, αCH), 3.06 (dd, *J* = 5.0 Hz, *Jgem* = 14.0 Hz, 1H, βCH_2), 3.00 (dd, *J* = 5.0 Hz, *Jgem* = 14.1 Hz, 1H, βCH_2), 2.89 (dd, *J* = 9.4 Hz, *Jgem* = 14.2 Hz, 1H, βCH_2), 2.84 (dd, *J* = 8.4 Hz, *Jgem* = 14.4 Hz, 1H, βCH_2), 1.63 – 1.52 (m, 1H, βCH_2), 1.52 – 1.40 (m, 1H, βCH_2), 1.37 – 1.18 (m, 2H, 2 x γCH_2), 0.84 (t, *J* = 7.3 Hz, 3H, 3 x δCH_3).

^{13}C NMR (100 MHz, DMSO-d_6) δ (ppm) 173.2, 171.5, 168.2 (3 x CO); 138.0, 135.3, 129.9, 129.5, 128.9, 128.6, 127.5, 126.8 (Ar); 53.9, 53.7, 52.7 (3 x αC), 37.6, 37.0, 35.1 (2 x βC; 1 x βC); 18.7 (γC), 14.2 (δC).

MS (ESI) m/z 412.2 $(M+H)^+$ $C_{23}H_{29}N_3O_4$ requires 411.2.

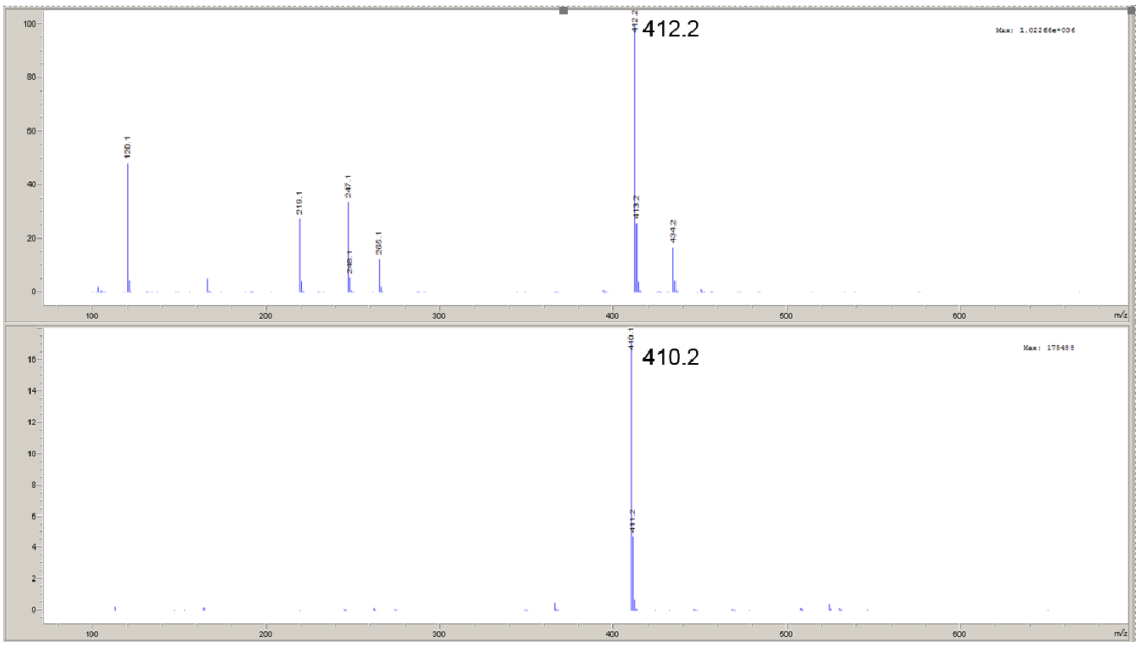

Fig. S10. ESI-MS spectra of Phe-Nva-Phe in positive (top) and negative (bottom) ion mode.

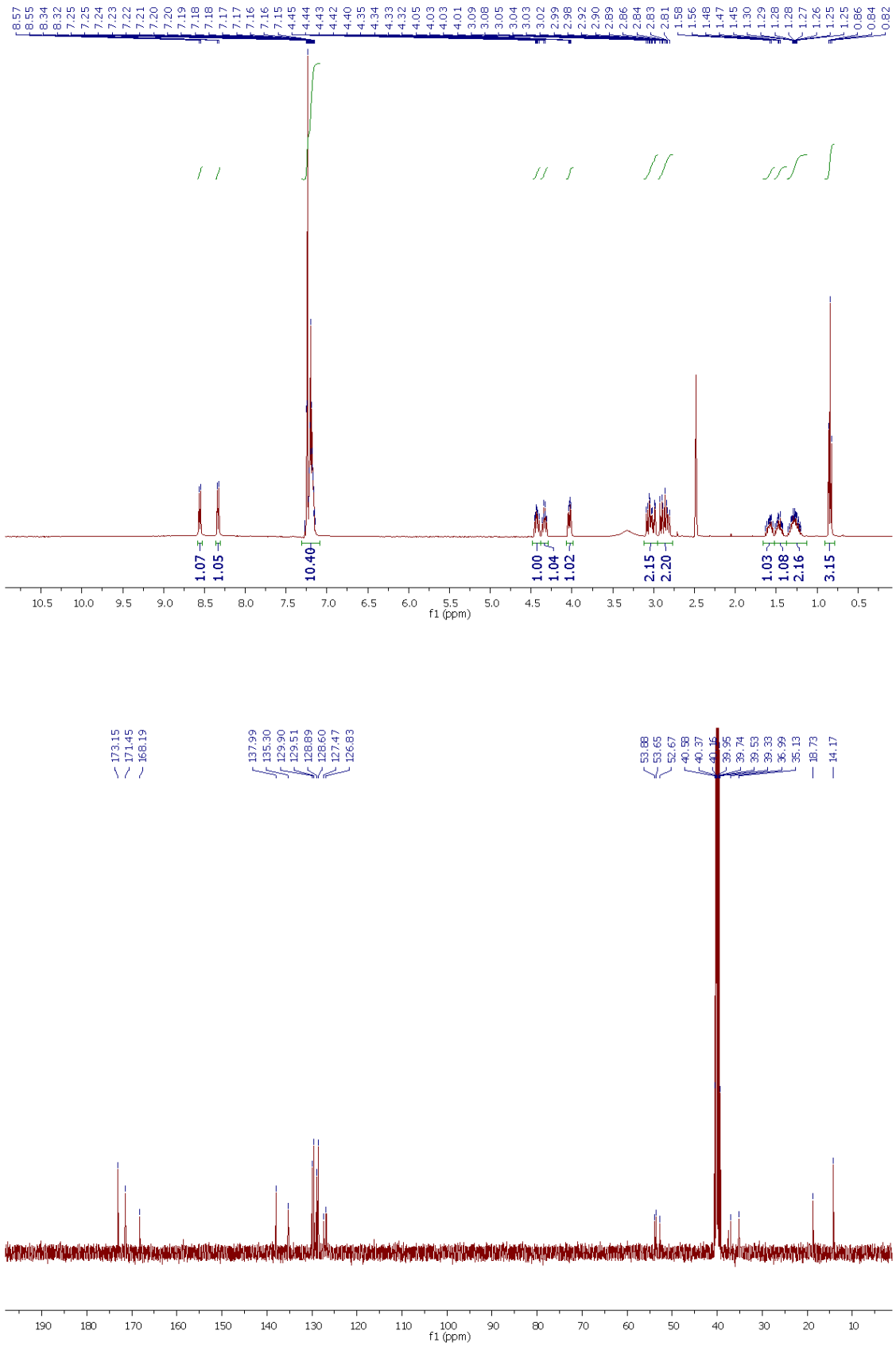

Fig. S11. ^{1}H-NMR (top) and ^{13}C-NMR (bottom) of Phe-Nva-Phe.

d. Phe-Leu-Phe

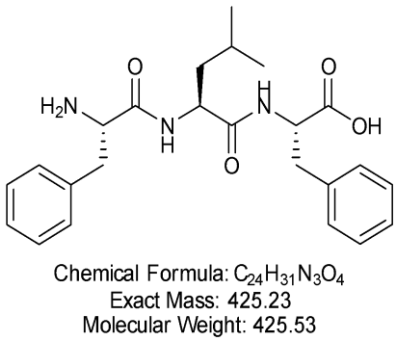

Fig. S12. Chemical structure of Phe-Leu-Phe.

^{1}H NMR (400 MHz, DMSO-d_6) δ (ppm) 8.55 (d, *J* = 8.4 Hz, 1H, NH), 8.37 (d, *J* = 7.8 Hz, 1H, NH), 7.29 – 7.11 (m, 10H, Ar), 4.47 – 4.35 (m, *2*H, αCH), 4.00 (dd, *J* = 8.2, 4.9 Hz, 1H, αCH), 3.06 (dd, *J* = 5.1 Hz, *Jgem* = 14.0 Hz, 1H, βCH$_2$), 3.00 (dd, *J* = 4.9 Hz, *Jgem* = 14.2 Hz, 1H, βCH$_2$), 2.91 (dd, *J* = 9.1 Hz, *Jgem* = 14.0 Hz, 1H, βCH$_2$), 2.82 (dd, *J* = 8.3 Hz, *Jgem* = 14.2 Hz, 1H, βCH$_2$), 1.70 – 1.52 (m, 1H, γCH$_2$), 1.50 – 1.35 (m, 2H, 2 x βCH), 0.88 (d, *J* = 6.6 Hz, 3H, 3 x δCH$_3$), 0.85 (d, *J* = 6.5 Hz, 3H, 3 x δCH$_3$).

^{13}C NMR (100 MHz, DMSO-d_6) δ (ppm) 173.1, 171.8, 168.1 (3 x CO); 138.0, 135.2, 129.9, 129.5, 128.9, 128.6, 127.5, 126.8 (Ar); 53.8, 53.6, 51.4 (3 x αC), 41.8, 37.5, 37.0 (3 x βC); 24.4, 23.5, 22.2 (γC, 2 x δC).

MS (ESI) m/z 426.2 $(M+H)^+$ $C_{24}H_{31}N_3O_4$ requires 425.2.

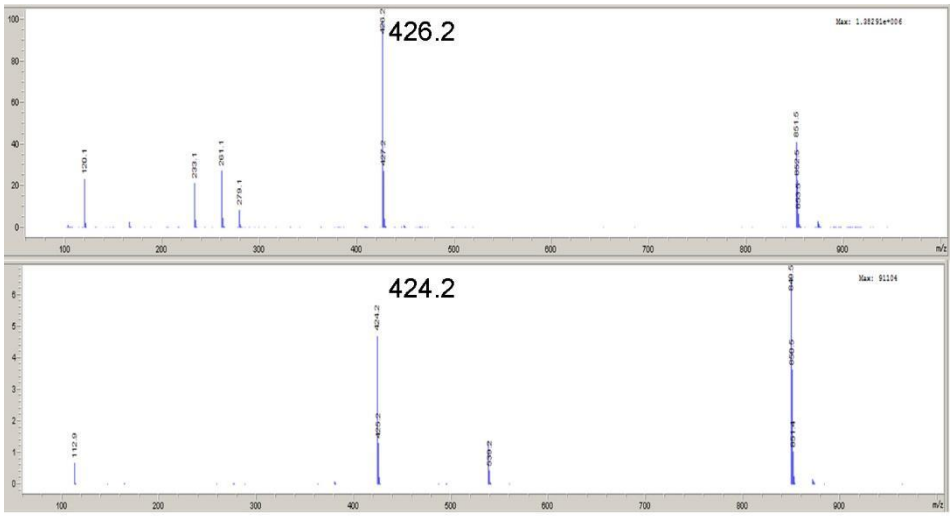

Fig. S13. ESI-MS spectra of Phe-Leu-Phe in positive (top) and negative (bottom) ion mode.

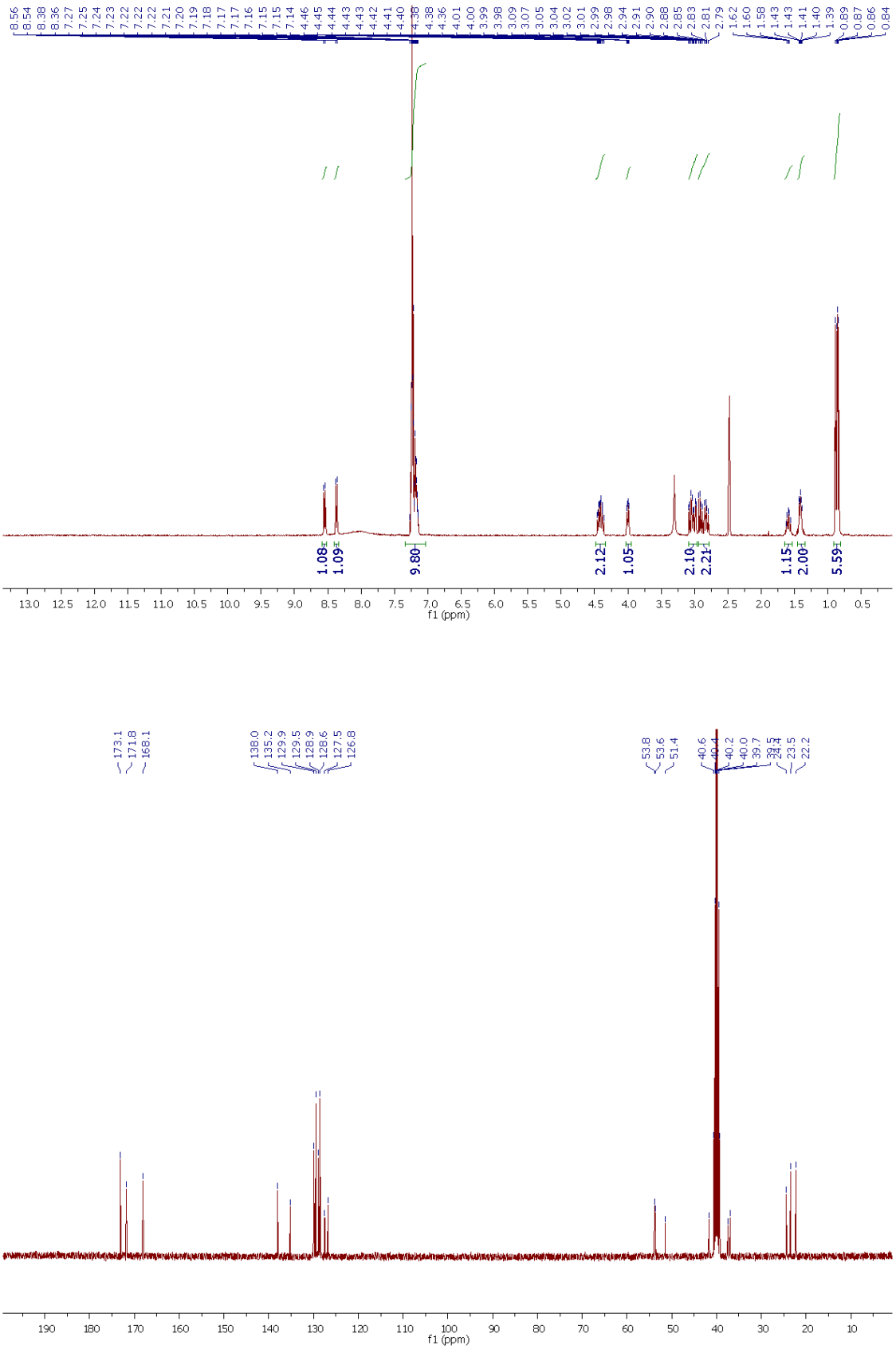

Fig. S14. ^{1}H-NMR (top) and ^{13}C-NMR (bottom) of Phe-Leu-Phe.

e. Phe-Ile-Phe

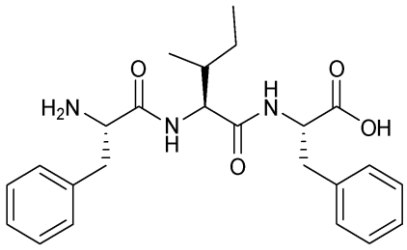

Chemical Formula: $C_{24}H_{31}N_3O_4$
Exact Mass: 425.23
Molecular Weight: 425.53

Fig. S15. Chemical structure of Phe-Ile-Phe.

^{1}H NMR (400 MHz, DMSO-d_6) δ (ppm) 12.71 (s, 1H, OH), 8.47 (d, *J* = 9.0 Hz, 1H, NH), 8.40 (d, *J* = 7.7 Hz, 1H, NH), 8.08 (s, 3H, NH_3^+), 7.27 – 7.10 (m, 10H, Ar), 4.44 (ddd, *J* = 9.2, 7.9, 5.1 Hz, 1H, αCH), 4.25 (dd, *J* = 8.8, 7.6 Hz, 1H, αCH), 4.12 – 4.02 (m, 1H, αCH), 3.06 (dd, *J* = 5.1 Hz, *Jgem* = 14.0 Hz, 1H, βCH_2), 2.98 – 2.77 (m, 3H, 3 x βCH_2), 1.73 – 1.60 (m, 1H, βCH), 1.46 (ddd, *J* = 13.4, 7.6, 3.3 Hz, 1H, γCH_2), 1.11 – 0.95 (m, 1H, γCH_2), 0.82 (d, *J* = 6.7 Hz, 3H, 3 x γCH_3), 0.79 (d, *J* = 7.5 Hz, 3H, 3 x δCH_3).

^{13}C NMR (100 MHz, DMSO-d_6) δ (ppm) 173.2, 170.8, 168.1 (3 x CO); 138.0, 135.2, 130.0, 129.5, 128.9, 128.6, 127.5, 126.8 (Ar); 57.2, 53.8, 53.5 (3 x αC), 37.8, 37.6, 37.0 (3 x βC); 24.6, 15.5 (2 x γC), 11.5 (δC).

MS (ESI) m/z 426.2 $(M+H)^+$ $C_{24}H_{31}N_3O_4$ requires 425.2.

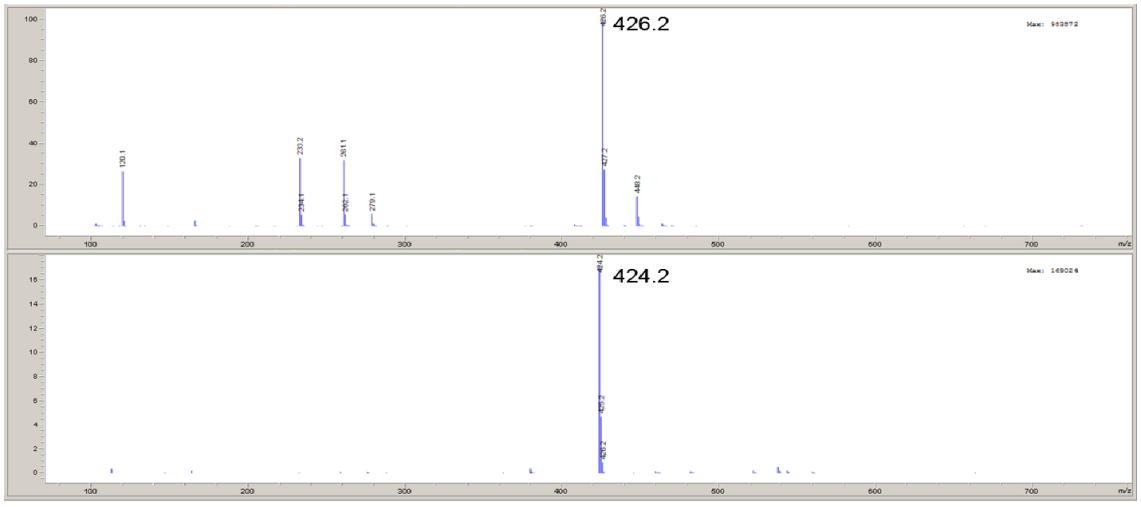

Fig. S16. ESI-MS spectra of Phe-Ile-Phe in positive (top) and negative (bottom) ion mode.

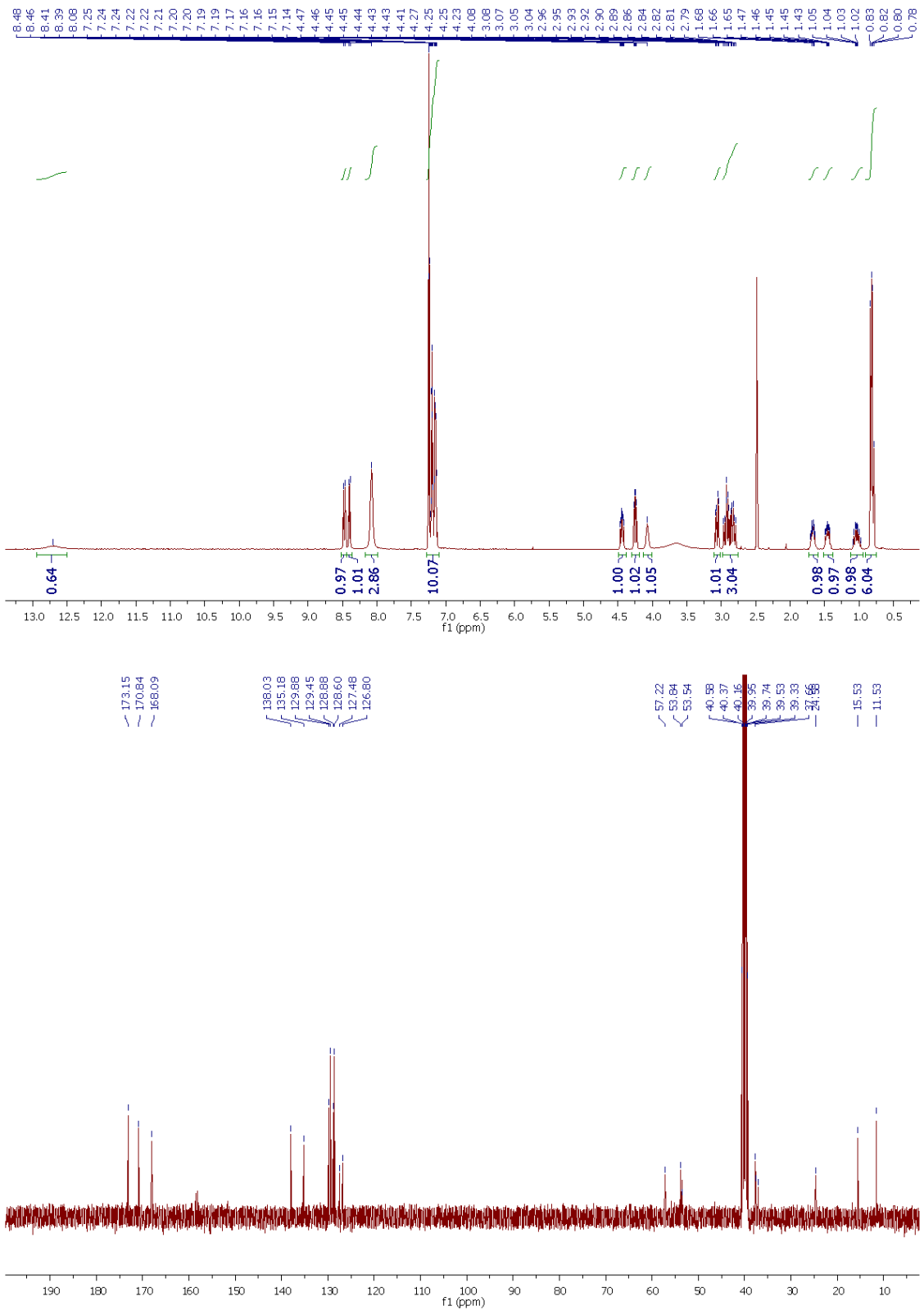

Fig. S17. ^{1}H-NMR (top) and ^{13}C-NMR (bottom) of Phe-Ile-Phe.

f. Phe-Nle-Phe

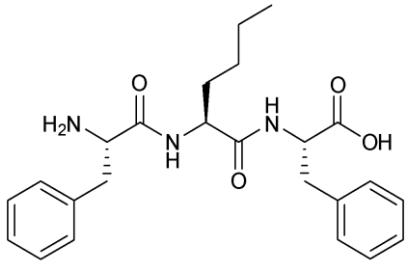

Chemical Formula: $C_{24}H_{31}N_3O_4$
Exact Mass: 425.23
Molecular Weight: 425.53

Fig. S18. Chemical structure of Phe-Ile-Phe.

^{1}H NMR (400 MHz, DMSO-d_6) δ (ppm) 12.78 (s, 1H, OH), 8.58 (d, *J* = 8.2 Hz, 1H, NH), 8.34 (d, *J* = 7.9 Hz, 1H, NH), 8.10 (s, 3H, NH_3^+), 7.52 – 6.90 (m, 10H, Ar), 4.49 – 4.38 (m, 1H, αCH), 4.32 (td, *J* = 8.0, 5.8 Hz, 1H, αCH), 4.12 – 3.97 (m, 1H, αCH), 3.07 (dd, *J* = 5.0 Hz, *Jgem* = 14.0 Hz, 1H, βCH_2), 3.01 (dd, *J* = 5.1 Hz, *Jgem* = 14.2 Hz, 1H, βCH_2), 2.90 (dd, *J* = 8.5 Hz, *Jgem* = 13.3 Hz, 1H, βCH_2), 2.84 (dd, *J* = 7.3 Hz, *Jgem* = 13.4 Hz, 1H, βCH_2),1.68 – 1.41 (m, 2H, 2 x βCH_2), 1.32 – 1.14 (m, 4H, 2 x γCH_2, 2 x δCH_2), 0.83 (t, *J* = 6.9 Hz, 3H, 3 x εCH_3).

^{13}C NMR (100 MHz, DMSO-d_6) δ (ppm) 173.2, 171.4, 168.0 (3 x CO); 138.0, 135.2, 129.9, 129.5, 128.9, 128.6, 127.5, 126.8 (Ar); 53.9, 53.6, 52.9 (3 x αC); 37.5, 37.0, 32.7 (3 x βC); 27.6 (γC), 22.4 (δC), 14.3 (εC).

MS (ESI) m/z 426.2 $(M+H)^+$ $C_{24}H_{31}N_3O_4$ requires 425.2.

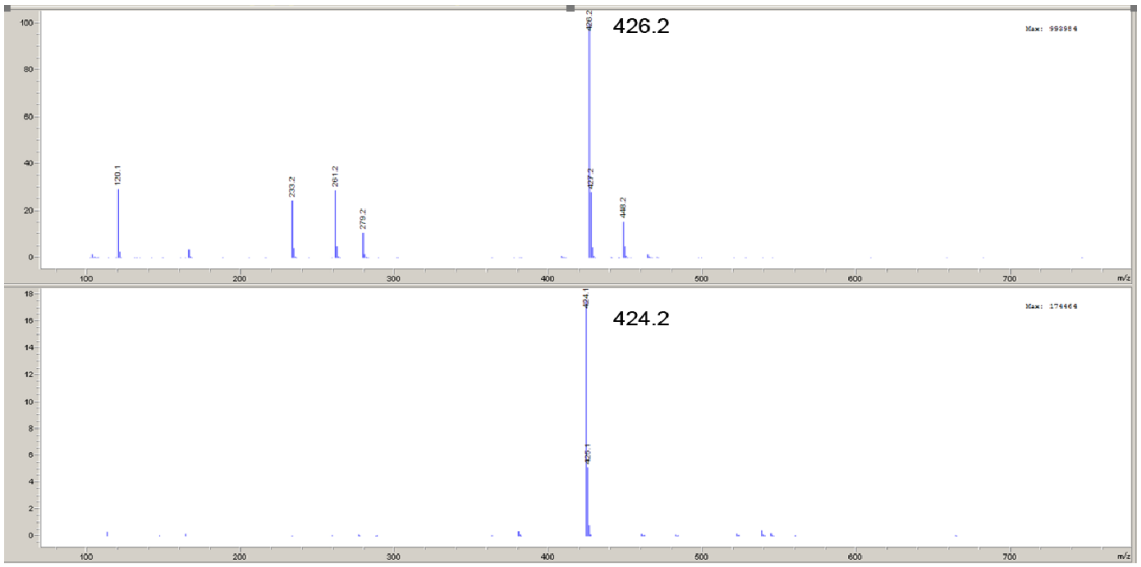

Fig. S19. ESI-MS spectra of Phe-Nle-Phe in positive (top) and negative (bottom) ion mode.

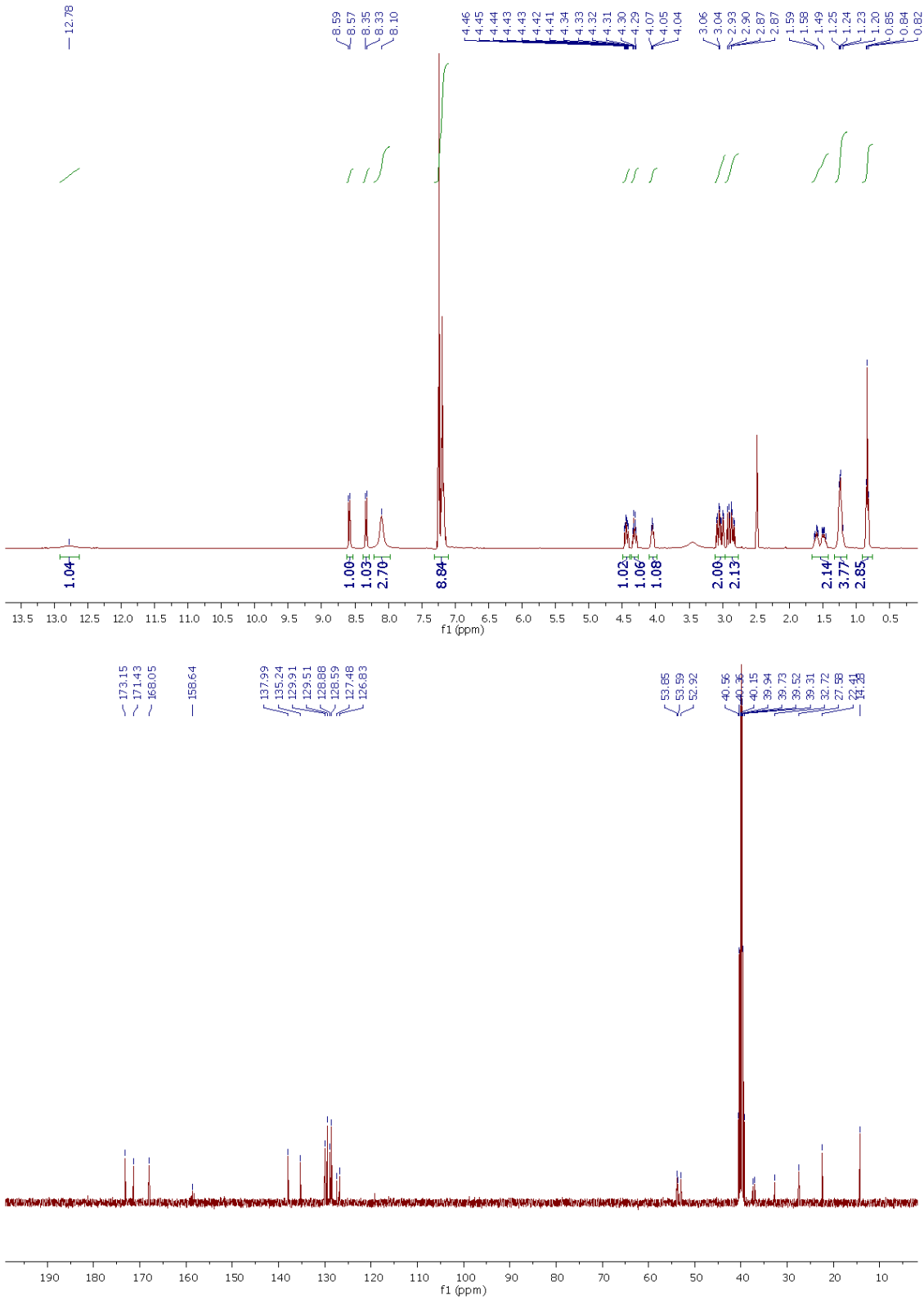

Fig. S20. ^{1}H-NMR (top) and ^{13}C-NMR (bottom) of Phe-Nle-Phe.

g. Phe-^{D}Ala-Phe

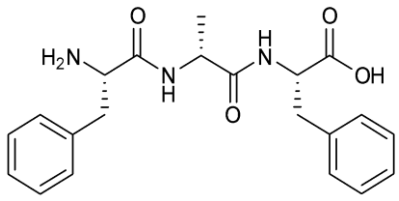

Fig. S21. Chemical structure of Phe-^{D}Ala-Phe.

^{1}H NMR (500 MHz, DMSO-d_6) δ (ppm) 8.43 (d, *J* = 8.1 Hz, 2H, 2 x NH), 8.19 (s, 3H, NH_3^+), 7.51 – 6.75 (m, 10H, Ar), 4.44 (td, *J* = 9.9, 4.6 Hz 1H, αCH), 4.34 (p, *J* = 6.9 Hz, 1H, αCH), 4.08 (t, *J* = 7.1 Hz, 1H, αCH), 3.08 (dd, *J* = 4.4 Hz, *Jgem* = 13.7 Hz, 1H, βCH_2), 2.96 (d, *J* = 7.1 Hz, *2*H, 2 x βCH_2), 2.79 (dd, *J* = 10.4 Hz, *Jgem* = 13.5 Hz, 1H, βCH_2), 0.73 (t, *J* = 6.9 Hz, 1H, 3 x βCH_3).

^{13}C NMR (125 MHz, DMSO-d_6) δ (ppm) 173.3, 171.7, 167.5 (3 x CO); 137.8, 135.2, 130.0, 129.6, 128.8, 128.5, 127.5, 126.8 (Ar); 53.5, 53.4, 48.2 (3 x αC), 37.6, 37.4 (2 x βC); 19.2 (γC).

MS (ESI) m/z 384.0 $(M+H)^+$ 406.1 $(M+Na)^+$ $C_{21}H_{25}N_3O_4$ requires 383.2.

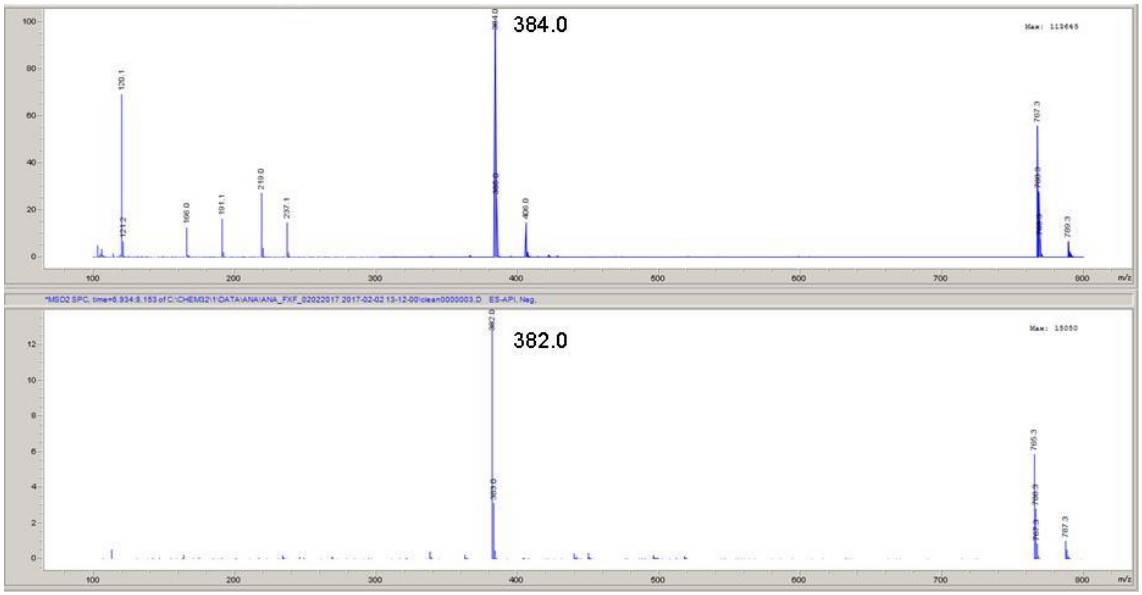

Fig. S22. ESI-MS spectra of Phe-^{D}Ala-Phe in positive (top) and negative (bottom) ion mode.

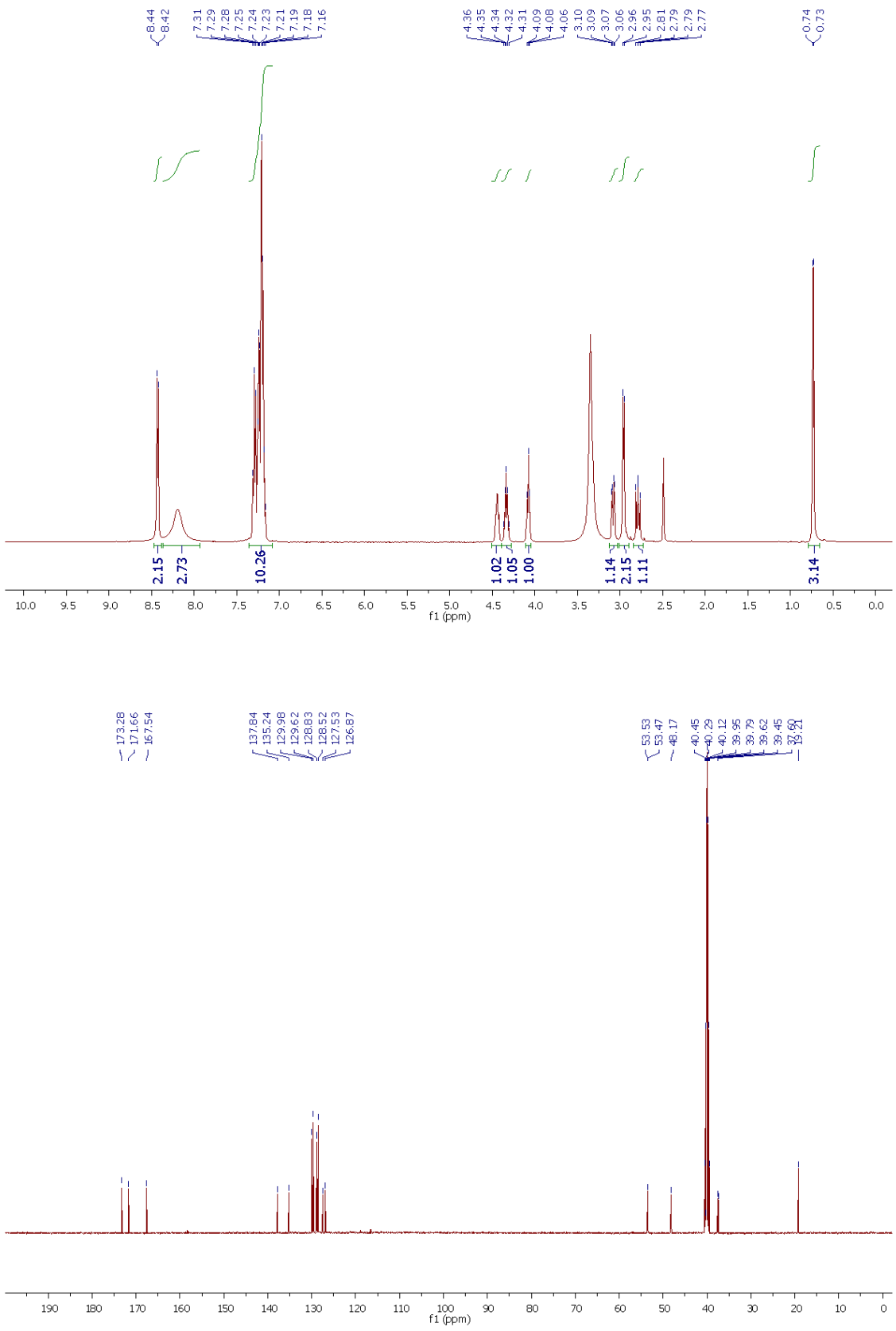

Fig. S23. 1H-NMR (top) and 13C-NMR (bottom) of Phe-^{D}Ala-Phe.

h. Phe-^{D}Val-Phe

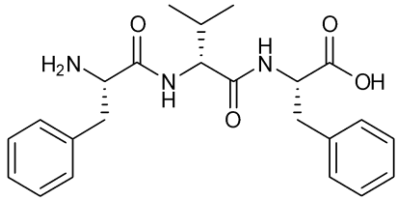

Fig. S24. Chemical structure of Phe-^{D}Val-Phe.

^{1}H NMR (500 MHz, DMSO-d_6) δ (ppm) 8.49 (d, *J* = 8.4 Hz, 1H, NH), 8.41 (d, *J* = 9.1 Hz, 1H, NH), 7.34 – 7.14 (m, 10H, Ar), 4.50 (ddd, *J* = 10.5, 8.5, 4.5 Hz, 1H, αCH), 4.32 (dd, *J* = 9.0, 5.4 Hz, 1H, αCH), 4.19 (dd, *J* = 8.1, 6.6 Hz, 1H, αCH), 3.09 (dd, *J* = 4.5 Hz, *Jgem* = 13.8 Hz, 1H, βCH_2), 3.03 (dd, *J* = 6.3 Hz, *Jgem* = 13.8 Hz, 1H, βCH_2), 2.89 (dd, *J* = 8.4 Hz, *Jgem* = 13.8 Hz, 1H, βCH_2), 2.78 (dd, *J* = 10.5 Hz, *Jgem* = 13.8 Hz, 1H, βCH_2), 1.73–1.48 (m, 1H, βC), 0.44 (d, *J* = 6.8 Hz, 3H, γCH_3), 0.36 (d, *J* = 6.8 Hz, 3H, γCH_3).

^{13}C NMR (125 MHz, DMSO-d_6) δ (ppm) 173.4, 170.4, 168.5 (3 x CO); 137.9, 135.4, 129.9, 129.5, 128.9, 128.6, 127.6, 126.8 (Ar); 57.3, 53.8, 53.7 (3 x αC), 38.1, 37.5, 31.7 (3 x βC); 19.3, 17.5 (2 x γC).

MS (ESI) m/z 412.0 $(M+H)^+$ 434.1 $(M+Na)^+$ $C_{23}H_{29}N_3O_4$ requires 411.2

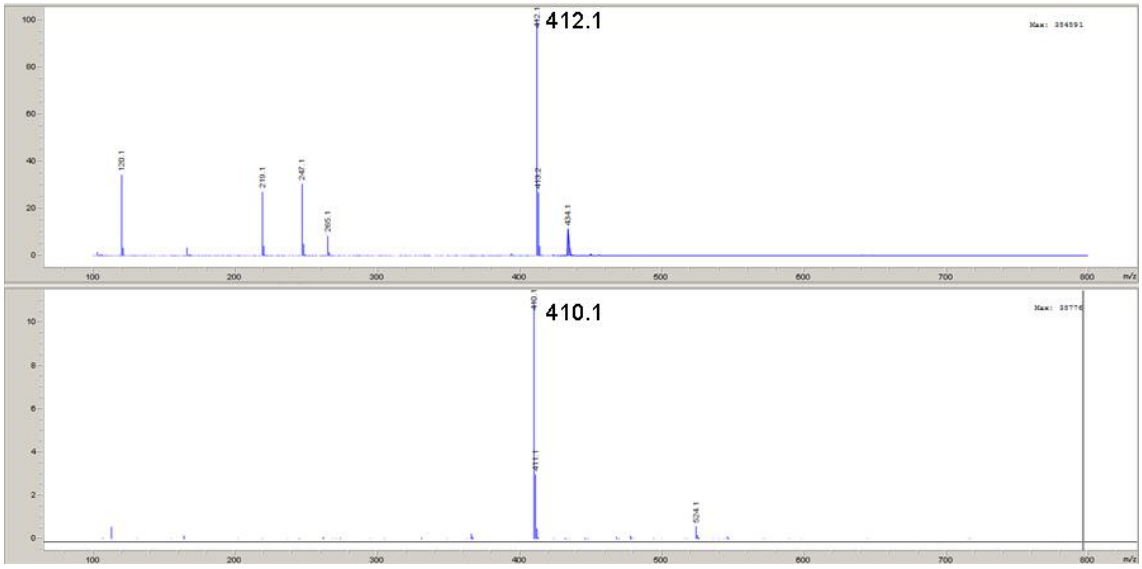

Fig. S25. ESI-MS spectra of Phe-^{D}Val-Phe in positive (top) and negative (bottom) ion mode.

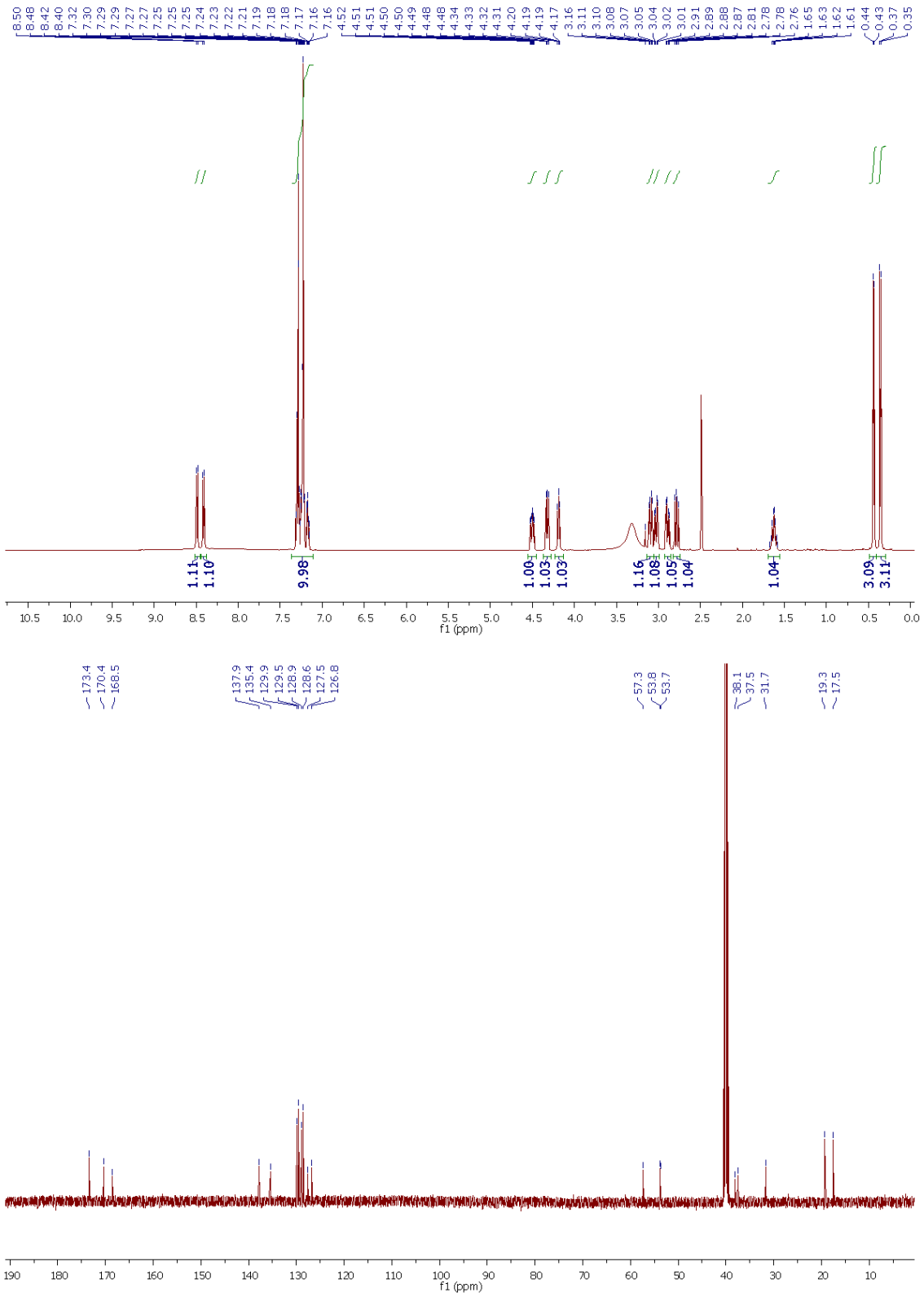

Fig. S26. ^{1}H-NMR (top) and ^{13}C-NMR (bottom) of Phe-^{D}Val-Phe.

i. Phe-^{D}Nva-Phe

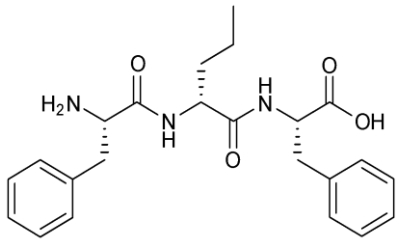

Chemical Formula: $C_{23}H_{29}N_3O_4$
Exact Mass: 411.22
Molecular Weight: 411.50

Fig. S27. Chemical structure of Phe-^{D}Nva-Phe.

^{1}H NMR (500 MHz, DMSO-d_6) δ (ppm) 8.47 (d, *J* = 8.4 Hz, 1H, NH), 8.41 (d, *J* = 8.3 Hz, 1H, NH), 7.36 – 7.10 (m, 10H, Ar), 4.53–4.39 (m, 1H, αCH), 4.32 (dd, *J* = 13.8, 6.8 Hz, 1H, αCH), 4.12 (t, *J* = 7.2 Hz, 1H, αCH), 3.09 (dd, *J* = 3.9 Hz, *Jgem* = 13.6 Hz, 1H, βCH$_2$), 2.95 (dd, *J* = 7.0 Hz, *2*H, 2 x βCH$_2$), 2.85–2.71 (m, 1H, βCH$_2$), 1.15–0.96 (m, 2H, 2 x βCH$_2$), 0.70–0.50 (m, 5H, 2 x γCH$_2$, 3 x δCH$_3$).

^{13}C NMR (125 MHz, DMSO-d_6) δ (ppm) 173.4, 171.0, 167.9 (3 x CO); 137.9, 135.3, 129.9, 129.6, 128.8, 128.5, 127.5, 126.8 (Ar); 53.7, 53.5, 52.3 (3 x αC), 37.8, 37.4, 35.3 (2 x βC; 1 x βC); 18.0 (γC), 14.1 (δC).

MS (ESI) m/z 412.1 $(M+H)^+$ 434.1 $C_{24}H_{31}N_3O_4$ requires 411.2

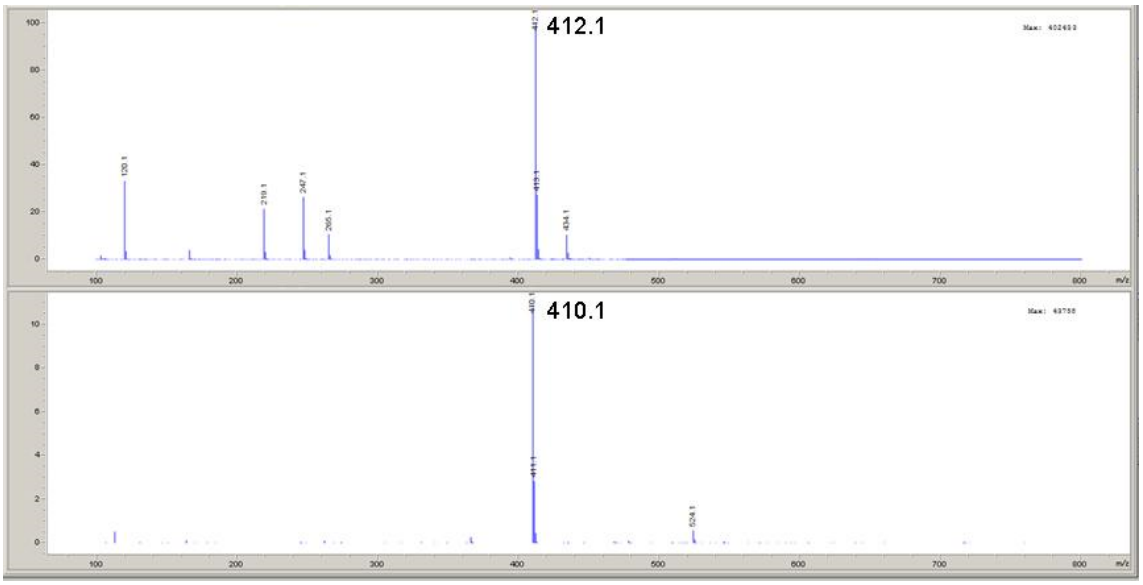

Fig. S28. ESI-MS spectra of Phe-^{D}Nva-Phe in positive (top) and negative (bottom) ion mode.

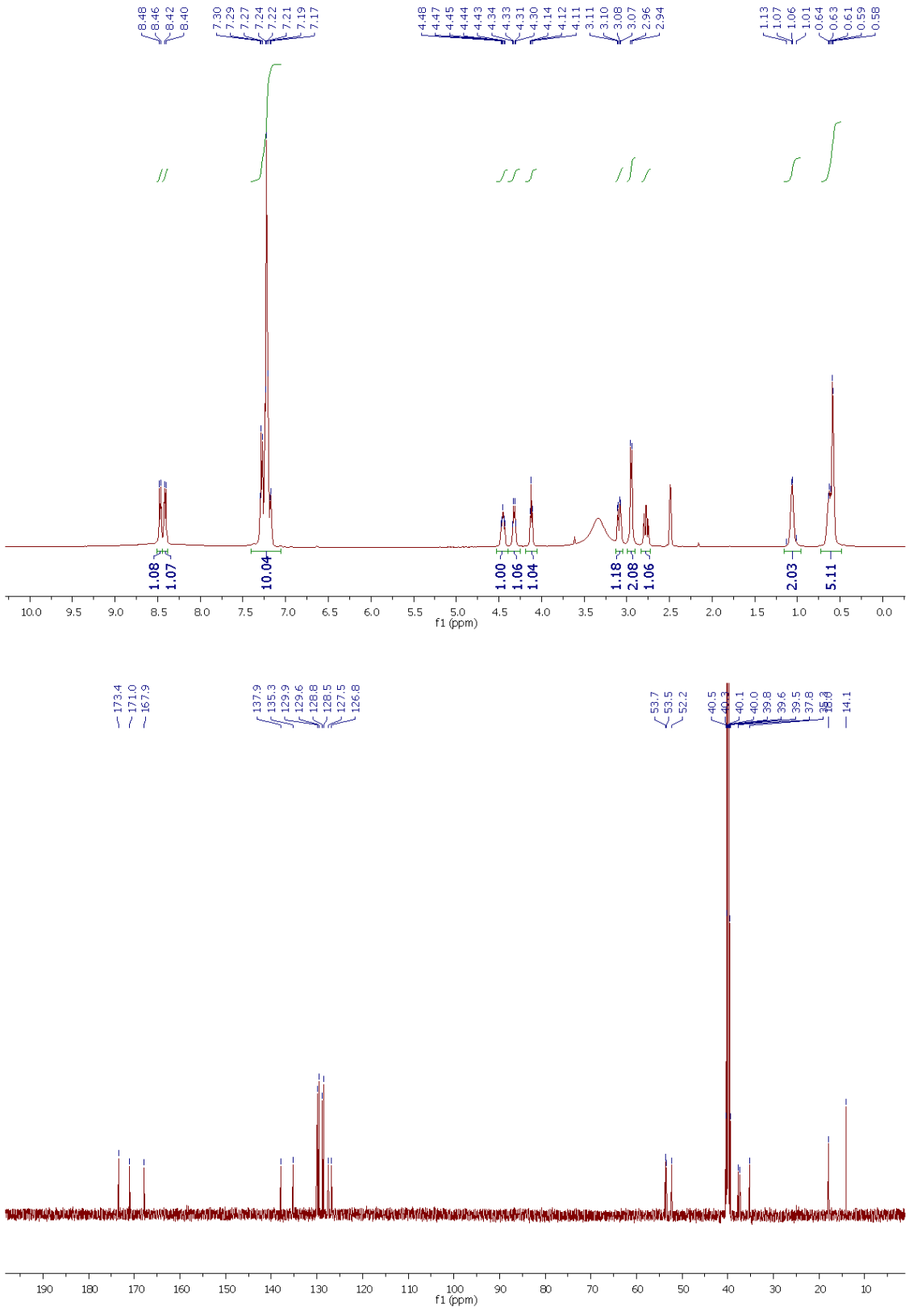

Fig. S29. ^{1}H-NMR (top) and ^{13}C-NMR (bottom) of Phe-^{D}Nva-Phe.

j. Phe-^{D}Leu-Phe

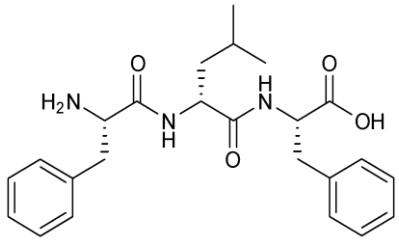

Chemical Formula: $C_{24}H_{31}N_3O_4$
Exact Mass: 425.23
Molecular Weight: 425.53

Fig. S30. Chemical structure of Phe-^{D}Leu-Phe.

^{1}H NMR (500 MHz, DMSO-d_6) δ (ppm) 8.51 (d, *J* = 8.5 Hz, 1H, NH), 8.42 (d, *J* = 8.6 Hz, 1H, NH), 7.32 – 7.14 (m, 10H, Ar), 4.43 (ddd, *J* = 10.6, 8.6, 4.5 Hz, 1H, αCH), 4.33 (dt, *J* = 13.8, 6.8 Hz, 1H, αCH), 4.02 (t, *J* = 7.2 Hz, 1H, αCH), 3.08 (dd, *J* = 4.4 Hz, *Jgem* = 13.7 Hz, 1H, βCH$_2$), 2.97 (dd, *J* = 6.7 Hz, *Jgem* = 13.7 Hz, 1H, βCH$_2$), 2.89 (dd, *J* = 7.8 Hz, *Jgem* = 13.7 Hz, 1H, βCH$_2$), 2.78 (dd, *J* = 10.7 Hz, *Jgem* = 13.6 Hz, 1H, βCH$_2$), 1.07 – 0.84 (m, 3H, 2 x βCH, γCH$_2$), 0.64 (d, *J* = 5.7 Hz, 6H, 6 x δCH$_3$).

^{13}C NMR (125 MHz, DMSO-d_6) δ (ppm) 173.5, 171.7, 168.3 (3 x CO); 138.0, 135.5, 129.9, 129.7, 128.8, 128.5, 127.5, 126.8 (Ar); 53.9, 53.8, 51.1 (3 x αC), 42.1, 38.0, 37.5 (3 x βC); 24.1, 23.4, 22.0 (γC, 2 x δC).

MS (ESI) m/z 426.1 $(M+H)^+$ 448.1 $(M+Na)^+$ $C_{24}H_{31}N_3O_4$ requires 425.2.

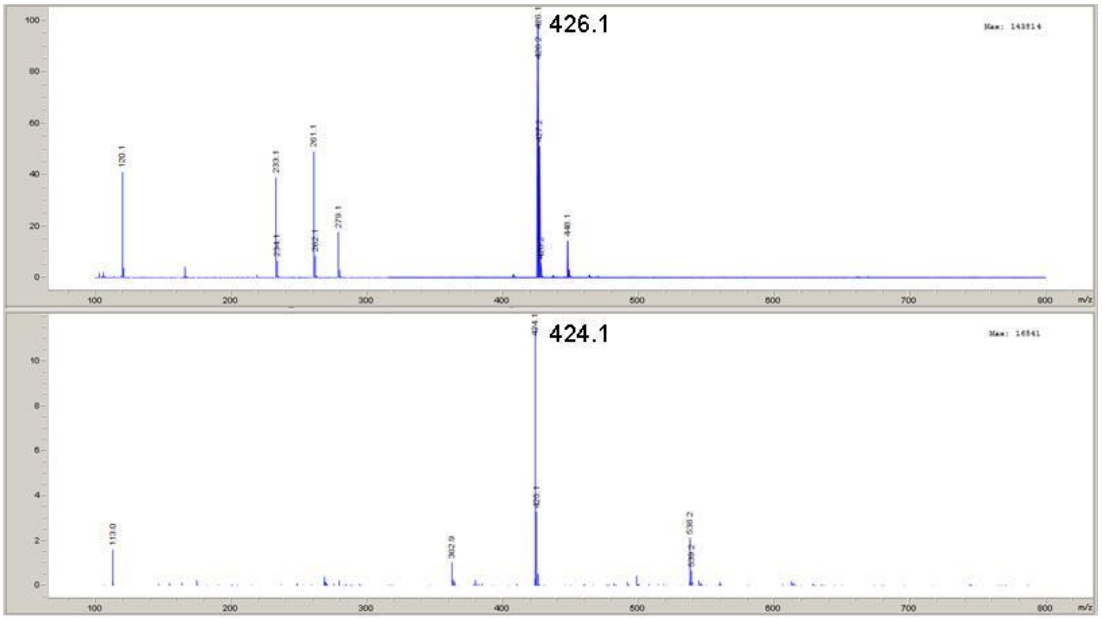

Fig. S31. ESI-MS spectra of Phe-^{D}Leu-Phe in positive (top) and negative (bottom) ion mode.

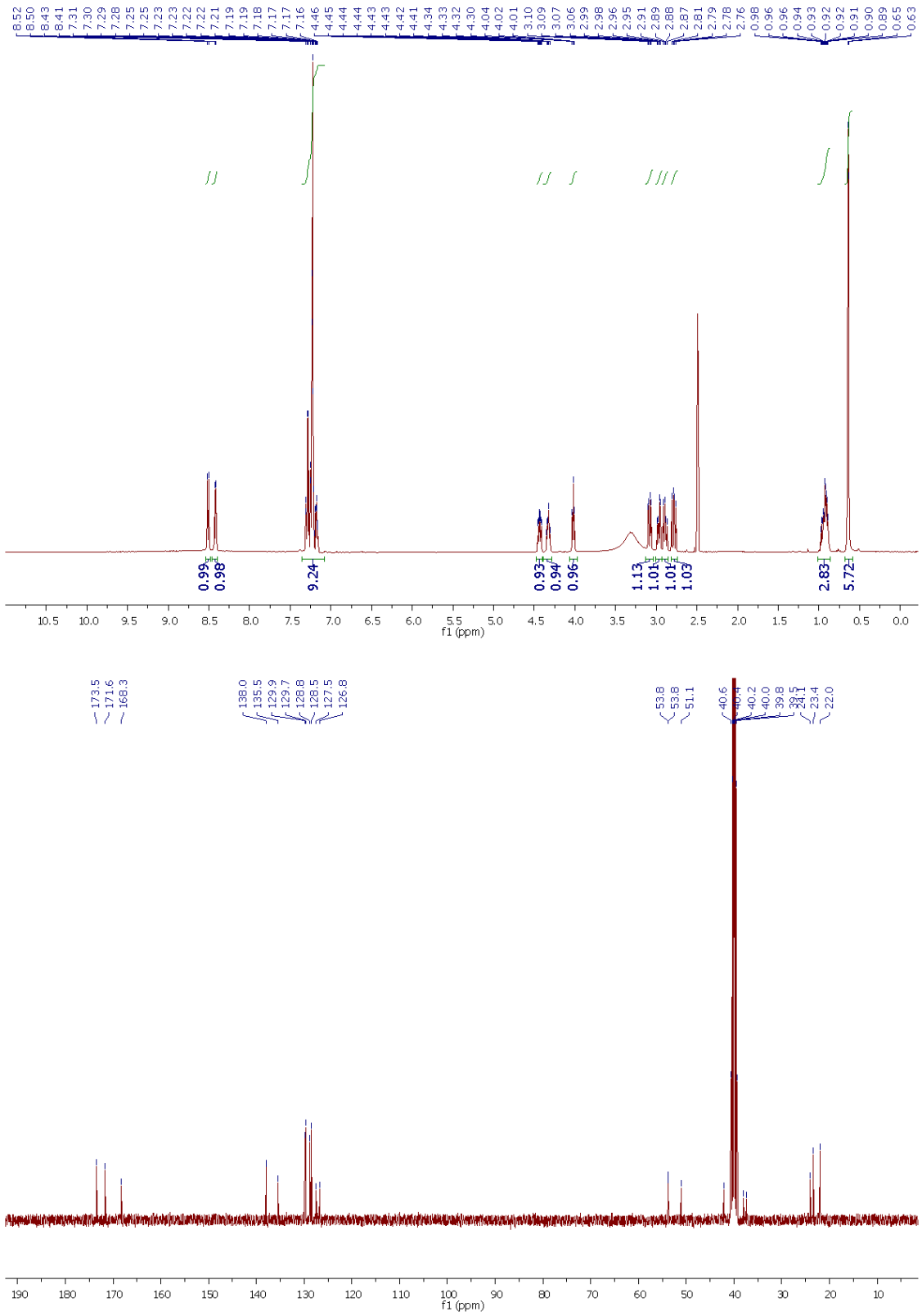

Fig. S32. ^{1}H-NMR (top) and ^{13}C-NMR (bottom) of Phe-^{D}Leu-Phe.

k. Phe-^{D}Ile-Phe

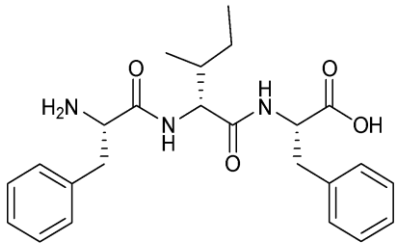

Chemical Formula: $C_{24}H_{31}N_3O_4$
Exact Mass: 425,23
Molecular Weight: 425,53

Fig. S33. Chemical structure of Phe-^{D}Ile-Phe.

^{1}H NMR (500 MHz, DMSO-d_6) δ (ppm) 8.50 (d, *J* = 8.3 Hz, 1H, NH), 8.41 (d, *J* = 9.0 Hz, 1H, NH), 7.57 – 6.96 (m, 10H, Ar), 4.48 (td, *J* = 10.6, 4.4 Hz, 1H, αCH), 4.34 (dd, *J* = 8.8, 5.8 Hz, 1H, αCH), 4.20 (t, *J* = 7.3 Hz, 1H, αCH), 3.08 (dd, *J* = 4.2 Hz, *Jgem* = 13.8 Hz, 1H, βCH_2), 3.01 (dd, *J* = 6.6 Hz, *Jgem* = 13.7 Hz, 1H, βCH_2), 2.91 (dd, *J* = 8.1 Hz, *Jgem* = 13.7 Hz, 1H, βCH_2), 2.78 (dd, *J* = 10.8 Hz, *Jgem* = 13.7 Hz, 1H, βCH_2), 1.42 – 1.24 (m, 1H, βCH), 1.01 – 0.80 (m, 1H, γCH_2), 0.63 – 0.46 (m, 4H, 4 x γCH), 0.38 (d, *J* = 6.8 Hz, 3H, 3 x δCH_3).

^{13}C NMR (125 MHz, DMSO-d_6) δ (ppm) 173.5, 170.4, 168.2 (3 x CO); 137.9, 135.3, 129.9, 129.5, 128.9, 128.6, 127.5, 126.8 (Ar); 56.8, 53.9, 53.6 (3 x αC), 38.0, 37.9, 37.3 (3 x βC); 23.8, 15.3 (2 x γC), 11.6 (δC).

MS (ESI) m/z 426.2 $(M+H)^+$ 448.2 $(M+Na)^+$ $C_{24}H_{31}N_3O_4$ requires 425.2.

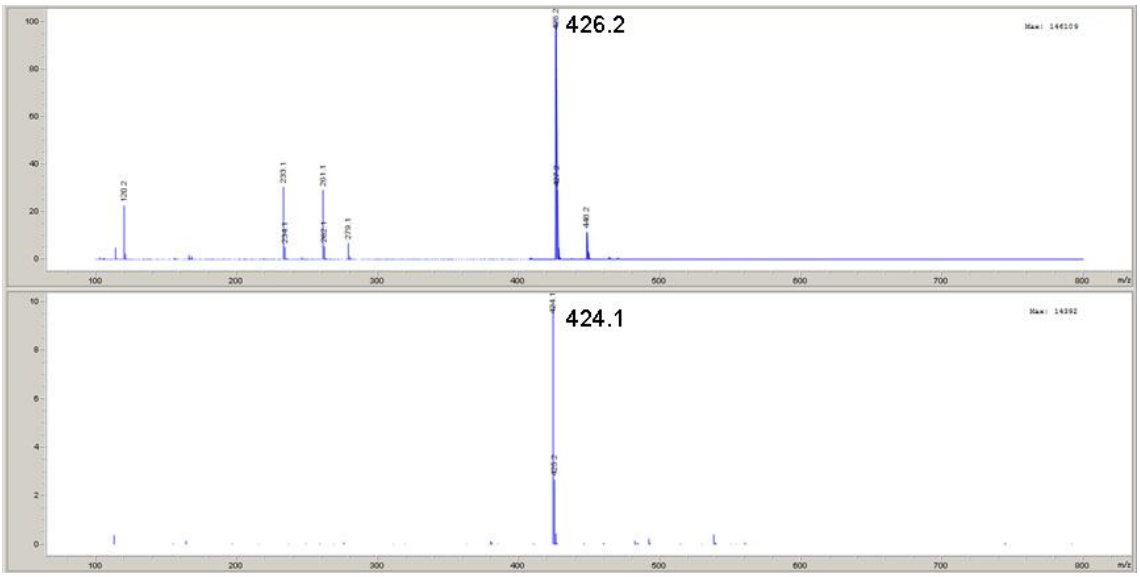

Fig. S34. ESI-MS spectra of Phe-^{D}Ile-Phe in positive (top) and negative (bottom) ion mode.

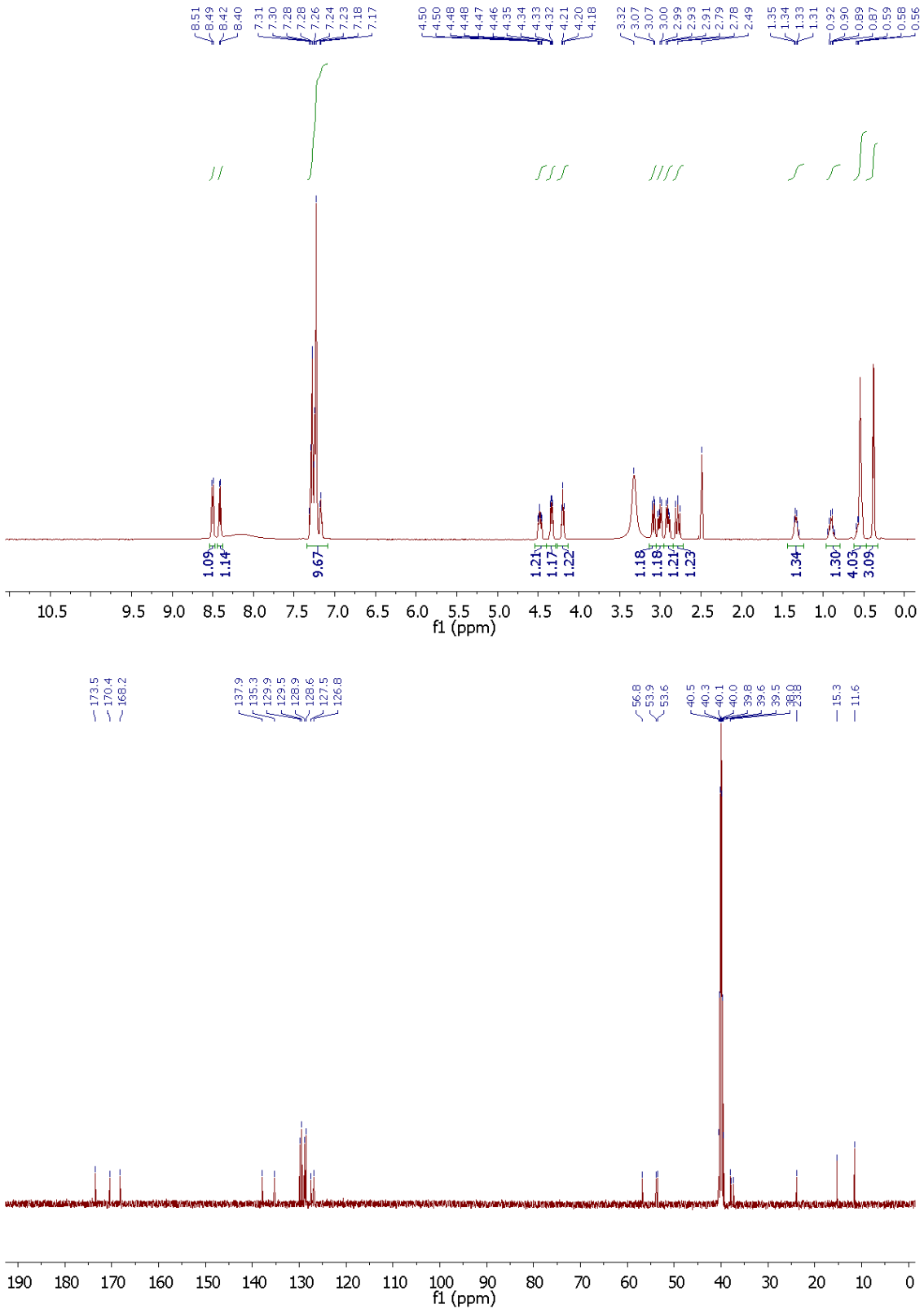

Fig. S35. ^{1}H-NMR (top) and ^{13}C-NMR (bottom) of Phe-^{D}Ile-Phe.

I. Phe-^{D}Nle-Phe

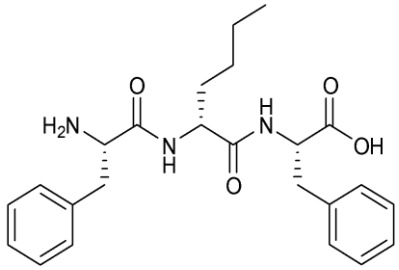

Fig. S36. Chemical structure of Phe-^{D}Nle-Phe.

^{1}H NMR (500 MHz, DMSO-d_6) δ (ppm) 8.48 (d, *J* = 8.5 Hz, 1H, NH), 8.41 (d, *J* = 8.4 Hz, 1H, NH), 7.34 – 7.13 (m, 10H, Ar), 4.46 (ddd, *J* = 10.7, 8.6, 4.3 Hz, 1H, αCH), 4.32 (dd, *J* = 13.5, 7.5 Hz, 1H, αCH), 4.12 (t, *J* = 7.3 Hz, 1H, αCH), 3.09 (dd, *J* = 4.2 Hz, *Jgem* = 13.8 Hz, 1H, βCH$_2$), 3.02 – 2.87 (m, 2H, βCH$_2$), 2.77 (dd, *J* = 10.8 Hz, *Jgem* = 13.7 Hz, 1H, βCH$_2$), 1.18 – 0.89 (m, 4H, 2 x βCH$_2$, 2 x γCH$_2$), 0.74 – 0.55 (m, 5H, δCH$_2$, εCH$_3$).

^{13}C NMR (125 MHz, DMSO-d_6) δ (ppm) 173.4, 171.0, 167.8 (3 x CO); 137.9, 135.3, 129.9, 129.6, 128.8, 128.5, 127.5, 126.8 (Ar); 53.6, 53.5, 52.4 (3 x αC); 37.8, 37.4, 32.9 (3 x βC); 26.8 (γC), 22.2 (δC), 14.1 (εC).

MS (ESI) m/z 426.1 $(M+H)^+$ $C_{24}H_{31}N_3O_4$ requires 425.2.

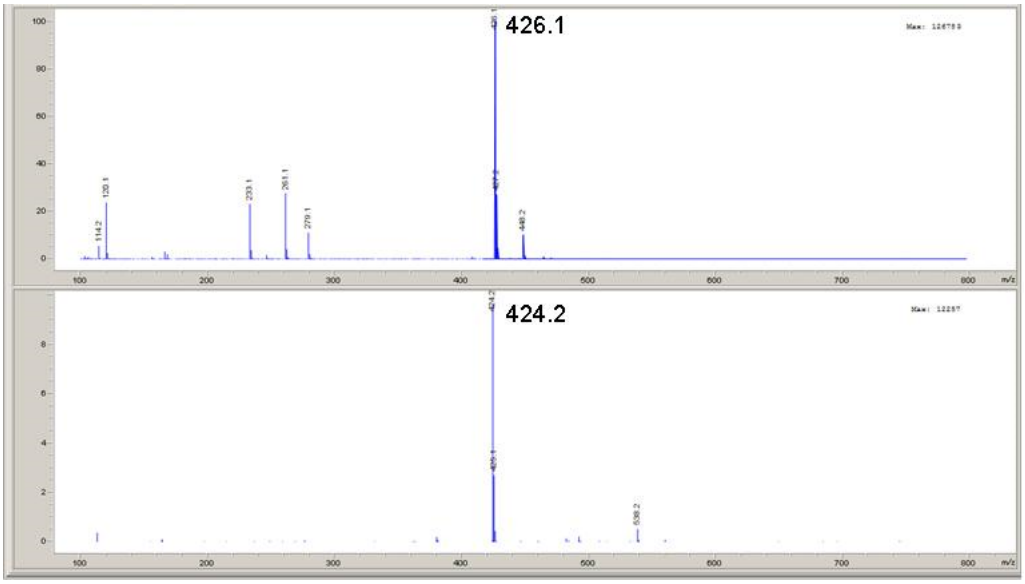

Fig. S37. ESI-MS spectra of Phe-^{D}Nle-Phe in positive (top) and negative (bottom) ion mode.

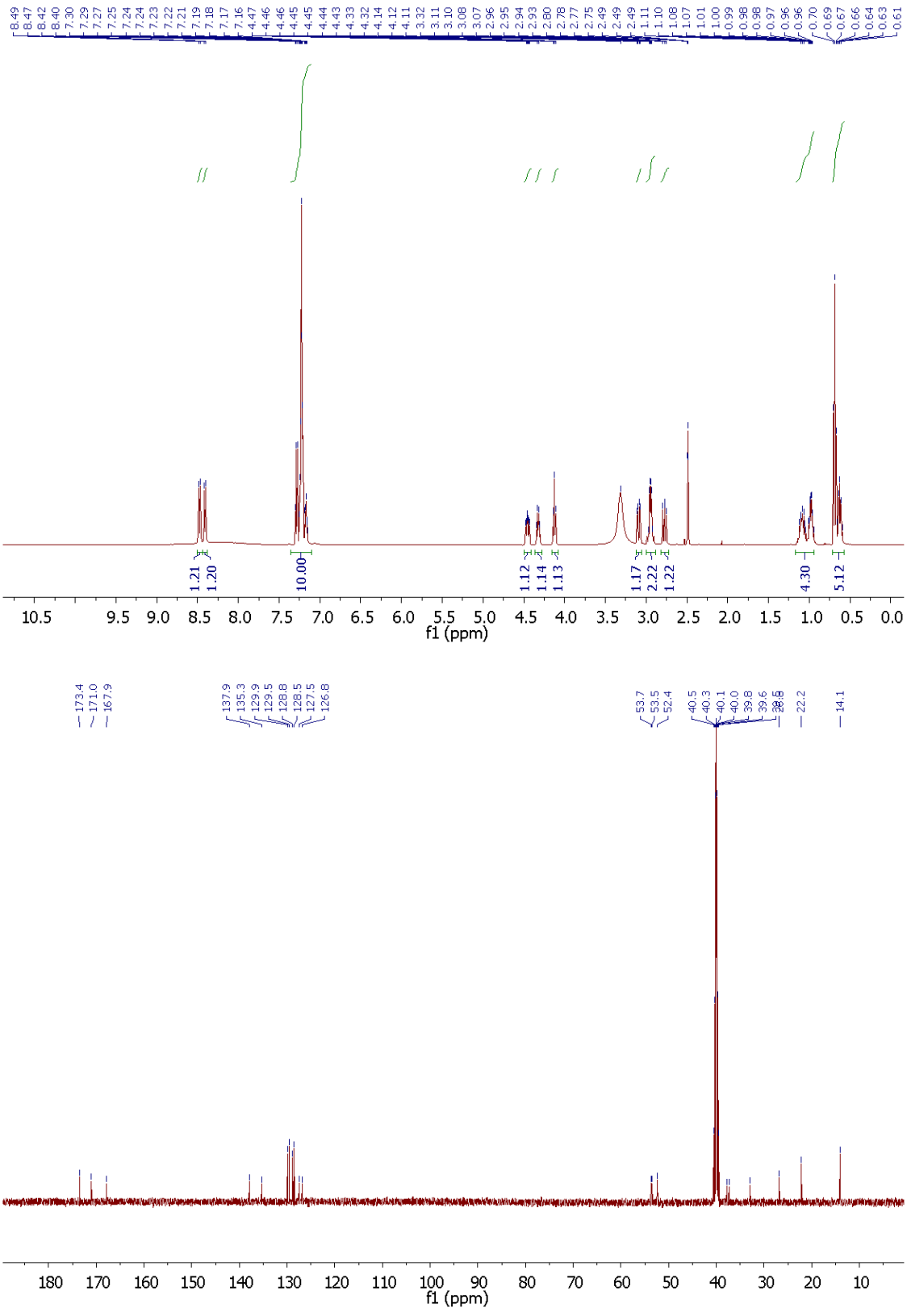

Fig. S38. ^{1}H-NMR (top) and ^{13}C-NMR (bottom) of Phe-^{D}Nle-Phe.

3. Peptides HPLC trace

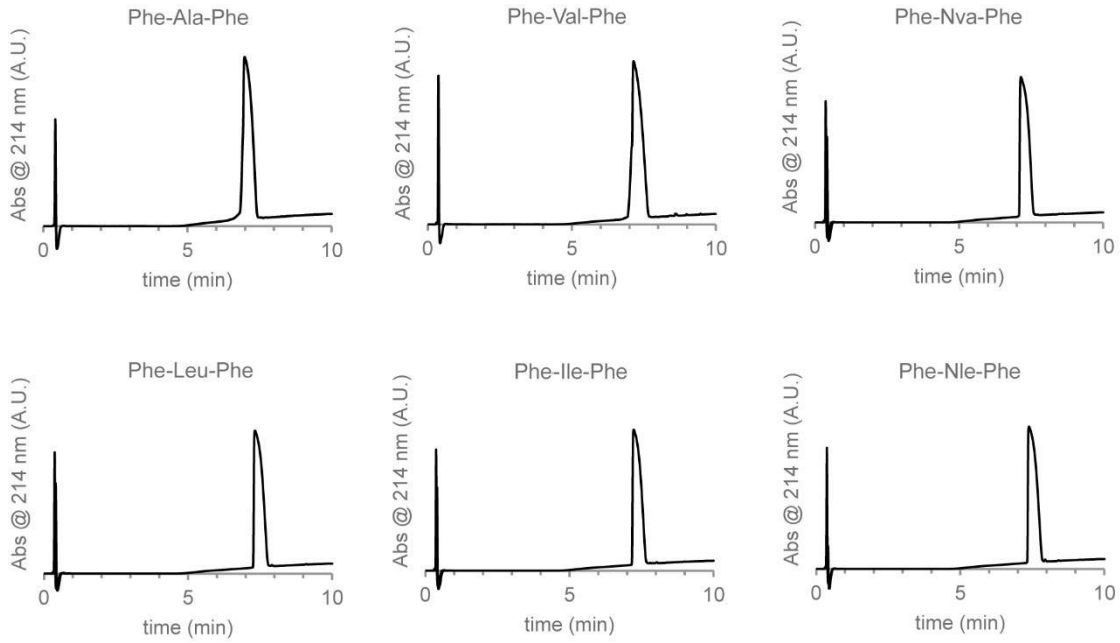

Fig. S39. Analytical HPLC trace for homochiral tripeptides. Column: Zorbax SB-C18 Rapid Resolution HT 2.1x50 mm, particle size: 1.8 microns. Flow 0.5 ml/min. Method: t= 0, 95% water (+0.1% formic acid) and 5% MeCN (+0.1% formic acid); t = 10 min, 5% water (+0.1% formic acid) and 95 % MeCN (+0.1 % formic acid).

Table S2. Homochiral peptides HPLC retention time.

SEQUENCE	RETENTION TIME (min)
Phe-Ala-Phe	7.0
Phe-Val-Phe	7.1
Phe-Nva-Phe	7.1
Phe-Leu-Phe	7.3
Phe-Ile-Phe	7.3
Phe-Nle-Phe	7.4

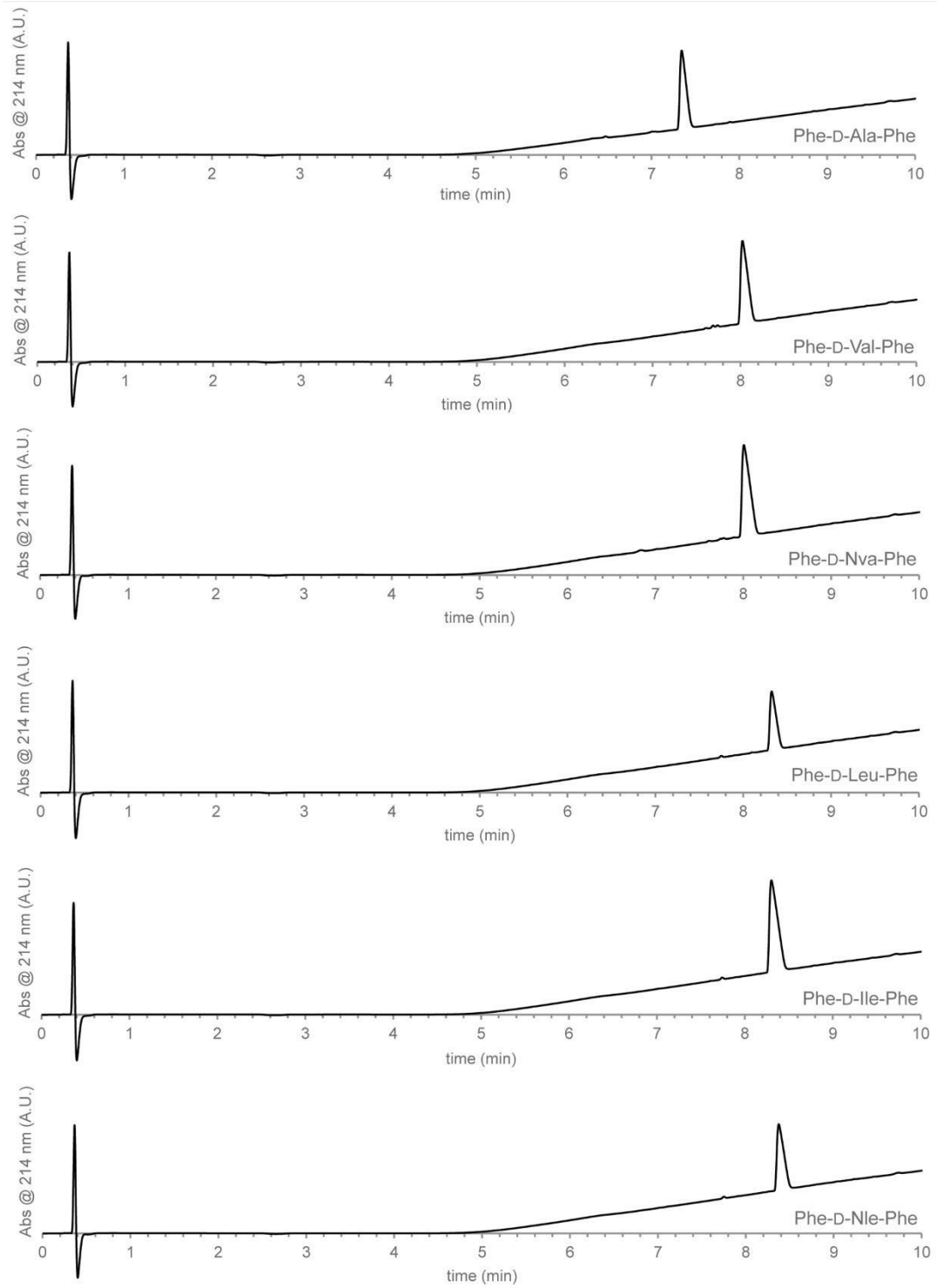

Fig. S40. Analytical HPLC trace for heterochiral tripeptides. Column: Zorbax SB-C18 Rapid Resolution HT 2.1x50 mm, particle size: 1.8 microns. Flow 0.5 ml/min. Method: t= 0, 95% water (+0.1% formic acid) and 5% MeCN (+0.1% formic acid); t = 10 min, 5% water (+0.1% formic acid) and 95 % MeCN (+0.1 % formic acid).

4. *In silico* data for tripeptides

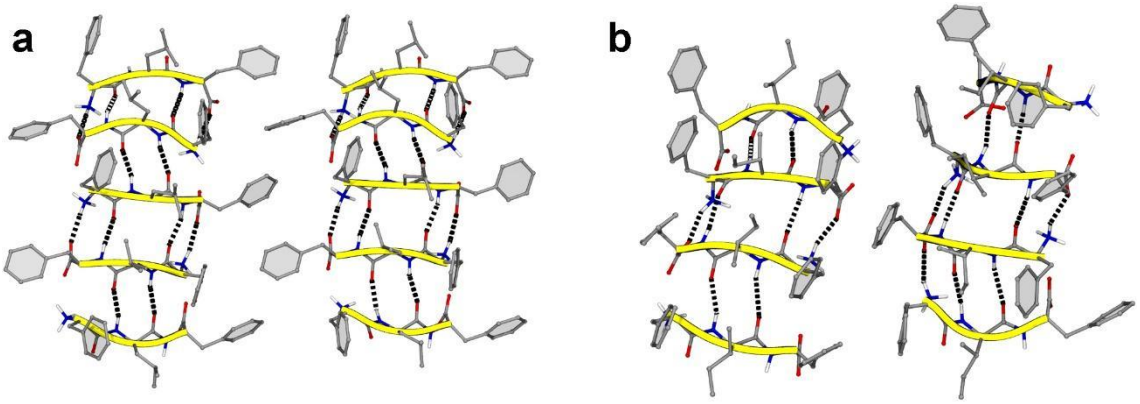

Fig. S41. Phe-^{D}Leu-Phe (a) and Phe-^{D}Ile-Phe (b) tripeptide stacks with backbones depicted in yellow and hydrogen bonds depicted with dashed bold lines. Oxygen atoms are shown in red and nitrogen atoms in blue. Images were generated with the VMD 1.9.3 software. Hydrogen bonds were identified using cutoffs of 3.5 Å and 35° for the donor-acceptor distance and donor-hydrogen-acceptor angle, respectively.

5. CD spectra of tripeptides in solution

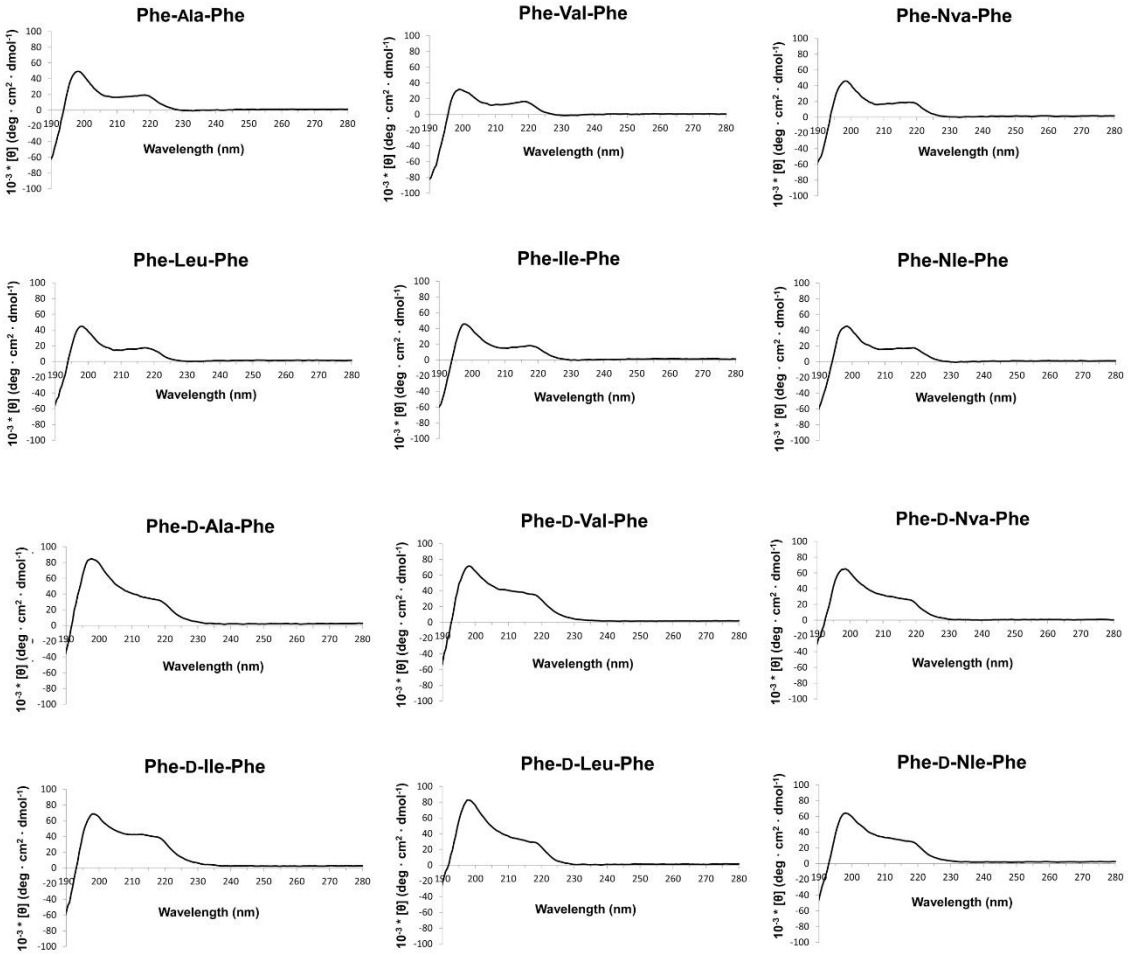

Fig. S42. CD spectra of tripeptides in solution (alkaline pH).

6. Tripeptide conformations in solution

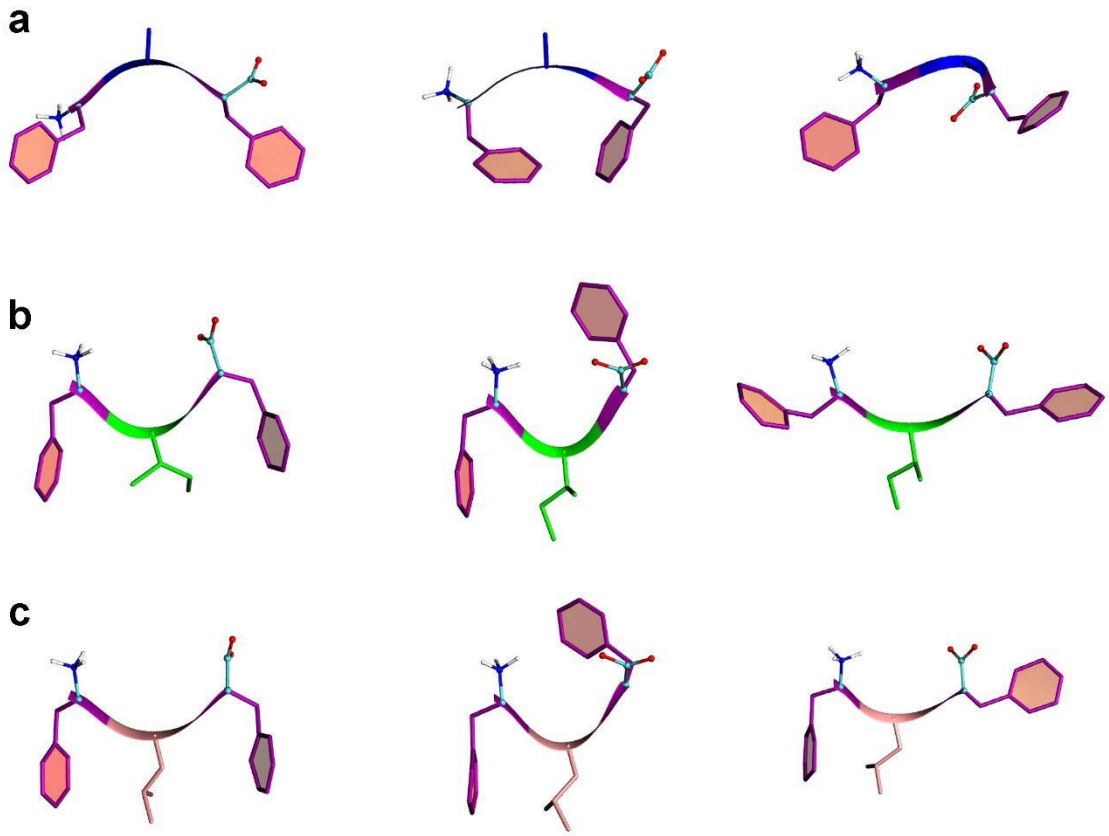

Fig. S43. Tripeptide main conformations adopted in solution by Phe-Ala-Phe (a), Phe-^{D}Ile-Phe (b) and Phe-^{D}Leu-Phe (c).

Table S3. χ_1, χ_2 angles and $C_{\alpha 1}$-$C_{\alpha 3}$ distances (Å) for the most representative tripeptide conformations.

Sequence	χ_1	χ_2	χ_2	χ_3	**$C_{\alpha 1}$-$C_{\alpha 3}$ (Å)**
Phe-Ala-Phe	156°	-81°	145°	-119°	6.7
Phe-^{D}Leu-Phe	132°	70°	-147°	-100°	6.7
Phe-^{D}Ile-Phe	147°	59°	-149°	-81°	6.4

7. CD spectra and photographs of non-gelling tripeptides at neutral pH.

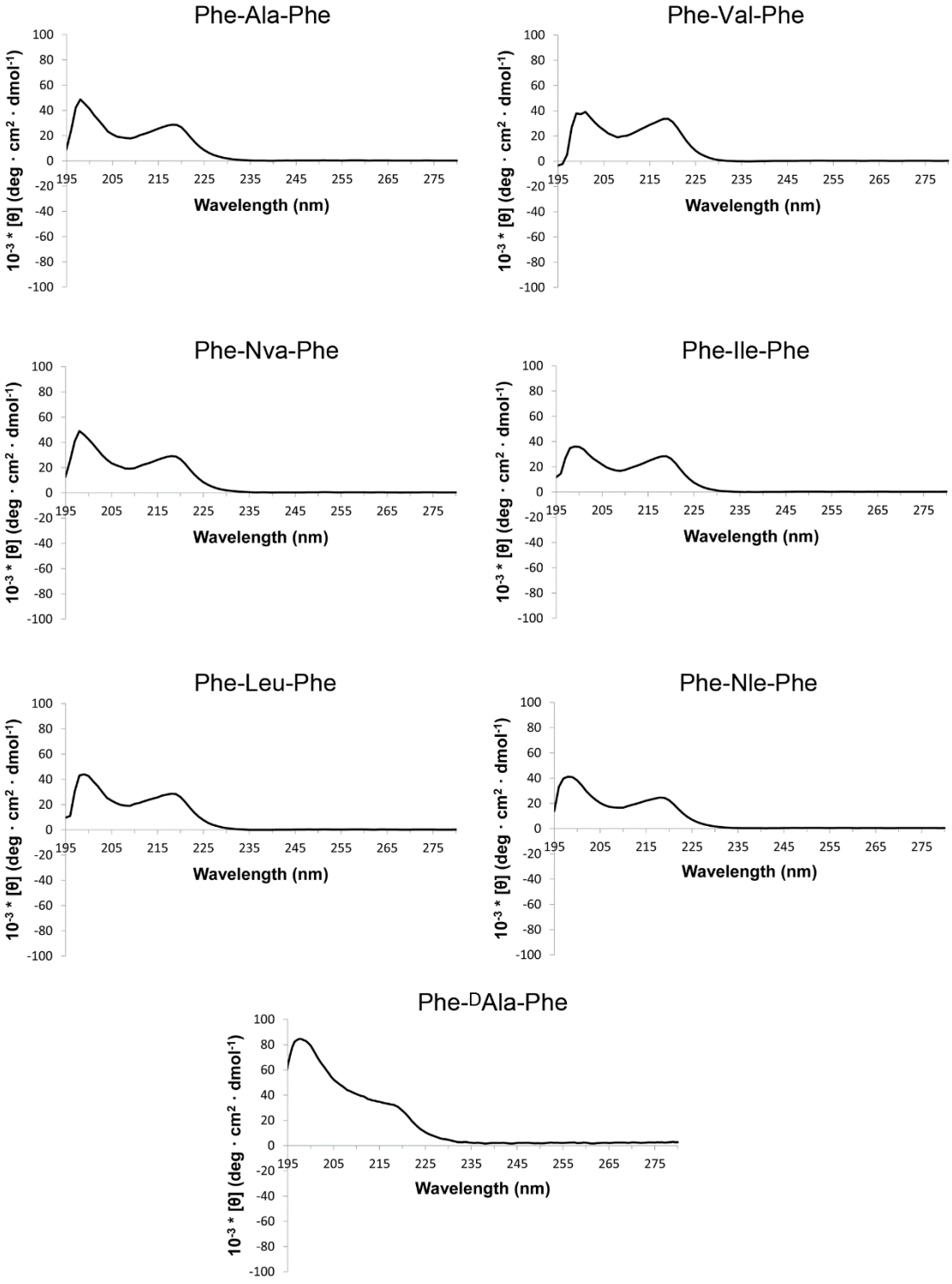

Fig. S44. CD spectra of non-assembling tripeptides at 10 mM and pH 7.4. *Note:* molar ellipticity did not change significantly for peptide concentrations in the range 1-10 mM, while changes were noted for self-assembling peptides.

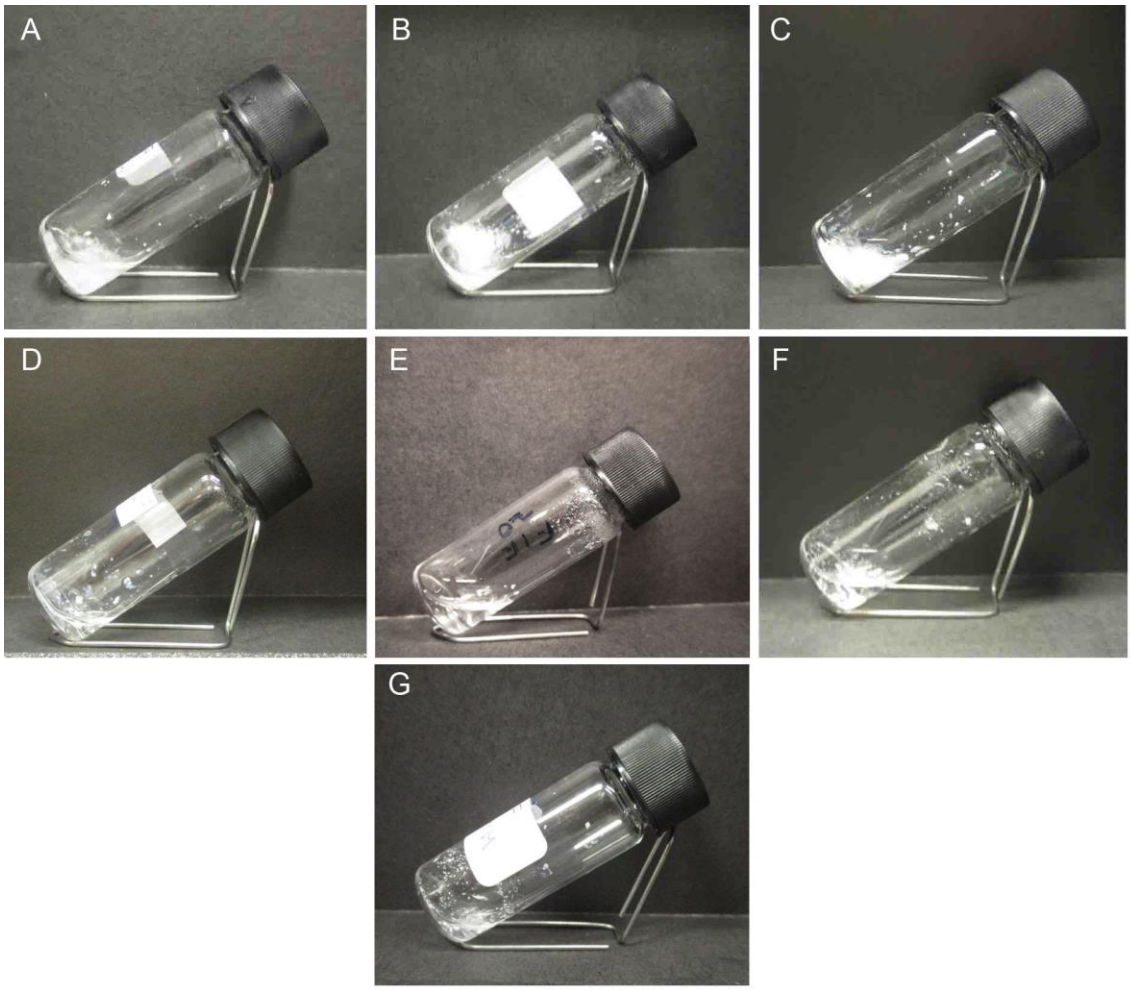

Fig. S45. Increasing the concentration of non-gelling tripeptides above their solubility limit led to phase separation but not to hydrogel formation. A, Phe-Ala-Phe; B, Phe-Val-Phe; C, Phe-Nva-Phe; D, Phe-Leu-Phe; E, Phe-Ile-Phe; F, Phe-Nle-Phe; G, Phe-^{D}Ala-Phe.

8. CD spectra of tripeptide self-assembly kinetics.

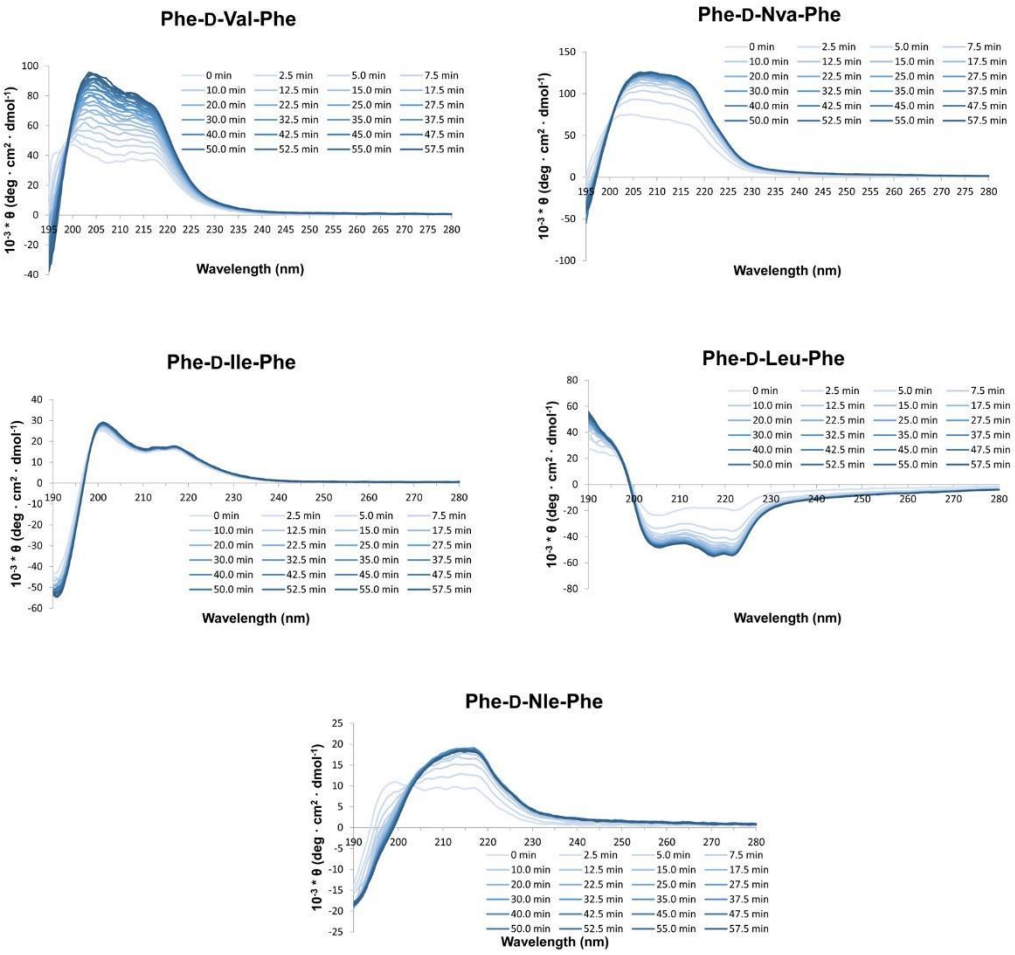

Fig. S46. CD spectra of tripeptide self-assembly kinetics.

9. Thermoreversibility tests.

SEQUENCE	MELTING TEMPERATURE RANGE(ºC)
Phe-^{D}Val-Phe	43 – 59
Phe-^{D}Nva-Phe	39 – 60
Phe-^{D}Ile-Phe	50 – 72
Phe-^{D}Leu-Phe	55 – 81
Phe-^{D}Nle-Phe	51 – 73

Table S4. Gel-to-sol transition temperature range for each tripeptide hydrogel as observed in glass vials. The first value refers to the first solution drop appearing in the sample, and the last value refers to the sample being completely soluble. All hydrogels are thermoreversible (see photographs of Figure 3a in main MS).

10. Comparison of MD data for Phe-^{D}Leu-Phe and Phe-^{D}Ile-Phe sheets.

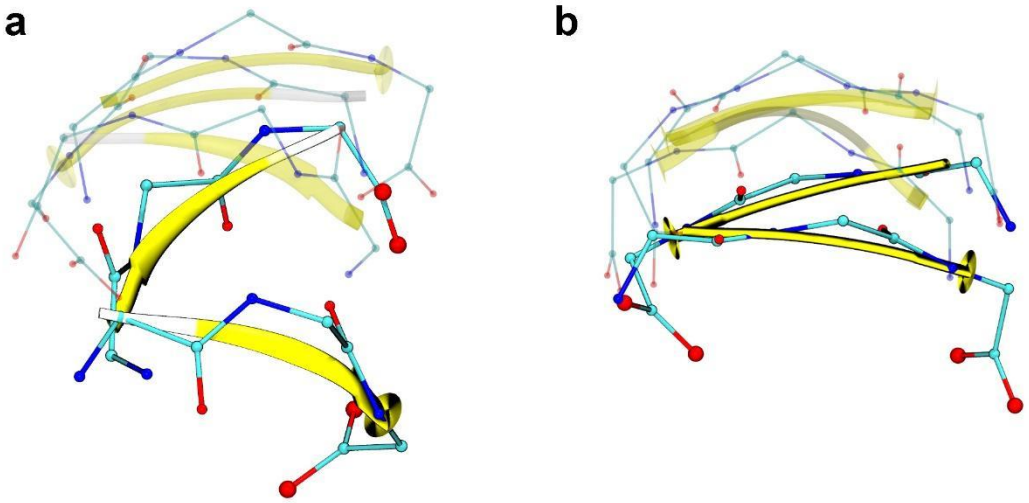

Fig. S47. Comparison of MD data for peptide stacks formed by Phe-^{D}Leu-Phe (a) and Phe-^{D}Ile-Phe (b) revealed that the latter were more planar. ®-strands are highlighted in yellow.

11. ATR-IR spectra for tripeptides.

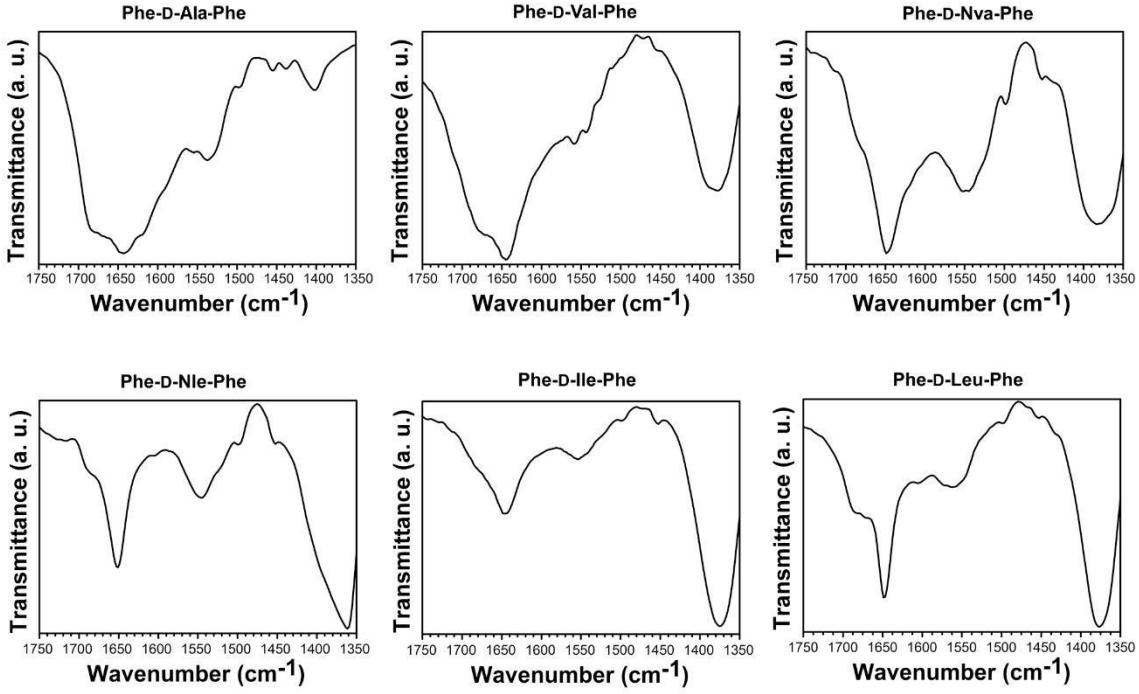

Fig. S48. ATR-IR spectra of Phe-^{D}Ala-Phe (that does not gel) and tripeptide gels.

12. AFM images of non-gelling L-peptides.

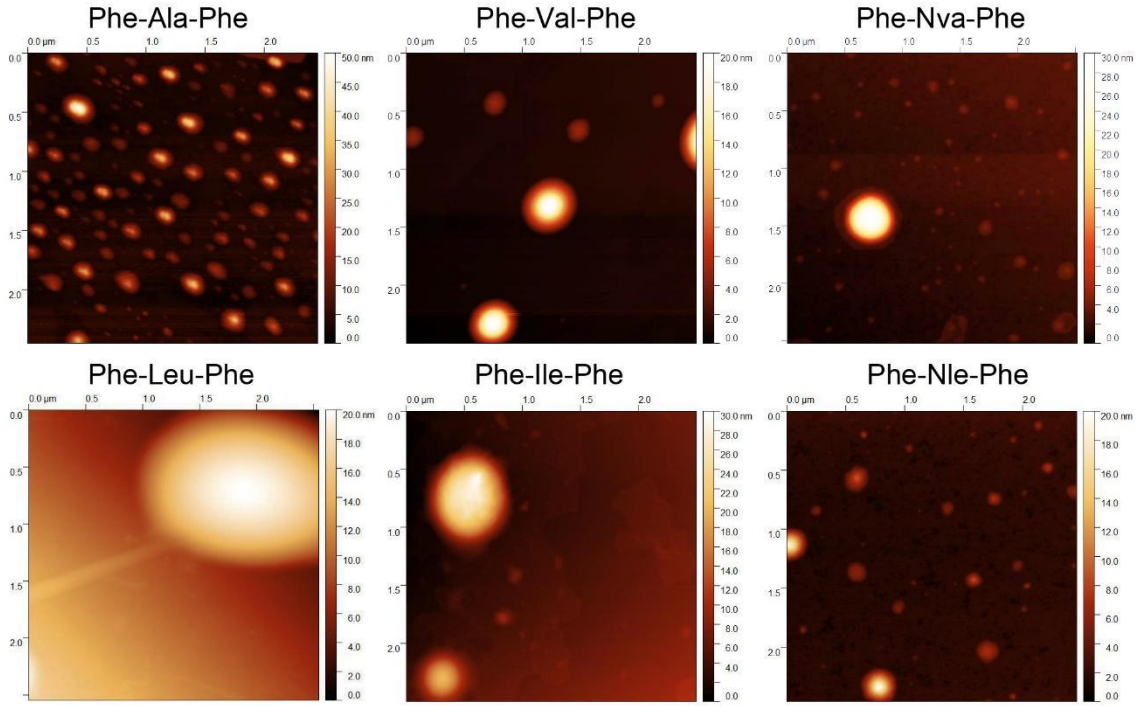

Fig. S49. AFM images of non-gelling L-peptides revealed mainly amorphous aggregates. Phe-Ala-Phe samples displayed also microcrystals (of size too large to be probed by AFM).

13. Stained TEM images of non-gelling L-peptides.

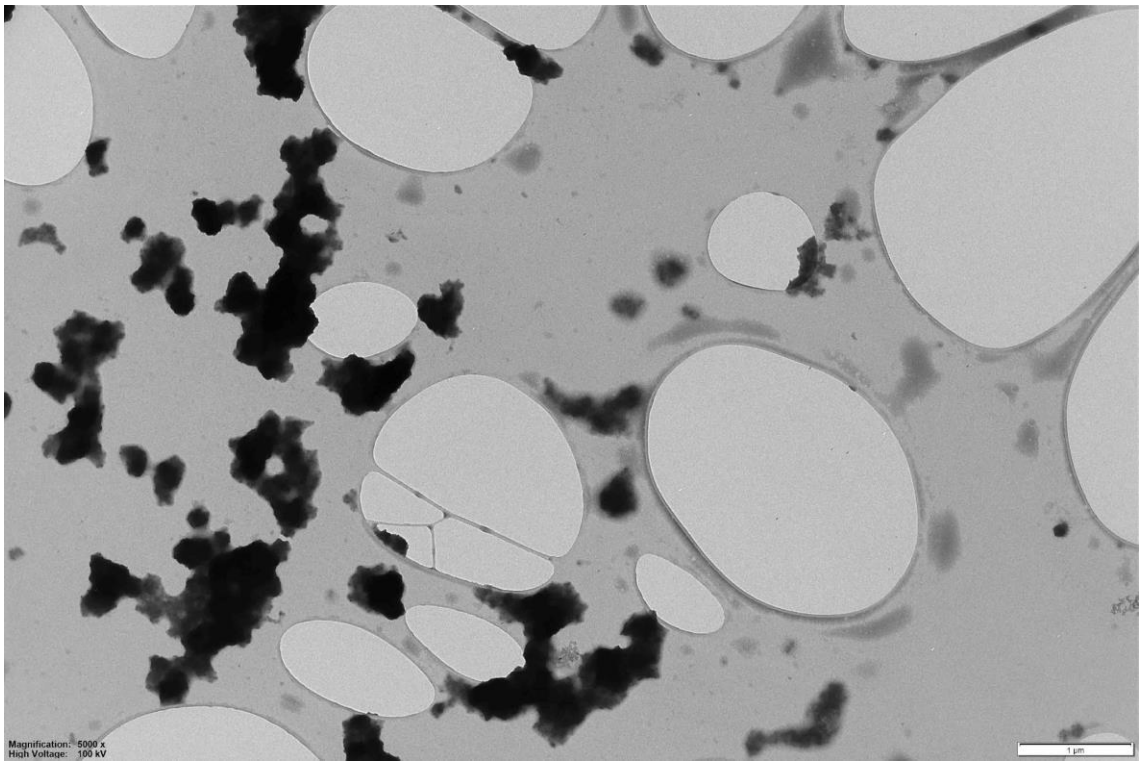

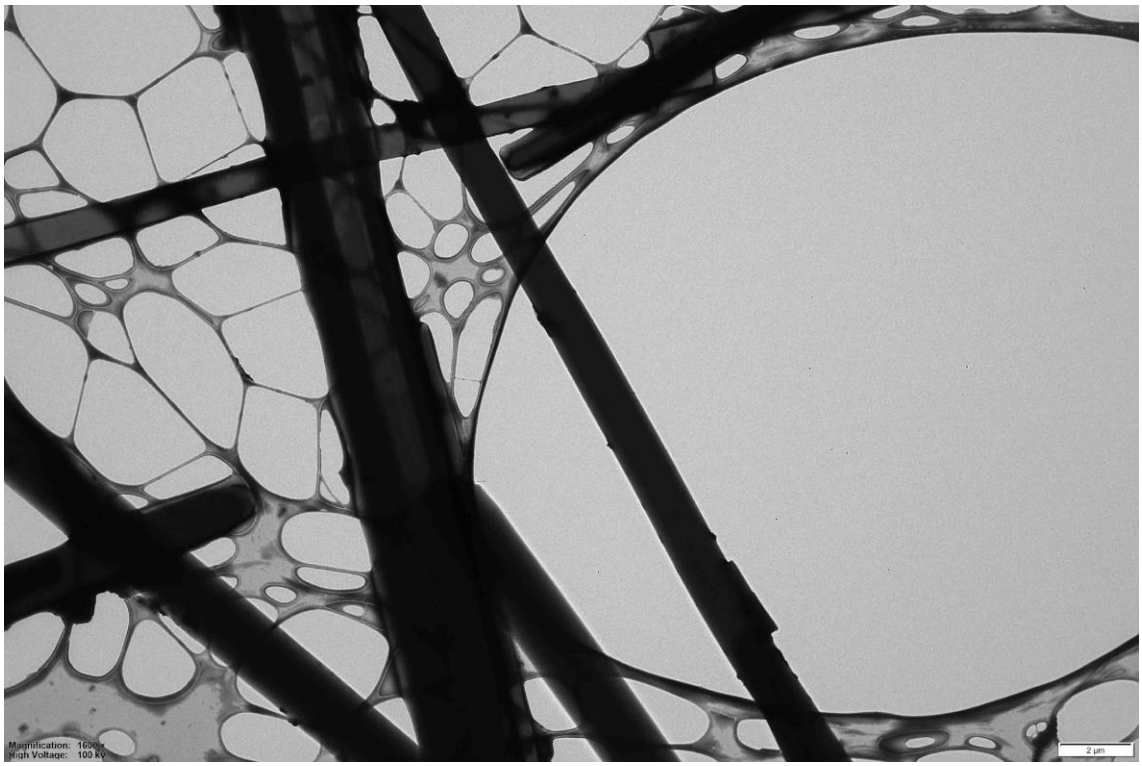

Fig. S50. TEM images of Phe-Ala-Phe showing amorphous aggregates (top) and microcrystals (bottom).

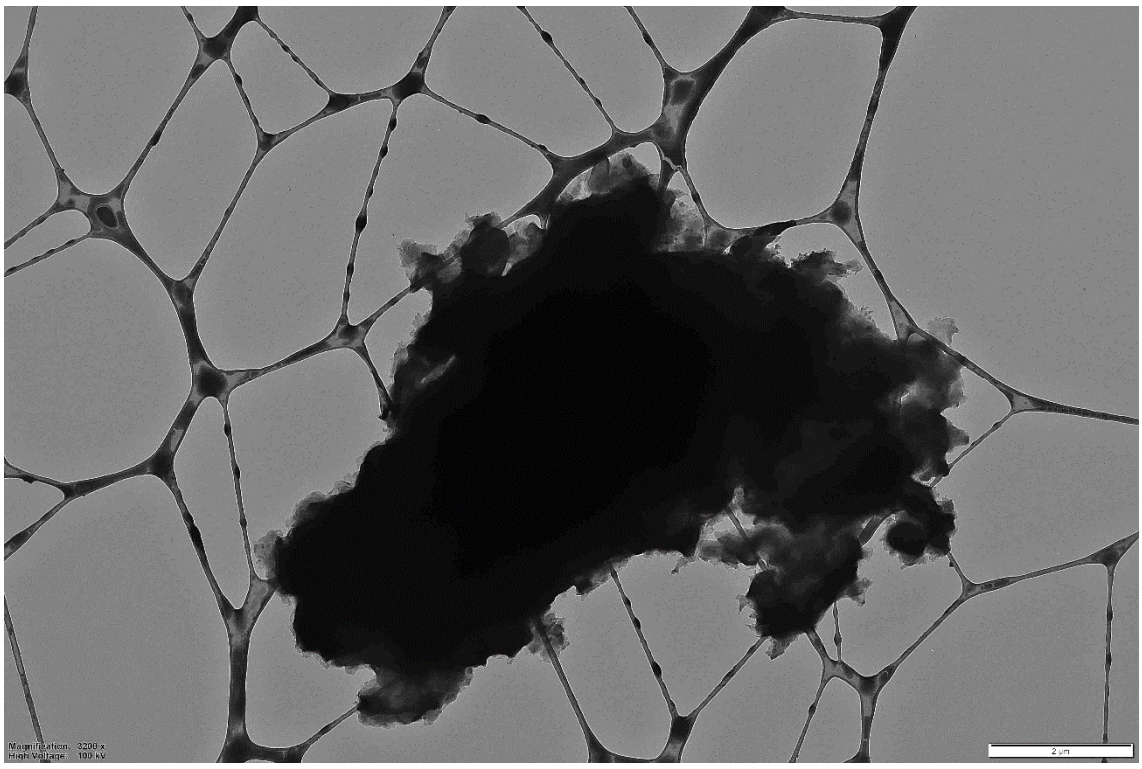

Fig. S51. TEM images of Phe-Val-Phe showing amorphous aggregates.

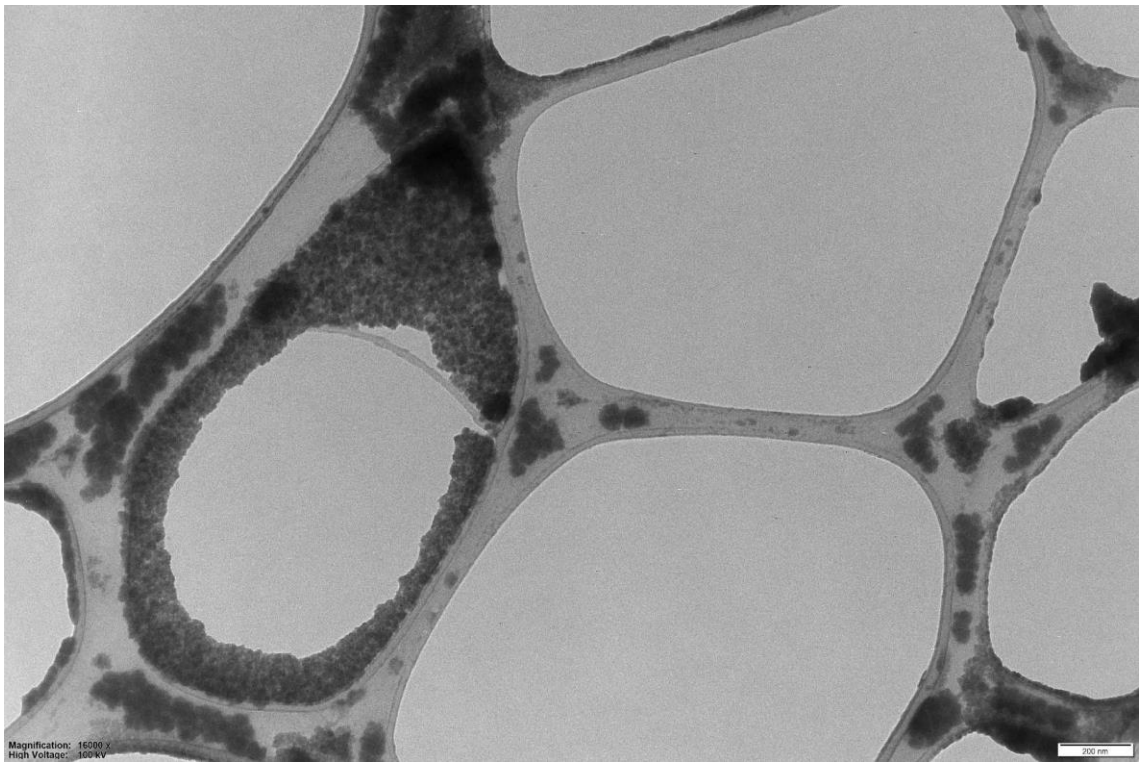

Fig. S52. TEM images of Phe-Nva-Phe showing amorphous aggregates.

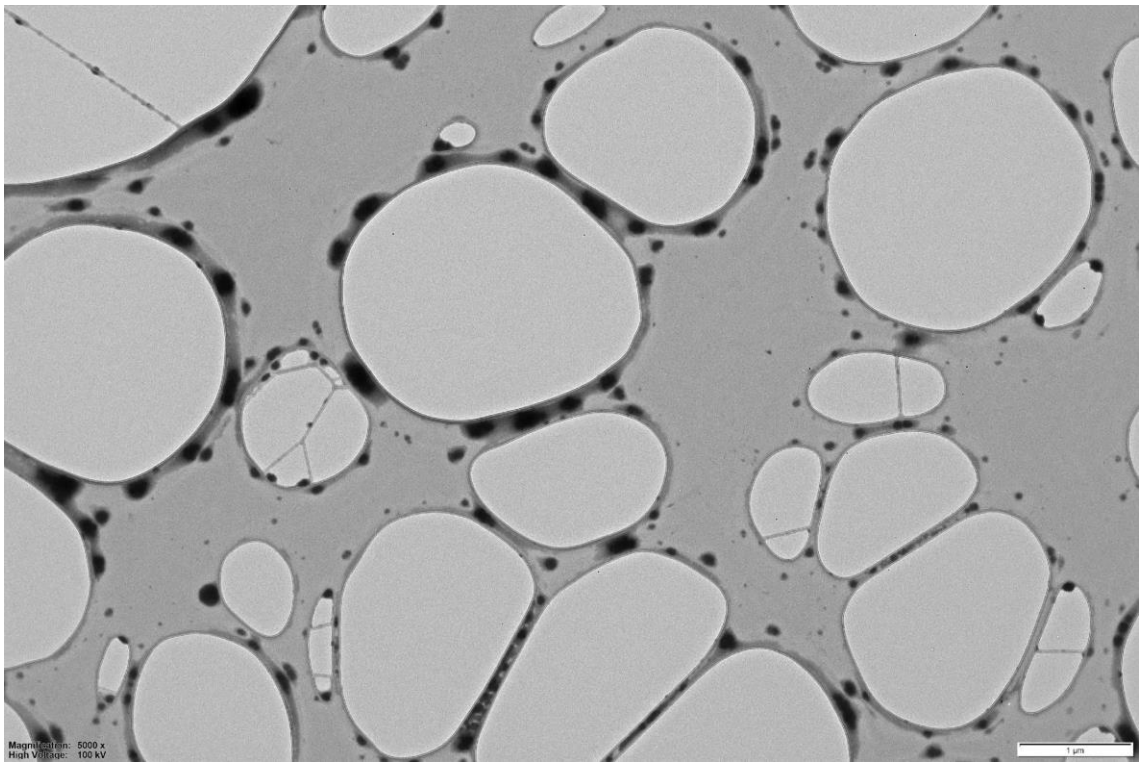

Fig. S53. TEM images of Phe-Leu-Phe showing amorphous aggregates.

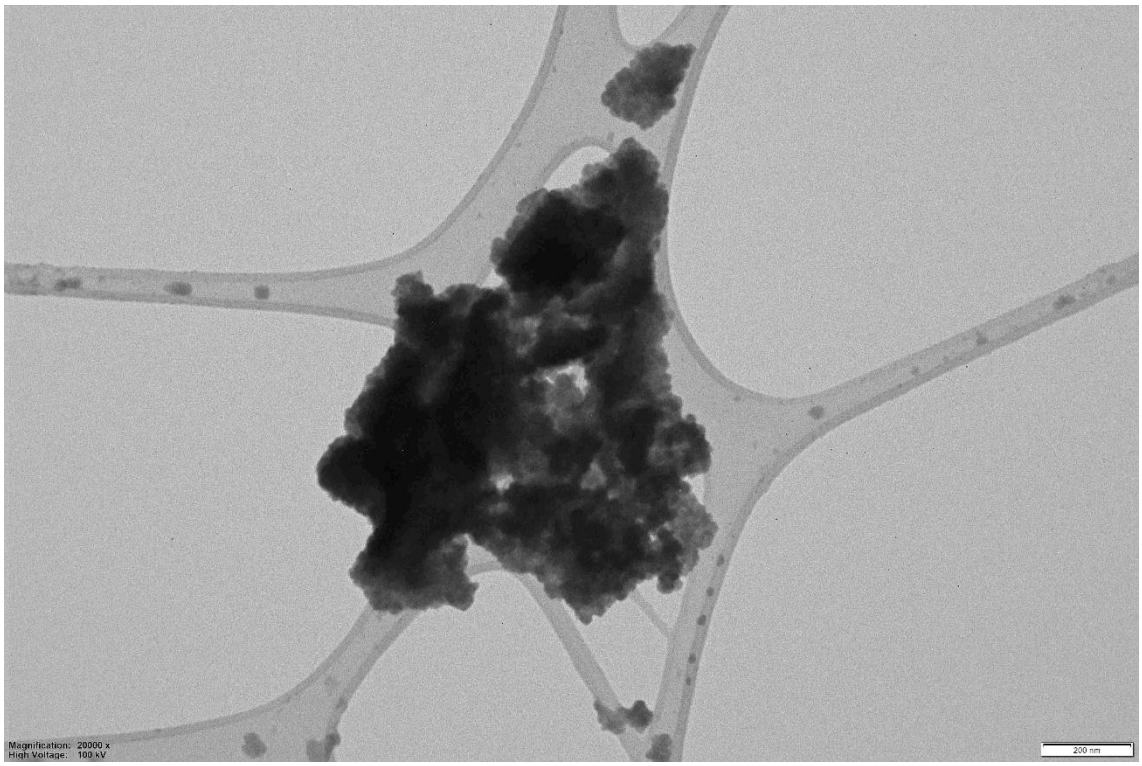

Fig. S54. TEM images of Phe-Ile-Phe showing amorphous aggregates.

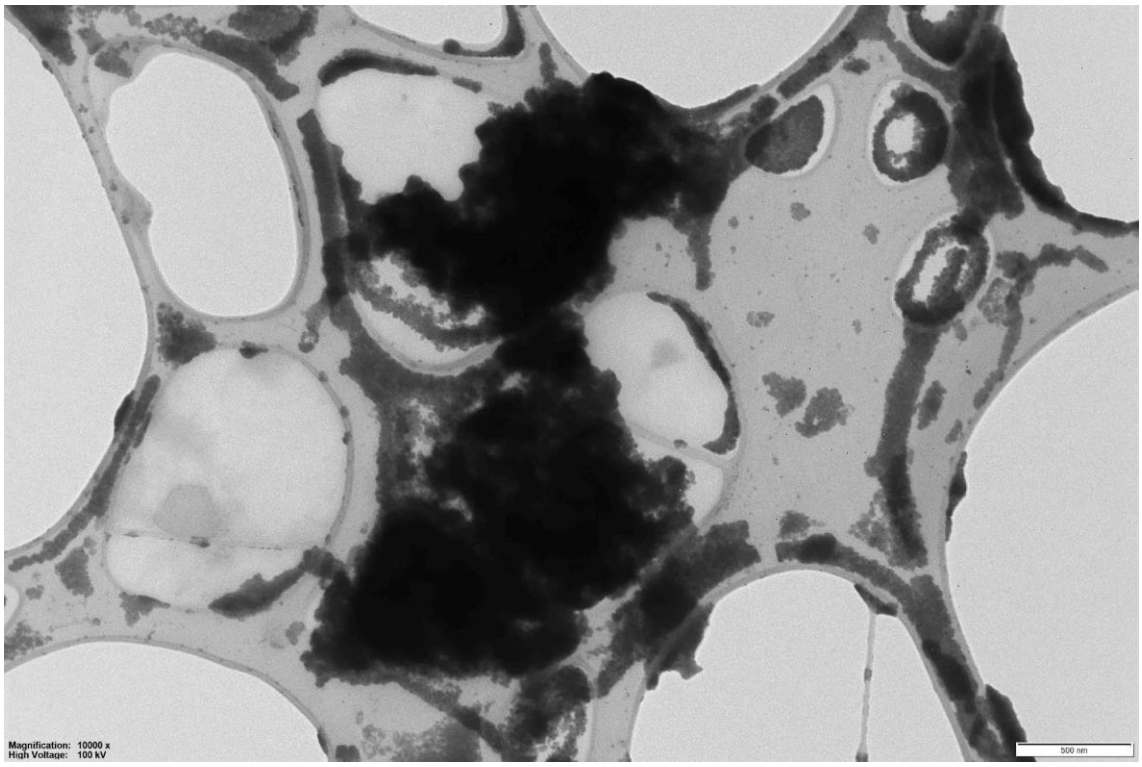

Fig. S55. TEM images of Phe-Nle-Phe showing amorphous aggregates.

14. Cryo-TEM and stained TEM images for non-gelling Phe-^{D}Ala-Phe.

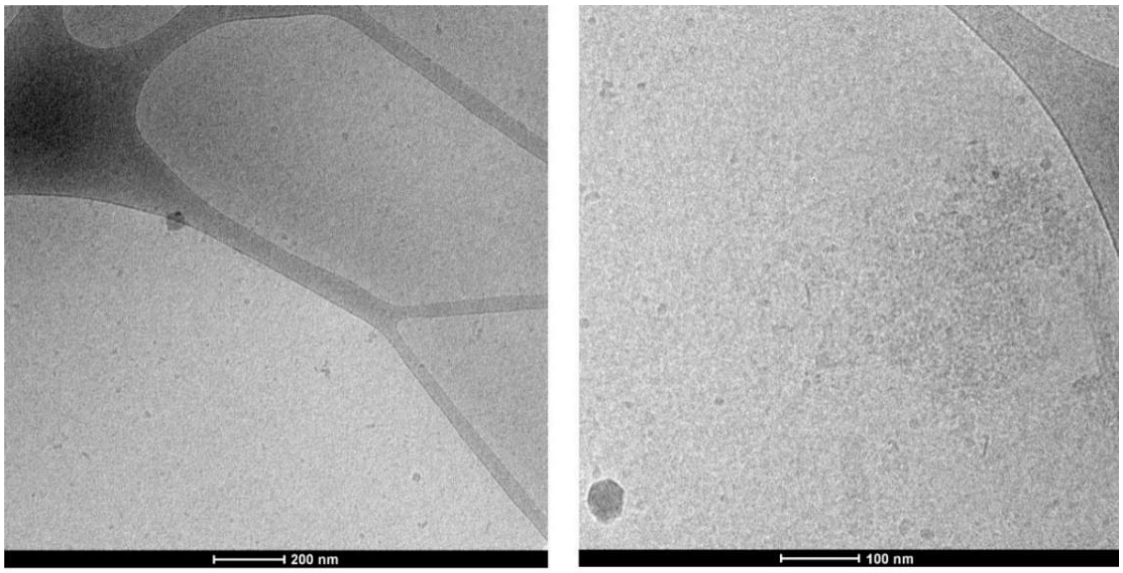

Fig. S56. Cryo-TEM images of Phe-^{D}Ala-Phe. The majority of images were featureless.

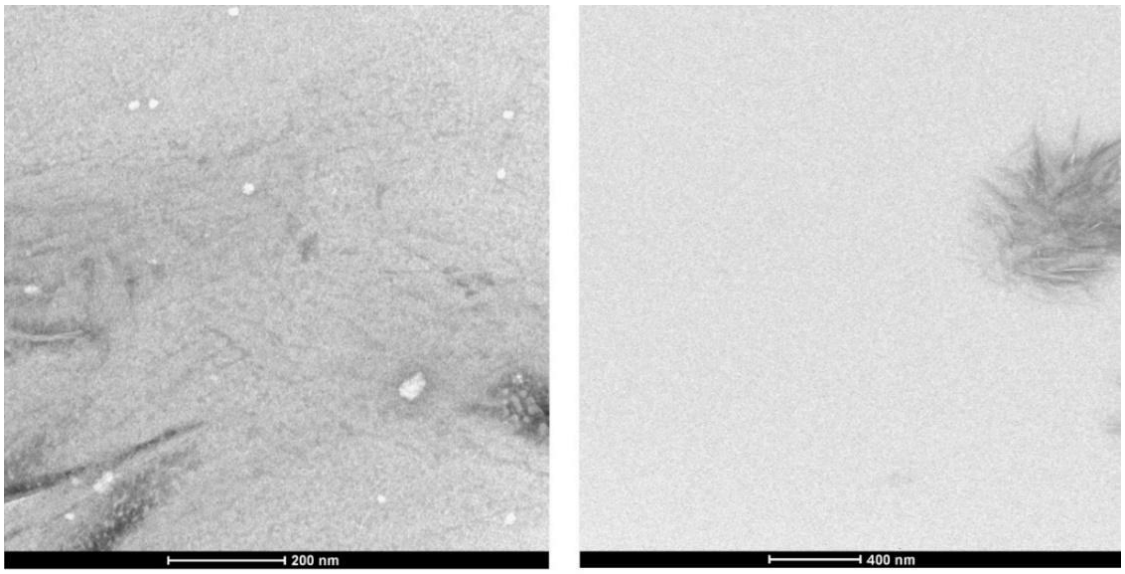

Fig. S57. Stained TEM images of Phe-^{D}Ala-Phe. The majority of images were featureless.

15. Cryo-TEM and stained TEM images of self-assembled peptides.

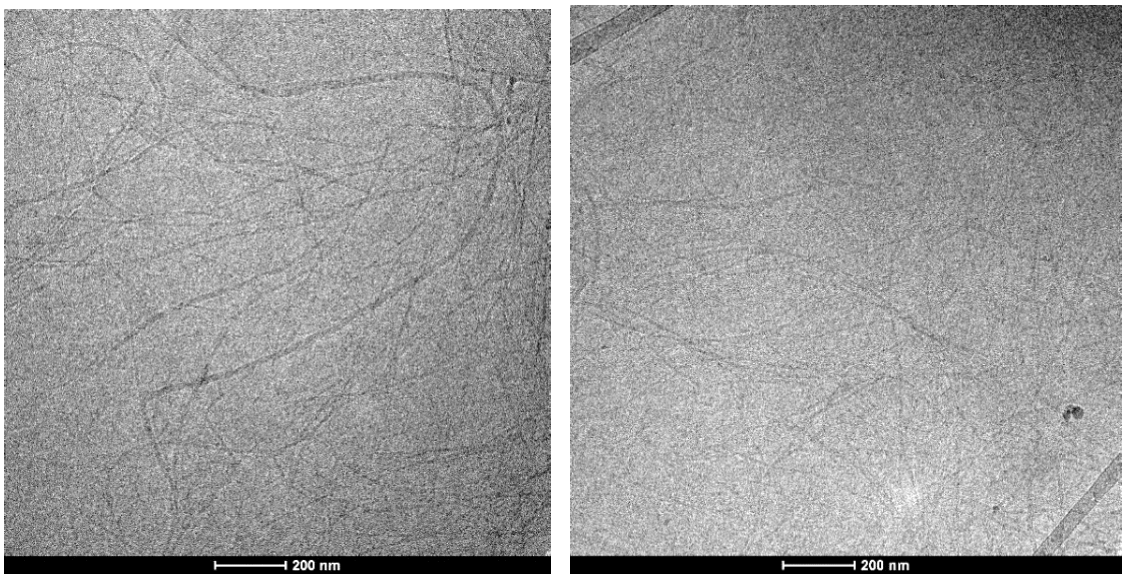

Fig. S58. Cryo-TEM images of Phe-^{D}Val-Phe.

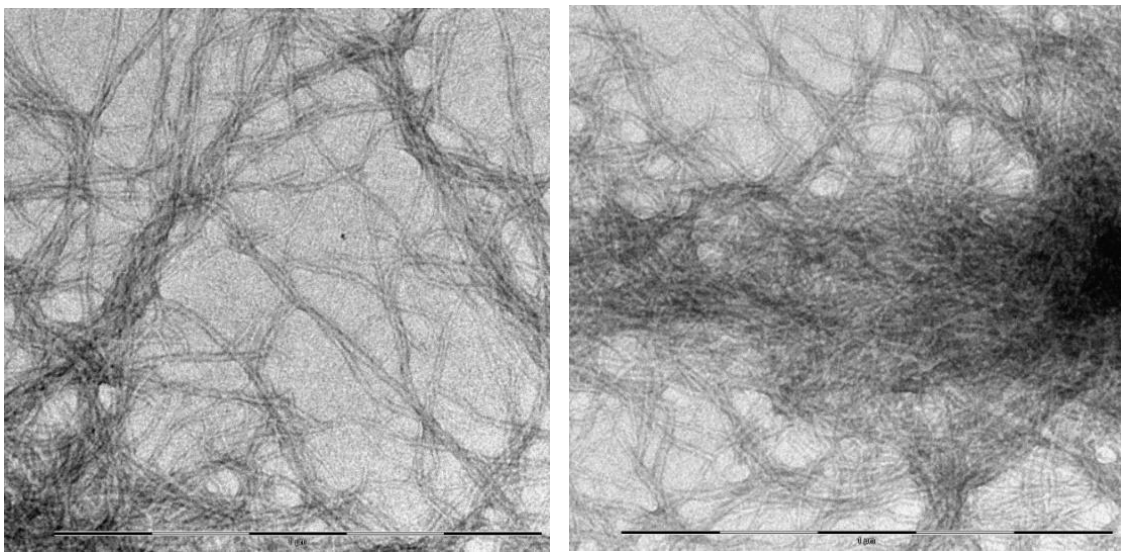

Fig. S59. TEM images of Phe-^{D}Val-Phe.

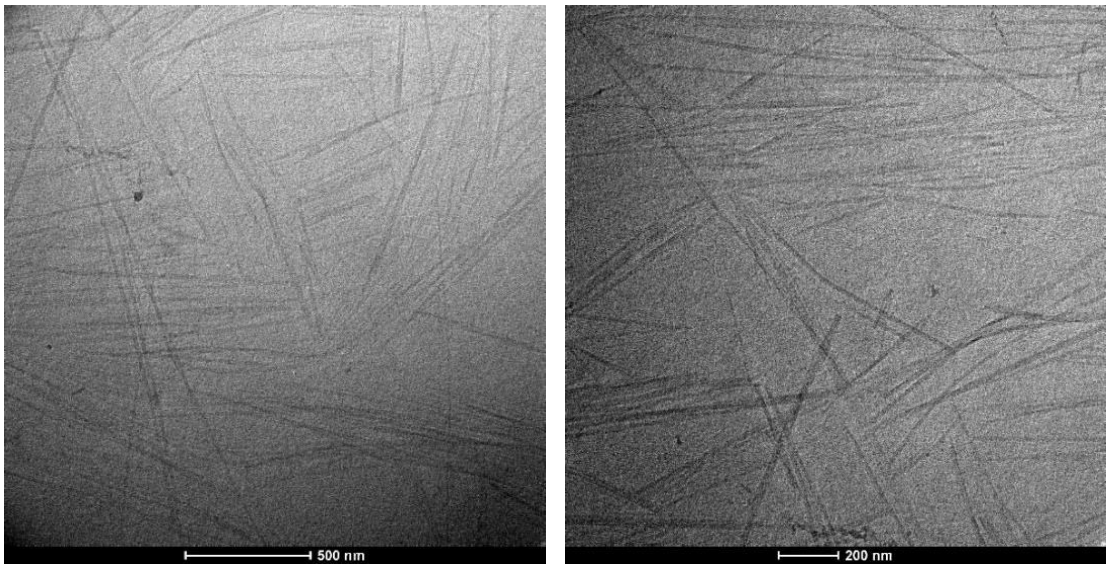

Fig. S60. Cryo-TEM images of Phe-^{D}Nva-Phe.

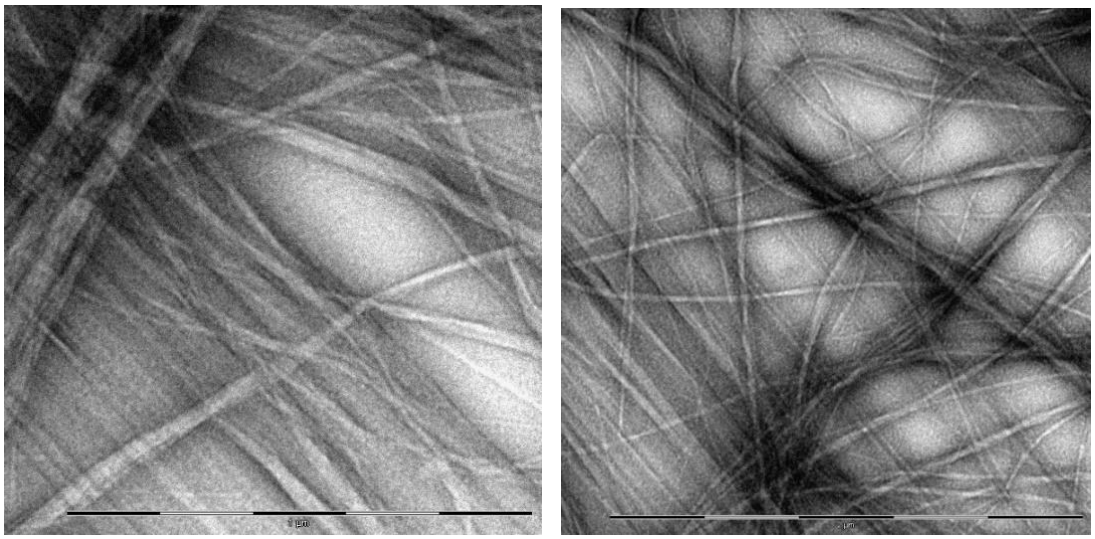

Fig. S61. TEM images of Phe-^{D}Nva-Phe.

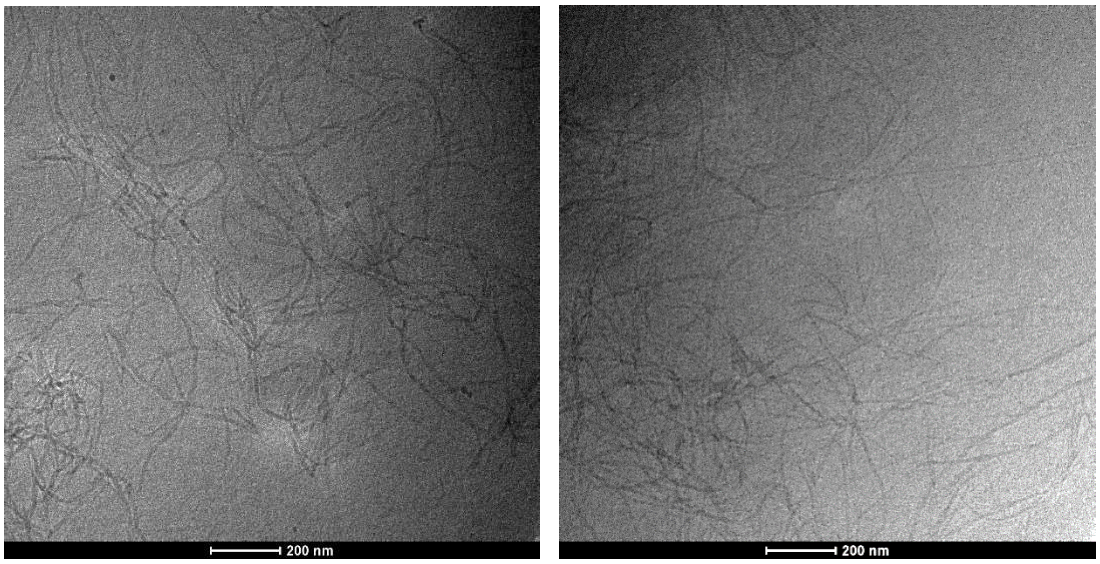

Fig. S62. Cryo-TEM images of Phe-^{D}Ile-Phe.

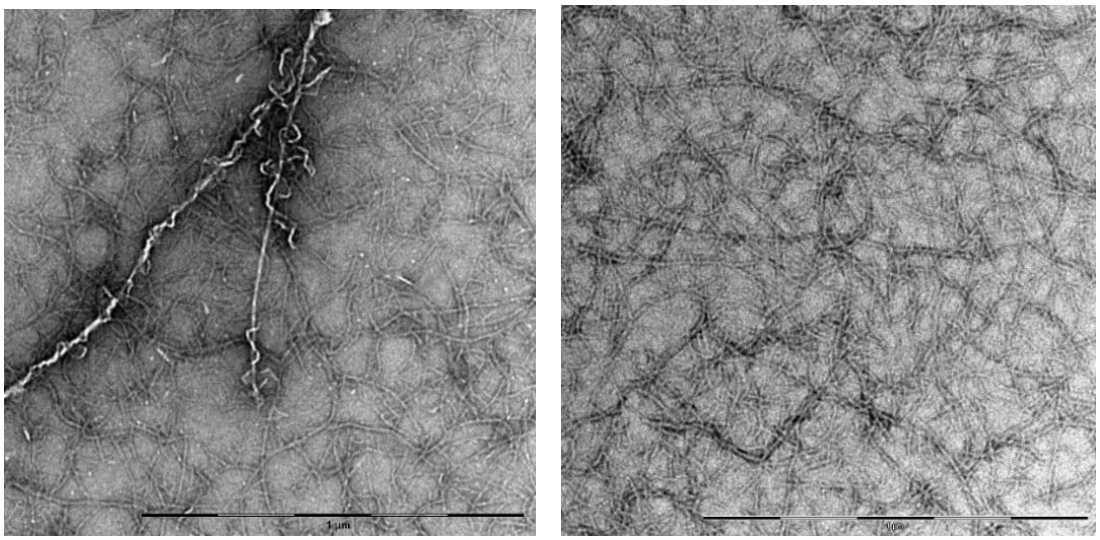

Fig. S63. TEM images of Phe-^{D}Ile-Phe.

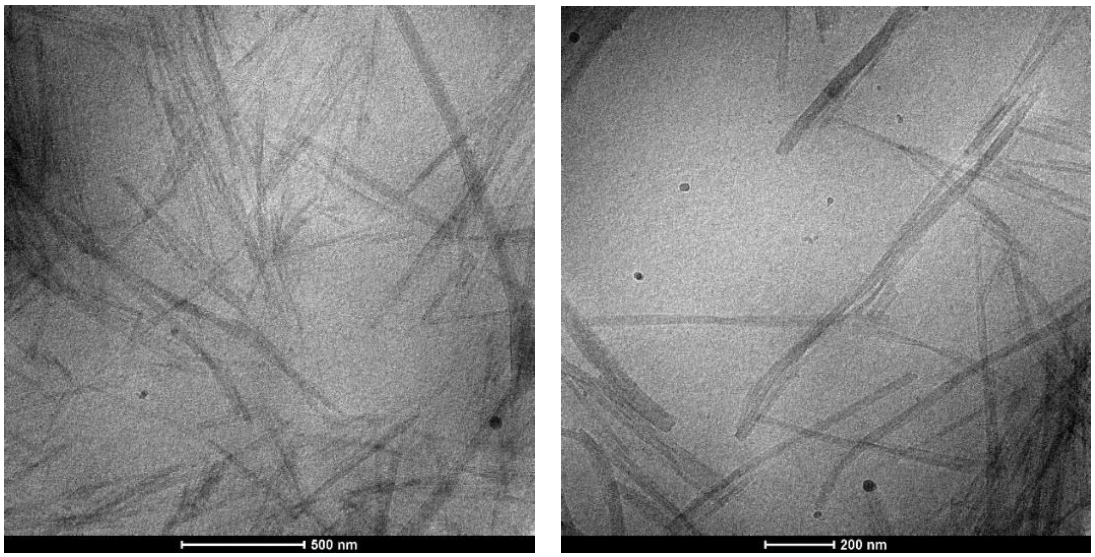

Fig. S64. Cryo-TEM images of Phe-^{D}Leu-Phe.

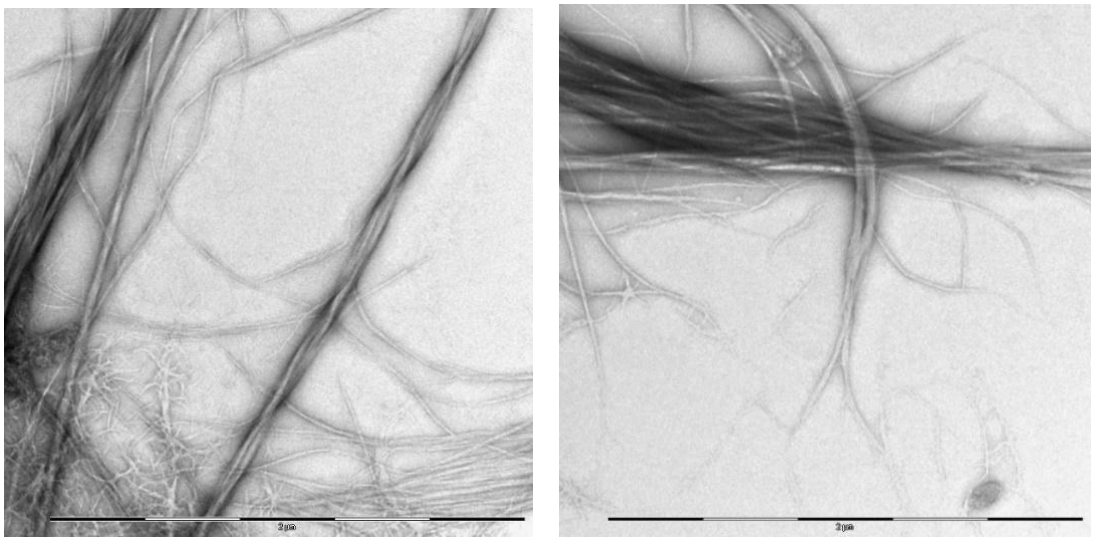

Fig. S65. TEM images of Phe-^{D}Leu-Phe.

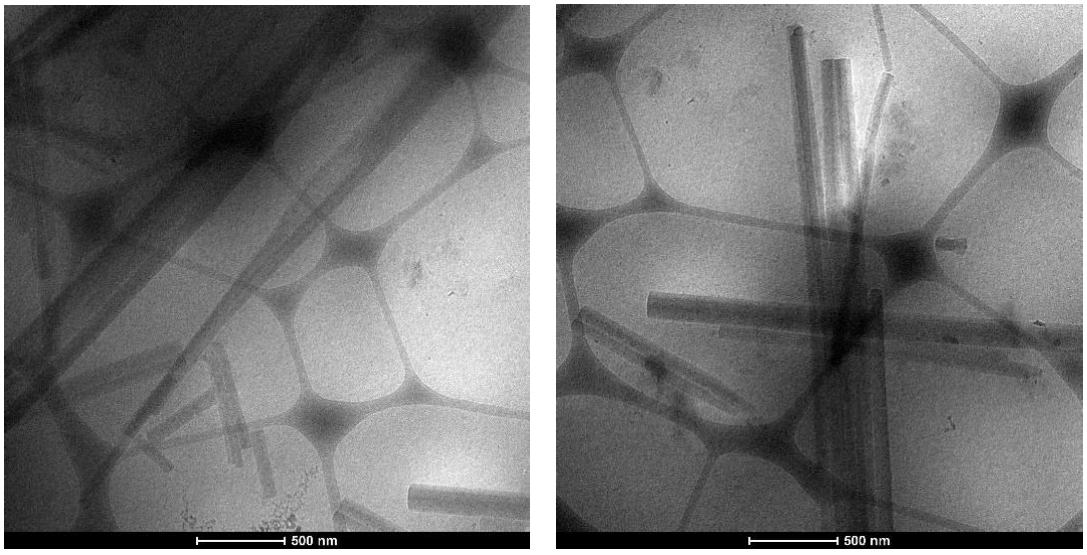

Fig. S66. Cryo-TEM images of Phe-^{D}Nle-Phe.

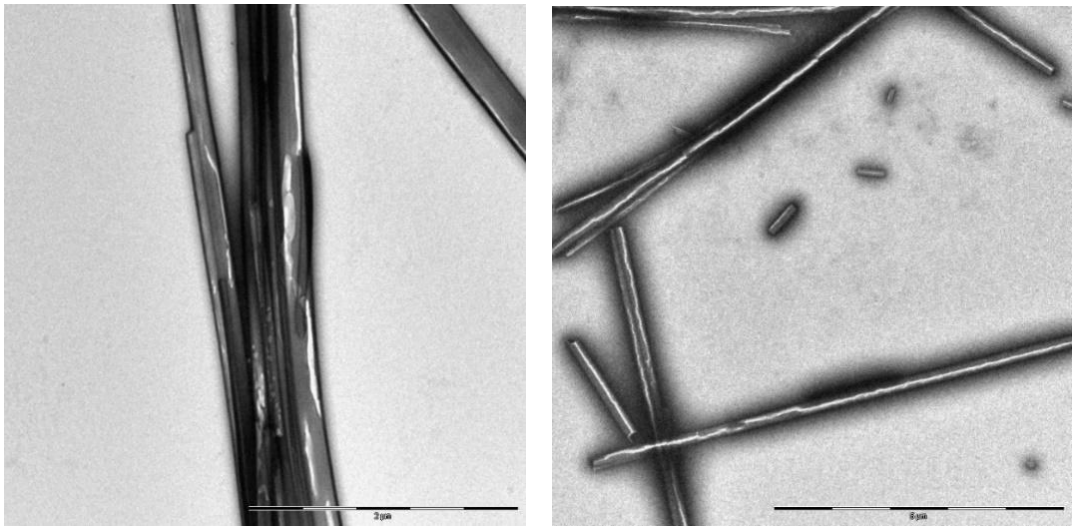

Fig. S67. TEM images of Phe-^{D}Nle-Phe.

16. Frequency sweep rheometry data.

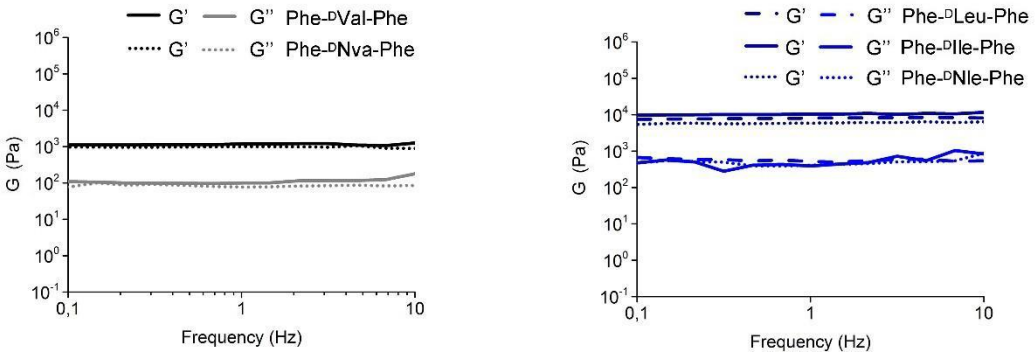

Fig. S68. Frequency sweeps for peptide hydrogels. All of them showed a clear gel behaviour as the elastic (G') and the viscous (G'') moduli do not depend on solicitation frequency and G' >> G''.

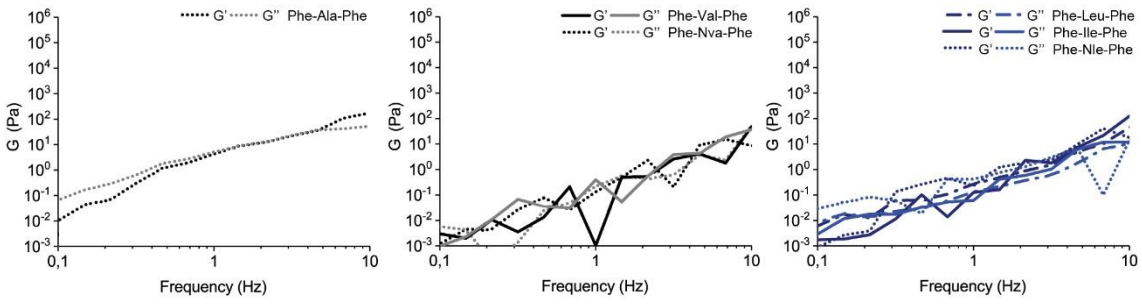

Fig. S69. Frequency sweeps for homochiral peptide systems. None of them showed gel behaviour.

17. Cell viability for peptides in solution.

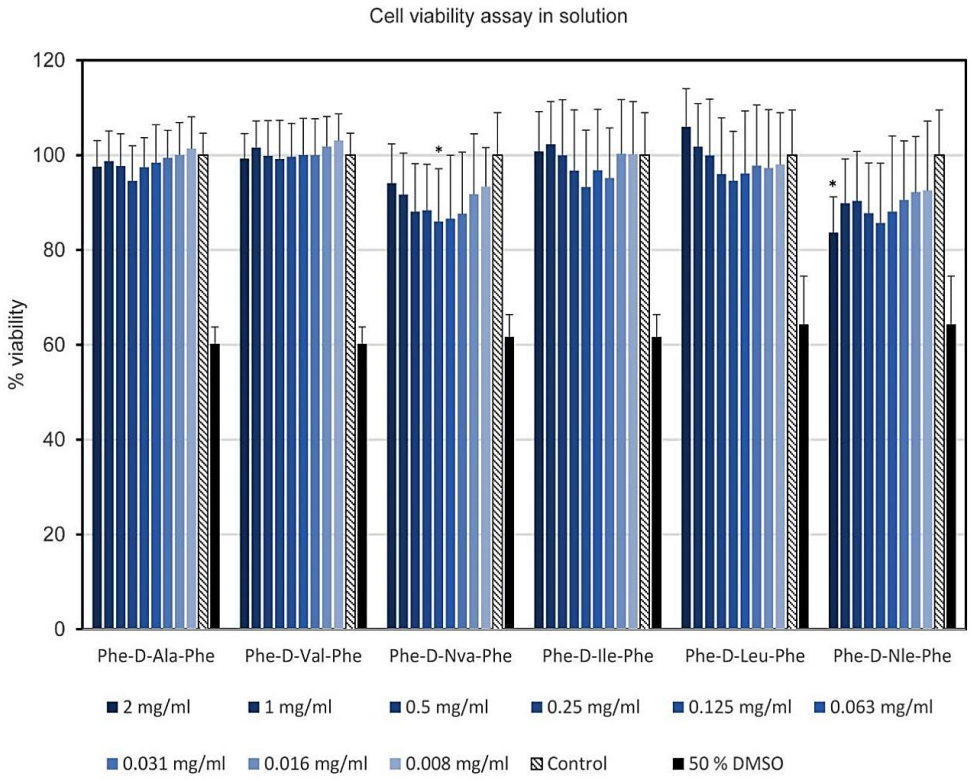

Fig. S70. Cell viability for heterochiral peptides in solution (* denotes statistically significant difference relative to control with $p < 0.05$). Data represent average +- STD of two separate experiments in triplicate ($n = 6$).

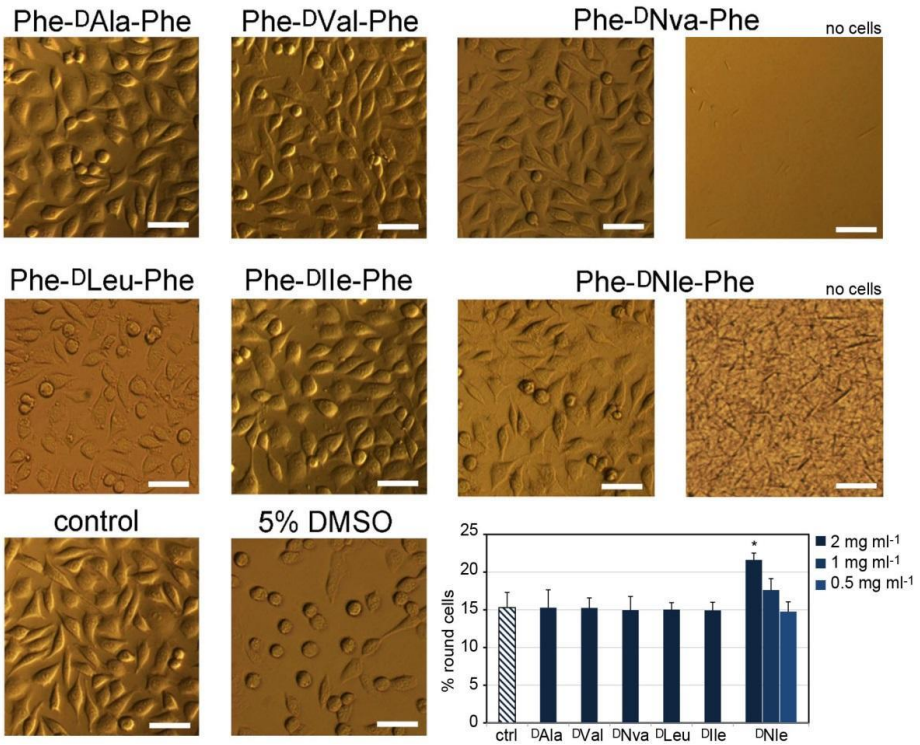

Fig. S71. Bright-field microscopy images of cells treated over 24 hr with peptides in solution at the highest concentration (*i.e.*, 2 mg/ml). In the case of peptides bearing ^{D}Nva or ^{D}Nle, low or high fibrillisation was noted, respectively. The latter case was the only instance where cell spreading was negatively affected, as shown in the graph (* denotes p <0.05. Average and standard deviations of three samples are shown, with each one featuring a cell count of n >500). Scale bar = 50 microns.

18. Protease assay data.

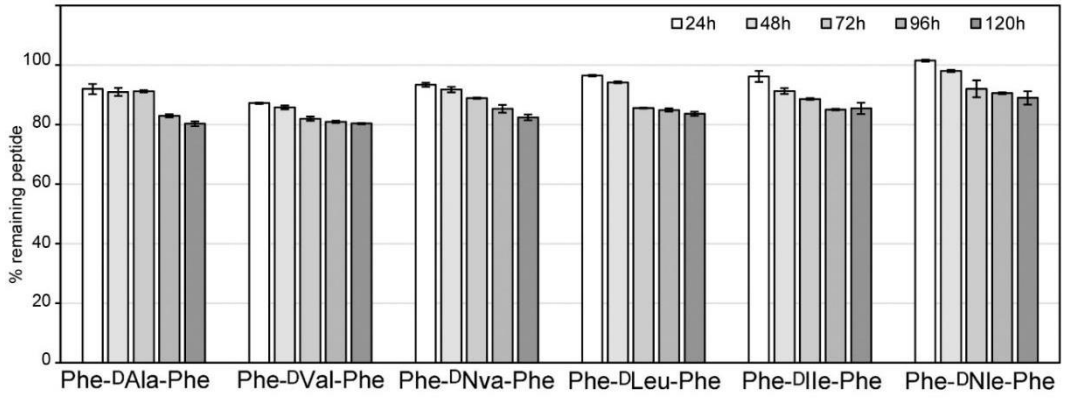

Fig. S72. Peptide integrity in protease assay. >80% of each heterochiral peptide resisted hydrolysis over 5 days. Homochiral L-peptides were not detected after 24 h (complete hydrolysis), with the exception of Phe-Nva-Phe and Phe-Nle-Phe that were found in traces (2.0 ± 0.3 % and 5.0 ±0.2 %, respectively).

Time	hydrogel integrity (%)					
	^{D}Ala	**^{D}Val**	**^{D}Nva**	**^{D}Leu**	**^{D}Ile**	**^{D}Nle**
24h	-	72	72	80	80	88
48h	-	70	70	80	80	88
72h	-	65	65	75	75	85
96h	-	55	55	72	72	80
120h	-	50	50	**70**	**70**	**75**

Table S5. Hydrogel disassembly in protease assay. More hydrophobic peptides bearing leucine isomers showed higher % integrity over time.